nature electronics

SUPPLEMENTARY INFORMATION

https://doi.org/10.1038/s41928-018-0116-y

In the format provided by the authors and unedited.

Three-dimensional integrated stretchable electronics

Zhenlong Huang[1,2,9], Yifei Hao[1,3,9], Yang Li[1,9], Hongjie Hu[4], Chonghe Wang[1], Akihiro Nomoto[1], Taisong Pan[2], Yue Gu[4], Yimu Chen[1], Tianjiao Zhang[4], Weixin Li[1,3], Yusheng Lei[1], NamHeon Kim[1], Chunfeng Wang[1,5], Lin Zhang[1], Jeremy W. Ward[6], Ayden Maralani[7], Xiaoshi Li[1], Michael F. Durstock[6], Albert Pisano[1,4,7], Yuan Lin[2] and Sheng Xu[1,4,7,8]*

[1]Department of Nanoengineering, University of California San Diego, La Jolla, CA, USA. [2]State Key Laboratory of Electronic Thin films and Integrated Devices, University of Electronic Science and Technology of China, Chengdu, China. [3]Biomedical Engineering, School of Precision Instrument and Opto-electronics Engineering, Tianjin University, Tianjin, China. [4]Materials Science and Engineering Program, University of California San Diego, La Jolla, CA, USA. [5]The Key Laboratory of Materials Processing and Mold of Ministry of Education, School of Materials Science and Engineering, School of Physics & Engineering, Zhengzhou University, Zhengzhou, China. [6]Soft Matter Materials Branch, Materials and Manufacturing Directorate, The Air Force Research Laboratory, Wright-Patterson Air Force Base, OH, USA. [7]Department of Electrical and Computer Engineering, University of California San Diego, La Jolla, CA, USA. [8]Department of Bioengineering, University of California San Diego, La Jolla, CA, USA. [9]These authors contributed equally: Zhenlong Huang, Yifei Hao, Yang Li. *e-mail: shengxu@ucsd.edu

This file includes Supplementary Notes 1-9 and Supplementary Figures 1-63

Supplementary Note 1. The mechanical coupling between different layers in the 3D integrated device and potential solutions to mitigate the constraints

The chips/interconnects can add mechanical loading to the local elastomer matrix and result in strain non-uniformity in the vicinity areas. Compared with a single layer, such constraints from a multilayered device will be more prominent and thus influence the overall stretchability of the device, as shown in Fig. 1c and Supplementary Fig. 6. There are two potential solutions to solve this problem.

Solution 1: One approach is to reduce the dimensions of the rigid chips, by using the unpackaged bare dies. As shown in Supplementary Fig. 7, the XCT images of a typical functional chip (e.g., the amplifier) highlight the dimensions of the packaged chip, polished chip, and bare die. It can be seen that the width of the chip decreases from 6.2 mm (packed chip) to 2.3 mm (bare die) and the thickness decrease from 2.3 mm (packed chip) to 0.3 mm (bare die). The strain at the interface between the rigid and soft components decreases dramatically with reducing the rigid component size. Therefore, the constraints from the rigid components can be effectively reduced by moving from bulky packaged chips to small bare dies. In addition, bare dies can also improve the areal density of functional chips.

Solution 2: A strain isolation layer can be added between the adjacent layers. The strain isolation layer is usually an elastomer with ultra-low Young modulus or even liquid[1], which can effectively decouple the rigid and soft components. To study the strain isolation effect, an elastomer/solution layer with different Young modulus was added between two adjacent layers, as illustrated in Supplementary Fig. 8a. To control the thickness of the device, the strain isolation layer was limited to a thickness D = 0.15 mm with D/C = 0.06. And the interconnect length/chip width ratio L/C was controlled to be 1.06. The interconnect geometry and strain distribution were calculated by FEA under 20% stretching, as shown in the insets of Supplementary Fig. 8b-8e. With the Young modulus of the strain isolation layer decreased from 1000 kPa (PDMS) to 0.06 kPa (solution), the interconnect geometry becomes more uniform (Supplementary Fig. 8b-8e) and the maximum principal strain of the interconnect becomes smaller (Supplementary Fig. 8f). The Silbione elastomer with an ultra-low Young modulus of 3 kPa can achieve similar results as the solution based strain isolation layer. From these studies, it can be seen that low Young modulus (less than 3 kPa) elastomer/solution can be used as an ideal strain isolation mechanism to decrease the constraint between layers.

Supplementary Note 2. Adhesion between the Ecoflex in different layers

To assess the adhesion between the Ecoflex in different layers, the debonding energy was measured based on the strain-stress curves of three samples: a single substrate, a bilayer sample, and a debonding sample, as shown by the schematics in Supplementary Fig. 9.

A: Sample fabrication

(1) Single substrate

The process began with a coating of polymethyl methacrylate (PMMA) (5 μm thick) on two pieces of glass slides. Then the PMMA/glass slides were cured on a hotplate at 180 °C for 1 min. Two spacers with 1.00 mm thickness were placed between the two glass slides, and Ecoflex 0030 (1:1) was poured into the cavity between the two glass slides. The cured Ecoflex sample was then peeled from the glass slides and cut into several slices (length: 63.5 mm; width: 10.9 mm).

(2) Bilayer sample

The bilayer sample consisted of the single substrate and a second layer of Ecoflex. The single substrate was prepared first. Then two spacers with 2.00 mm thickness were placed on the top of the single substrate, and one piece of glass slide coated with cured PMMA was laminated on the spacers. Ecoflex-0030 (1:1) was poured and cured in the cavity between the single substrate and the glass slide. Removing the glass slide completed the fabrication process. Finally, the sample was cut into several slices with a length of 69.5 mm and a width of 11.2 mm.

(3) Debonding sample

The debonding sample consisted of two layers of Ecoflex, with a small region left unbonded in between. The fabrication approach was same as the bilayer sample, except that there was an unbonded region on one side of the bilayer interface. The unbonded region had an area of 10.92 mm × 3 mm and was created by inserting a thin plastic film before curing the second layer of Ecoflex. After the second layer of Ecoflex was cured, the plastic film was extracted out of the bilayer interface.

B: Testing method and principle

Before doing the tensile testing, each sample was glued and fixed on acrylic boards. Then, the samples were clamped and stretched by the tensile testing machine (Instron 5965). The testing rate was 1.25% per second, and the load cell was 1 kN. When measuring the debonding sample, a single lens reflex camera (Canon EOS70D) was used to take a video and record the entire process so that the time of delamination between two layers can be captured. The stress-strain curves of those three samples were obtained.

Based on the strain-stress curves of single substrate and bilayer sample, the elastic energy stored in the substrate and bilayer sample could be calculated by equations[2]:

$$U_s(\lambda) = \int_1^{\lambda} P_s(\lambda) d\lambda \ (1)$$

$$U_b(\lambda) = \int_1^{\lambda} P_b(\lambda) d\lambda \ (2)$$

where U_s, U_b, P, and λ are the elastic energy of the single substrate, the elastic energy of the bilayer sample, force, and strain, respectively. When doing the debonding test, the sample was subjected to a constant force P at a steady state. The strain of the detached substrate and bonded bilayer were assumed to be λ' and λ'', respectively, at the point of delamination between the two layers, which could be obtained by multiplying the testing rate and the time of delamination. The elastic energy of the single substrate and bilayer sample were $U_s(\lambda')$ and $U_b(\lambda'')$. Therefore, the debonding energy Γ can be calculated by the equation:

$$\Gamma = U_b(\lambda'') - U_s(\lambda') + P * (\lambda' - \lambda'') \quad (3)$$

For our samples, when the strain reached 400% in the debonding test, there was no deviation of strain-stress curve[3], which meant the delamination did not propagate. The sudden drops in the strain-stress curves in Supplementary Fig. 10 were the failure points when samples were broken due to the limited stretchability rather than the debonding. If the sudden drop at around 400% were to be used as the delamination point, the calculated debonding energy was around 424.26 $J*m^{-2}$. As the delamination point appeared beyond the 400% strain, the real debonding energy between the Ecoflex layers should be larger than 424.26 $J*m^{-2}$. For the wearable electronic device, 400% covers all practical use cases. Therefore, the Ecoflex layers won't delaminate in the multilayered device.

Supplementary Note 3. Bonding strength test between the chip and the interconnect pads

The most vulnerable part of the integrated electronic system is the contacts between solder pads in soft interconnection and rigid electronic chips due to their large mechanical mismatch. In our study, two critical parameters are the flux cleaning and the heating temperature, which are controlled to achieve high-quality bonding. And the details are shown below.

We used tin-based solder paste to bond the chip pins and copper interconnects. Specifically, after transfer printed on the elastomeric substrate, the copper interconnects were cleaned by Flux (WOR331928, Worthington, Inc.) to remove the surface oxides on the copper. Then, the $Sn_{42}Bi_{57.6}Ag_{0.4}$ alloy paste (Chip Quick Inc. SMDLTLFP-ND, with a low melting point of 138 °C) was screen-printed onto the copper pads. Polished chips with reduced thickness and footprint were well aligned on the copper pads, reflowed by baking on a hotplate at ~150 °C for five minutes, and then cooled down to room temperature to form solid alloys between the tin-based solder and interconnect copper pad. The as-formed tin-copper alloy between the chip pins and the solder, and the solder and the interconnects would yield a strong and robust bonding.

In this process, the flux would help remove the copper surface oxide, which would otherwise prevent the formation of solid alloys at the interface and thus lead to large contact resistance and weak bonding. Temperature had to be controlled carefully to melt the $Sn_{42}Bi_{57.6}Ag_{0.4}$ paste. If it was too high, it would melt the solidified alloys in previous layers. If it was too low, the solder paste would not melt thoroughly. Three groups of experiments were carried out to illustrate the effect of these two parameters, as shown in Supplementary Fig. 28.

Group 1: High heating temperature (150 °C) with flux treatment for copper interconnect (Supplementary Fig. 28a).

Group 2: High heating temperature (150 °C) without flux treatment for copper interconnect (Supplementary Fig. 28b).

Group 3: Low heating temperature (140 °C) with flux treatment for copper interconnect (Supplementary Fig. 28c).

For the group 1 (Supplementary Fig. 28a), the solder paste had good wetting behavior and formed a good contact angle between the solder and copper contact pad. For the group 2 (Supplementary Fig. 28b), the contact angle of the solder on untreated copper pads became much larger. The tin solder balls beaded-up, which forced the resistor to move away from the copper pads by surface tension. For the group 3 (Supplementary Fig. 28c), the reflow temperature was a little higher than the solder paste melting point (138 °C). However, the low thermal conductivity of the silicone led to incomplete solder paste melting around the chip, which might most likely cause open circuit and weak bonding.

To characterize the robustness of the bonding between the rigid chips and interconnect, the sample bonded with high heating temperature and flux treatment was used to test its stretchability, as shown in Supplementary Fig. 29. During the tensile test, the resistance of the device was continuously monitored. When the strain was 0%, the total resistance was 4.67 kΩ (Supplementary Fig. 29a). The results shown in Supplementary Fig. 29b indicated that the device had a stretchability of more than 120%. During the entire stretching process, the interface bonding between the rigid chip and interconnect pads was very stable and did not show any evidence of delamination. The serpentine interconnect was broken before the bonding between the rigid chip and interconnect pads failed, when it was stretched to 138% (Supplementary Fig. 29c), clearly proving the robustness of the bonding between the chips and the interconnect pads.

Supplementary Note 4. Comparison of different approaches for VIAs

The VIA formed by laser cutting has much higher complexity, better robustness, and lower resistance compared with other approaches reported in the literature. We discuss three typical VIA formation methods in the following.

The lithography-based method for copper VIAs used oxygen plasma etching (300 mT, 20 sccm O_2, 200 W for 10 min) to form a crater in the polyimide (PI) layer through a mask defined by high-resolution photolithography. Then, a thin layer of copper (600 nm) covering the internal surface of the crater was deposited through electron beam evaporation. For this method, **first**, the "VIA" presented was not the VIA in the conventional sense which should connect *different* layers of circuits for the electrical communication. The "VIA" in that work was used to connect the copper wires in the *same* layer. The insulator between the two connected copper wires was PI, which was only flexible but not stretchable and could not be used as the matrix material for the entire stretchable system. **Second**, the PI layer was very thin (1.2 μm), because oxygen plasma had limited etching capabilities. This approach could not be used to form high-aspect

ratio VIAs that were needed to connect non-adjacent circuit layers. **Third**, the electron beam evaporation deposited copper thin film could barely and weakly bond to the surface of the VIA sidewalls. When bent or twisted, the VIA shape would be changed and the copper film on the sidewalls might crack, which meant the VIA fabricated with this method was not stable.

The printing-based method exploited the mixture of Ni microparticles/PDMS(5:1)/silicone resin (OE6630, Dow Corning) with a mixing weight ratio of 5:2:3 as the VIA. For this kind of metal/polymer composites, **first**, the resistance was very large. As the authors described in the article "the range of initial resistance of core–shell VIAs was around 10-20 Ω", in comparison to the resistance of 0.068 ohms to 0.070 ohms in our case. With such a high resistance, the printed VIAs had little value for electrical communication in real circuits. The high resistance of interconnects will appreciably change electrical parameters and performance of the designed circuit. For amplifier chips (e.g., AD627), the gain was highly based on the external resistance input. For resonators, the resistance was critical for its quality factor. Besides, the high parasitic resistance would largely increase the power dissipation of the entire circuit. **Second**, the composite VIA formed by this method was not stable upon strain, as presented in Figure 4e of the paper, "the resistance versus applied tensile strain profile suggests that the resistance slightly increased in the low strain regime ($\varepsilon_{appl} < 20\%$), started to decrease, and was finally sustained in the high strain regime ($\varepsilon_{appl} < 100\%$)". The VIA resistance in the paper increased up to around 1.7 times of the initial resistance when 20% strain was applied. The unstable electrical properties of the VIAs would certainly undermine the performance and mechanical reliably of the stretchable system.

Our laser ablation and solder paste injection methods formed the VIAs through thick (100 μm) and stretchable silicone. The as-formed VIAs were used to connect circuits in different layers, adjacent and non-adjacent. Besides, the VIA material was $Sn_{42}Bi_{57.6}Ag_{0.4}$ metal alloy, which had very high conductivity. Furthermore, when heated, a layer of Cu-Sn alloy would form between the VIA and the copper interconnects (for both top and bottom copper wires), which built strong bonding between the VIAs and the interconnects in different layers and made the VIAs very stable.

To prove the high performance of the VIAs formed by the laser ablation and solder paste injection method, a VIA was bonded with two interconnects on the top and bottom layers, respectively, as shown in the schematics of Supplementary Fig. 1e. First, the I-V curves of the VIA under 0% and 100% strains were measured (Supplementary Fig. 30a). The straight line meant it was an ohmic contact between the VIA and copper interconnects. The overlapped two lines indicated the resistance didn't change noticeably with the strain from 0% to 100%. To check the VIA performance under high frequency, impedance spectroscopy data of the VIA was collected (Supplementary Fig. 30b). The impedance increased with the frequency, because of the skin effect for r.f. transmission wires[4] and increased inductive reactance value at higher frequencies (inductive reactance $X_L = 2\pi fL$, where f is the frequency and L is the wire inductance). The high frequency electric current flowed mainly at the "skin"--a surface layer of the conductor. The conductive skin depth was proportional to the square root of the frequency[4]. As such, with increasing frequency, the effective cross-sectional area of the conductor decreased and hence impedance increased. For our VIA, the impedance slightly increased when the

frequency was higher than 1 MHz, and dramatically increased when the frequency was above 50 MHz.

Supplementary Note 5. CNT-Silbione composite electrode biocompatibility

Carbon nanotubes (CNTs) have been used in a variety of biological and biomedical studies serving as biosensors, drug and vaccine delivery vehicles, and biomaterials[5]. With decades of research on bio-applications of the CNT, its toxicity and biocompatibility have been well studied on both cellular and tissue/organ levels. Researchers have demonstrated that on the cellular level, the purified CNT without chemical modification possessed no evidence of cytotoxicity[6,7]. On the tissue/organ level, the CNT performed no or very weak eye irritation and skin sensitization[8]. Results from a study based on human skin equivalent model and a Draize skin irritation test also revealed that the CNT did not induce any acute cutaneous irritation[7].

The CNT could be used as nano-fillers in existing polymeric materials to create electrically conductive nanocomposites. Devices incorporating CNT-polymer based electrodes have been reported[9-11]. The biocompatibility of CNT-polymer composite electrodes has also been verified. Jung *et al.* reported a CNT/PDMS composite flexible dry electrodes for ECG sensing[12]. They cultured skin fibroblast cells on the surface of the electrodes for seven days and the cell viability exceeded 95%, indicating that the CNT/PDMS composite did not affect the cell growth. Ten subjects continuously wore the electrodes on their forearms to reveal the skin compatibility. No irritation/side effects were observed over the seven-day continuous wearing.

Finally, reported evidence of the biological risk of CNT-related materials were mainly focused on lung toxicity, including lung inflammation and granuloma formation[13-16]. Significant evidence of pulmonary toxicity of unrefined CNTs was observed[15]. However, in our case, CNTs strongly adhered to the silbione matrix, and the application was for electrophysiological potential sensing on the skin surface, resulting in no risk of inhalation.

Supplementary Note 6. The local heating behavior of the 3D integrated stretchable system

To assess the local heating behavior of the system, a thermographic camera (Therm-App® TH, 384*288 pixels resolution, Sensitivity < 70 mK) was used to capture thermal images of a working device.

First, the system was placed on the bench at room temperature (24 ^{o}C). After the system was powered on, thermal images of the system were recorded continuously, as shown in Supplementary Fig. 44. It could be seen that the temperature of the device increased as long as the device was powered, and then tended to be stable in around 10 mins. The highest temperature, automatically identified by the thermal camera, was located on the gyro chip, which had the biggest power dissipation as shown in Supplementary Fig. 42. The temperature of the gyro chip increased 2.7 ^{o}C in the first 10 mins and was stable at 27.2 ^{o}C. And the lowest temperature, automatically identified by the thermal camera, was located on the corner of the device, where no chip was located. Detailed information for the temperature variation is shown

in Supplementary Fig. 44b. When the system was shut down, the device temperature recovered to the room temperature in ~10 mins.

Second, to evaluate the real working environment, the system was attached to the human skin to assess the temperature distribution of the system in operation, as shown in Supplementary Fig. 45. The highest temperature of the system increased to 33.6 ^{o}C in 5 mins, only 2.3 ^{o}C higher than the resting state (31.3 ^{o}C), which was acceptable for the human skin.

As shown in Supplementary Figs. 44 and 45, the temperature variation is within 2.7 ^{o}C working at room temperature (24 ^{o}C) and within 2.3 ^{o}C working on the human skin. After the device was turned off, the temperature dropped very fast. Thus, the natural passive heat dissipation was sufficient to manage the device temperature and thus no further specific measures were needed in this case.

Supplementary Note 7. Quantitative electrical measurements of the soft system under strain

This includes two parts: quantitative evaluation of the interconnect under strain, and quantitative electrical measurements of the multilayered system under strain.

Part 1: Quantitative evaluation of the interconnect under strain

A typical serpentine interconnect used in the multilayered system was designed and fabricated to quantify the electrical properties under strain. The I-V curve of the copper interconnect (width: 0.15 mm; pad-to-pad length: 5.68 mm; thickness: 0.02 mm) was tested under 0% and 100% strains, as shown in Supplementary Fig. 52. From the slope of the straight line, the resistance of the copper interconnect could be calculated to be 0.34 Ω (0%) and 0.35 Ω (100%). Furthermore, with the strain from 0% to 100% (increment 10%), the interconnect resistance was measured, as shown in Supplementary Fig. 52b. The resistance varied in a narrow band from 0.33 Ω to 0.36 Ω, which indicated stable electrical properties of the interconnects.

To evaluate the serpentine interconnect performance at high frequencies, the interconnect impedance spectroscopy under 0% and 100% strain states was measured from 6 KHz to 100 MHz, as shown in Supplementary Fig. 53. Two conclusions could be drawn from the data. First, the interconnect impedance increased with increasing frequency, especially when the frequency was higher than 10 MHz due to the skin effect and increased inductive reactance at higher frequencies. Second, with interconnect strain increased from 0% to 100%, the impedance increased 7% when the frequency was lower than 1 MHz and up to around 34% when the frequency was larger than 10 MHz, which owned to the larger wire inductance of the deformed interconnects.

Furthermore, as the ceramic antenna chip was connected with the Bluetooth chip through a 5.75 mm long serpentine (width: 0.15 mm; thickness: 0.02 mm), the S_{11} parameter of the antenna connected with the same length serpentine interconnect (fully encapsulation with Ecoflex as in the multilayered soft system) was tested under strains from 0% to 80%, as shown in

Supplementary Fig. 54. It could be seen that the resonance frequency shifted slightly from 2.475 GHz (0% strain) to 2.461 GHz (80% strain) due to the serpentine interconnect deformation[17], and the corresponding S_{11} amplitude decreased from -16.79 dB to -46.59 dB, which meant less reflection loss when the interconnect was deformed from serpentine geometry (0% strain) to buckled geometry (80% strain).

Part 2: Quantitative electrical measurements of the multilayered system under strain

First, as discussed in part 1, the serpentine was very stable at low frequencies and was more sensitive to the strain when the frequency was higher than 10 MHz. For the Bluetooth communication, we connected a 16 MHz oscillator to the Bluetooth chip and a 2.4 GHz antenna was used for the wireless communication, which meant the Bluetooth module might be the most vulnerable part in the design. The received-signal-strength-indicator (RSSI) of the Bluetooth signal from the multilayered system was measured under different strain levels, with the receiver at a distance of several meters. The collected results are shown in Supplementary Fig. 55. It could be seen that the RSSI varied randomly from -75 dBm to -90 dBm with strains from 0% to 44% of the entire system, which means the Bluetooth module worked well with strain values up to 44%, beyond which, the device was broken and no Bluetooth signal could be detected probably due to the interconnect failure.

Second, it is also very valuable to evaluate the accuracy and quality of the signals acquired by the sensors and processed by the chips under strain. As the four-layer stretchable system was fully packaged by the silicone elastomer. It was challenging to probe the signal quality at defined locations inside the packaged system. So, we redesigned the four-layer system with probing sites embedded, as shown in Supplementary Fig. 56. A few probing sites were added to corresponding interconnects and chip pads. These probing sites allowed us to record the signals after relevant steps, e.g., picked up by the sensor and processed by the pre-amplifier and filters.

In our study, we used the electrocardiogram channel as a representative example. We plotted the original ground truth signal from a functional generator, together with the signals after being picked up by the CNT/Silbione composite electrode, and processed by the amplifier and filters. The signals were compared when the full system was freestanding and under various levels of applied strain (Supplementary Fig. 57). Supplementary Fig. 57a shows the original signal, signals collected by the CNT/Silbione electrode, and signals magnified for 508 times and filtered by the chips under different levels of strain from 0% to 35% in the system. The zoom-in view of the original signal and sensor signal is shown in Supplementary Fig. 57b. Due to different magnitudes of the signals, we normalized them for a side-by-side comparison as shown in Supplementary Figs. 57c and d. The results show that the signals after being captured by the sensor and processed by the chips were very close to the original signal. Also, the different levels of strain applied to the system in this study had nearly no influence on the chip data processing and device performance.

Supplementary Note 8. Laser ablation as a viable tool for manufacturing stretchable electronic systems

In this study, we use the laser ablation to fabricate both the VIA and the interconnects.

For VIAs, it needs to ablate the silicone to generate craters with high aspect ratio. Yet, silicone elastomers are notoriously difficult to be etched due to their chemical inertness. With inorganic -Si-O-Si- backbones and hydrocarbon side chains, silicone elastomers cross the boundary between organic and inorganic materials: the inorganic backbone makes them highly resistant to reactive ion etching, and the organic side chains protect them from fluorine chemistry that is commonly used to break the Si-O bonds. So, for traditional etching methods, it can only generate silicone craters with low aspect ratio, which are not suitable for the VIAs in this case.

Laser ablation, a mass removal method by coupling photon energy to materials[18-21], is uniquely suitable to process silicone elastomers. In comparison with lithography-based processes, it offers quick, precise, and scalable direct-write capabilities[22]. Due to the low absorption of silicone elastomers in the visible and IR ranges, we mixed dyes in the translucent elastomer to enhance the absorption and therefore lower the ablation threshold, which made it possible for nanosecond laser for the VIA formation.

For interconnects, compared with traditional photolithography based etching methods, the laser ablation is more time and cost efficient. Additionally, it is chemical-free.

Yet, there are also some limitations of the laser ablation. For example, the heat generated from the laser could oxidize the copper interconnects. To solve this problem, the copper ablation might need to take place in an inert environment, e.g., in nitrogen or argon. Or after the laser processing, the flux solution might need to be applied to remove the surface oxide layer before the subsequent bonding steps.

Supplementary Note 9. The latency of the 3D integrated stretchable system

For the 3D integrated stretchable system, we used the commercial-off-the-shelf sensors, such as Accelerometer (ADXL335BCPZ), whose turn-on time was only 1 ms (Datasheet of ADXL335. *Analog Devices* **P3**, (2009-2010)). And for the wireless data communication, we used the standard Bluetooth protocol. According to the latency analysis of the Bluetooth network[23], it took 100 ms-200 ms to discover a device. Once connected, however, the communication time between two paired devices was less than 1 ms[23]. Therefore, for our multilayered system, the total time delay including the sensing and wireless data transfer was controlled to be less than 2 ms.

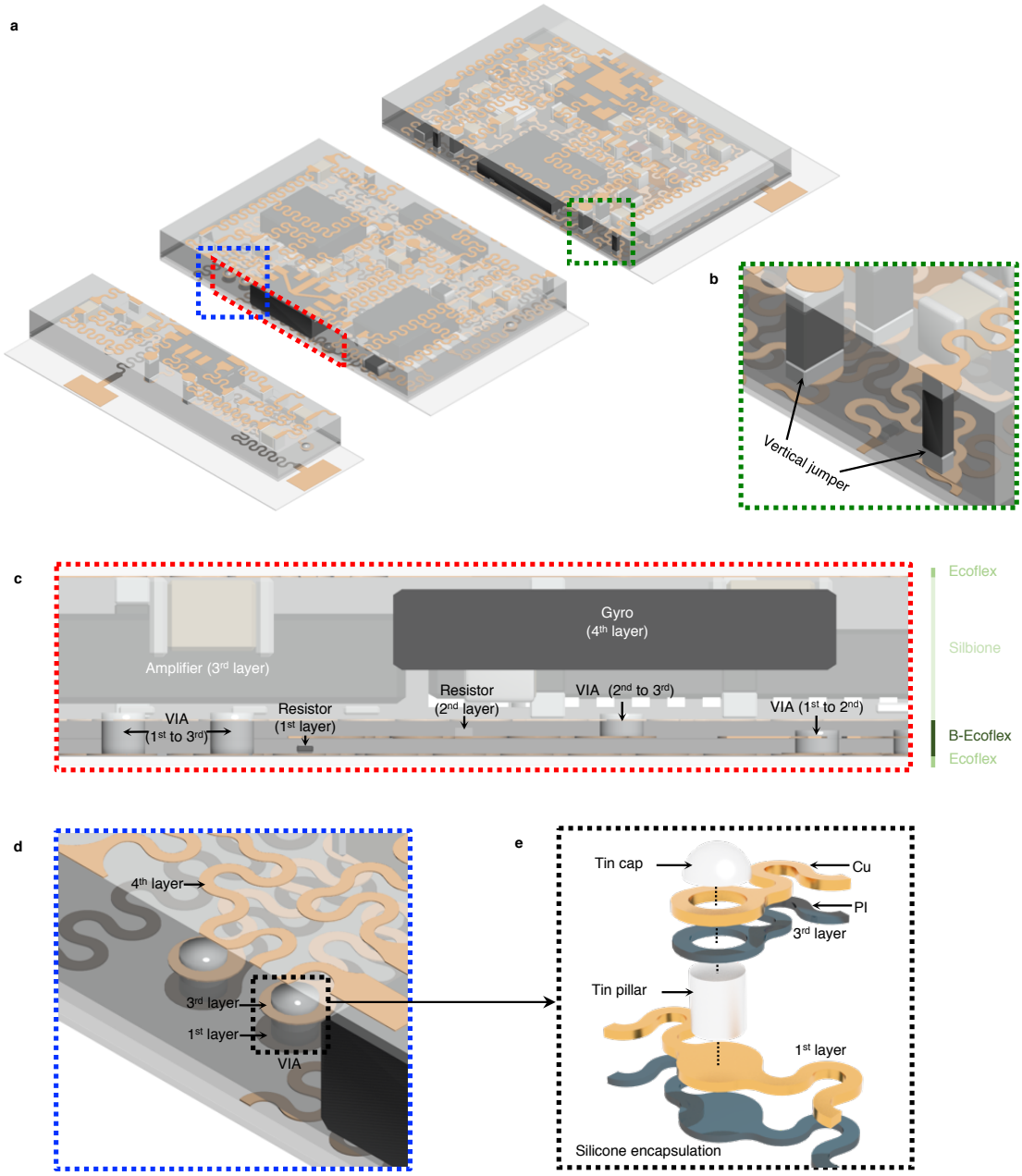

Supplementary Figure 1. Schematic illustration of the three-dimensional integrated stretchable system. a, Overview of a four-layer stretchable device with two cross-section cuts to highlight the design features. **b-d**, Zoomed-in views of the cuts. **b**, Vertical jumpers are used as the electrical connection between the 3rd layer and 4th layer, to accommodate some thick chips. The first three layers use tin based VIAs as the interlayer connection. **c**, The four-layer device has functional sensors and passive components in each layer with VIAs among these layers for interlayer electrical connections. The stretchable system is packed in core-shell structures, with Ecoflex as the shell and ultra-low Young's modulus Silbione as the core, to increase the stretchability of the overall system. B-Ecoflex indicated Ecoflex mixed with the black dye for laser ablation. **d-e**, The cross-section view and the exploded structure of a typical tin based VIA. The serpentine interconnect is composed of bilayers of Cu/PI. With screen-printing, the tin pillar and tin cap are fabricated to achieve solid electrical bonding.

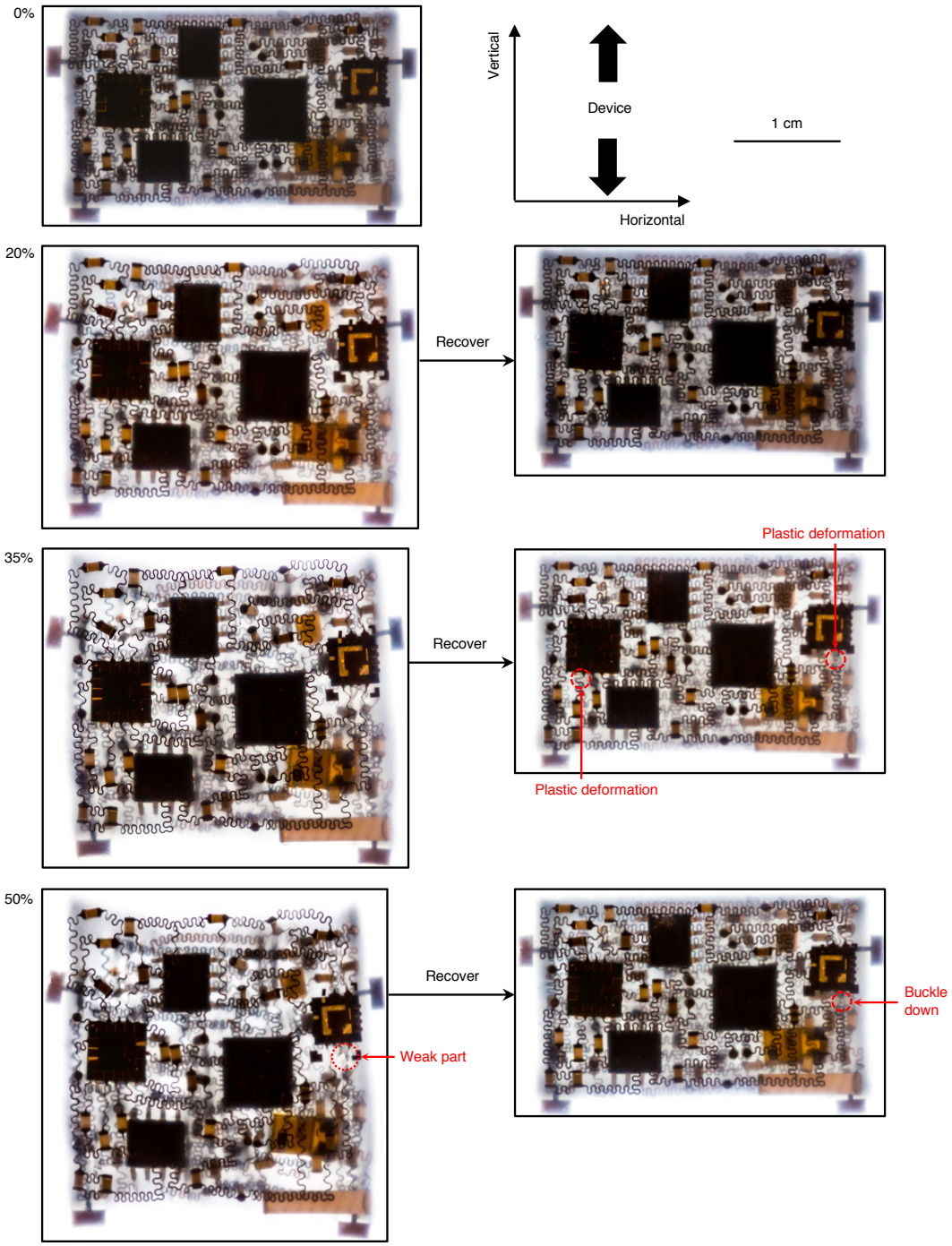

Supplementary Figure 2. Experimental studies of buckling deformations across the entire circuits under uniaxial stretching along the vertical direction. Failure strain in the vertical direction is ~50% with weak points at the interconnect between the accelerometer and capacitor. Plastic deformation begins at ~35% strain.

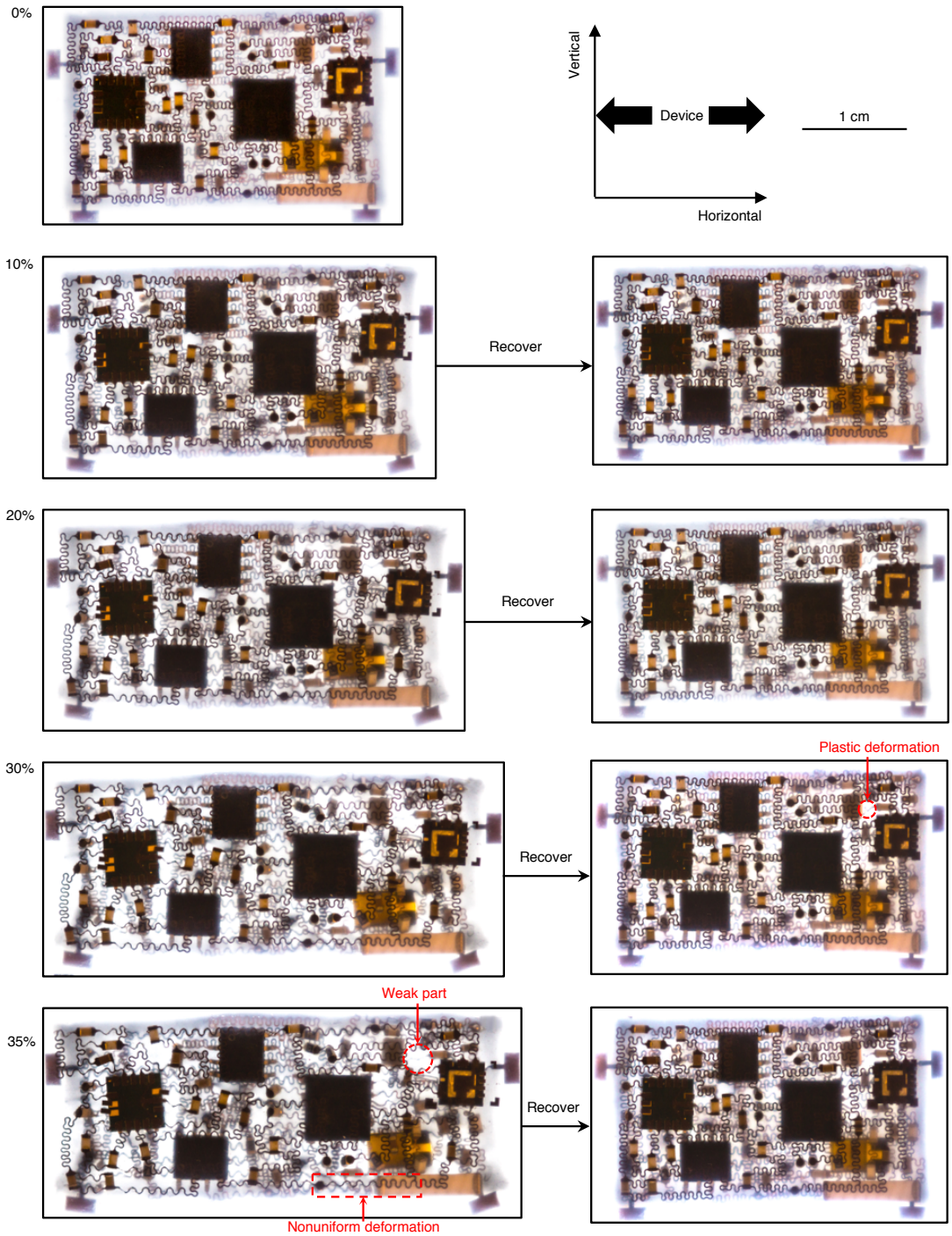

Supplementary Figure 3. Experimental studies of buckling deformations across the entire circuits under uniaxial stretching along the horizontal direction. Failure strain in the horizontal direction is ~35% with weak points at the interconnect between the crystal oscillator and capacitor. Plastic deformation begins at ~30% strain.

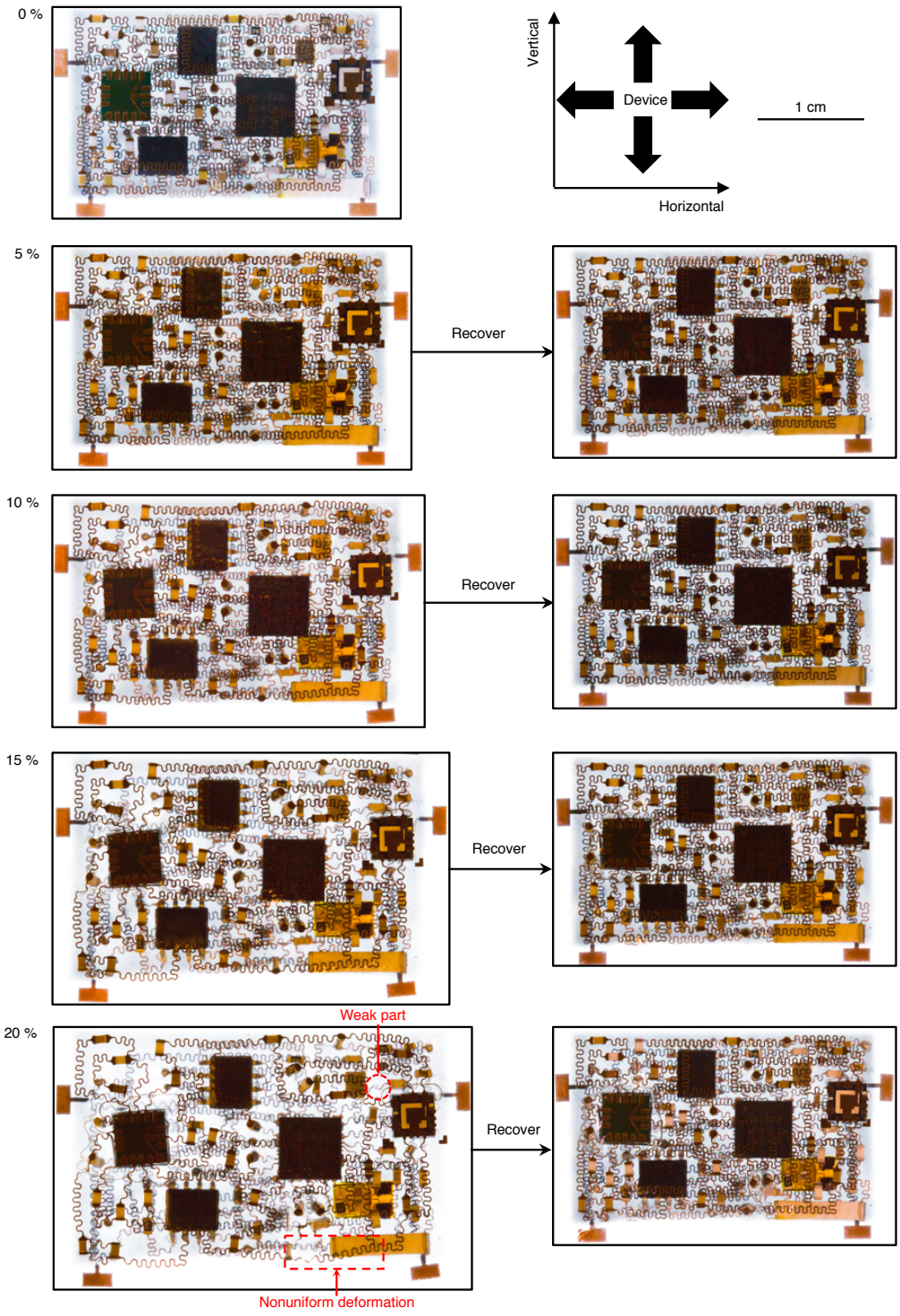

Supplementary Figure 4. Experimental studies of buckling deformations across the entire circuits under biaxial stretching. Failure strain for biaxial stretching is ~20% with weak points at the interconnect between the crystal oscillator and capacitor.

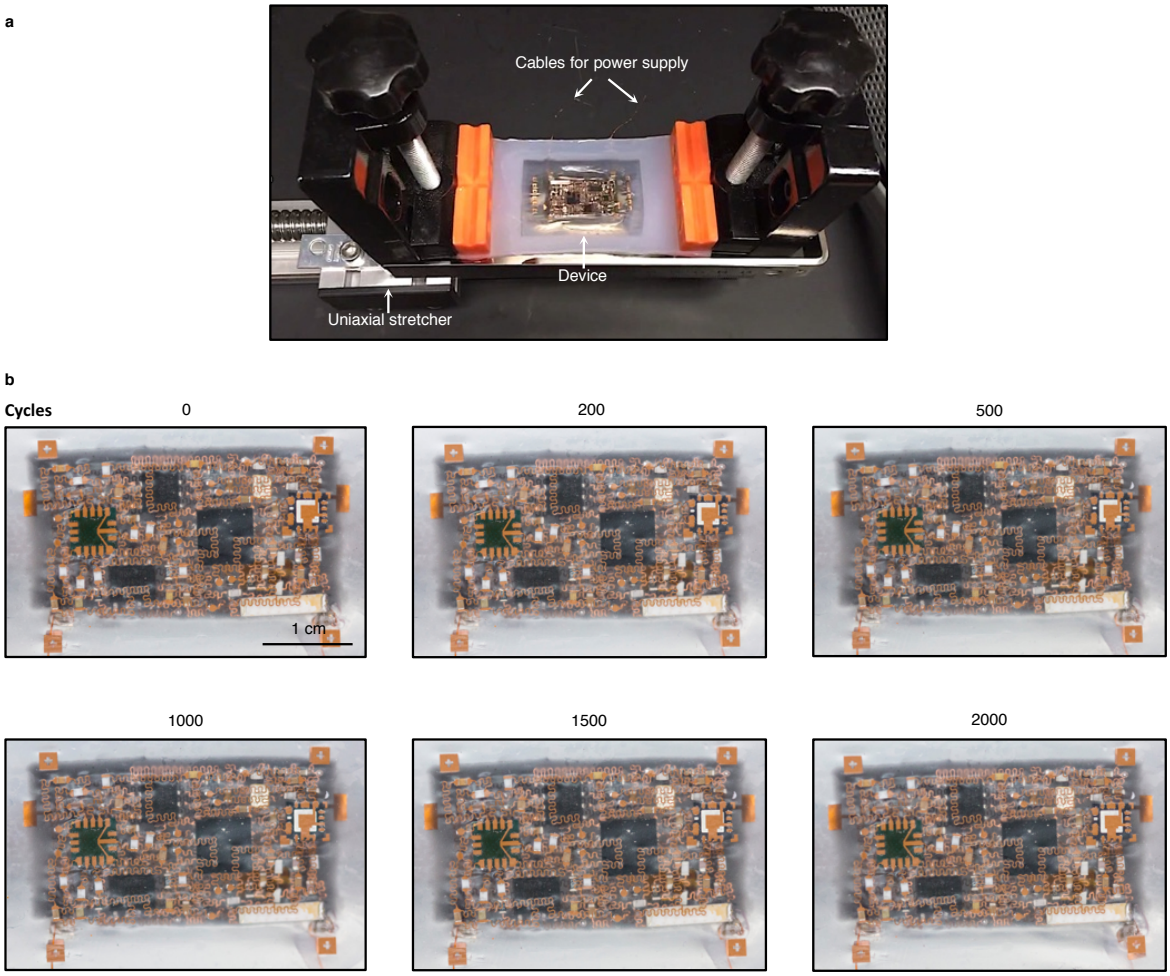

Supplementary Figure 5. Fatigue test of the three-dimensional integrated stretchable device with 10% uniaxial strain at a frequency of 0.5 Hz. a, Setup for the cycling test. A customized electrically controlled stretcher is used to apply 10% uniaxial strain at a frequency of 0.5 Hz to the device. Two cables with minimal mechanical footprint provide connection to an external power supply to the device. Bluetooth signals transmitted from the device are used as an indicator to identify whether the device is damaged during cycling test. **b**, Images of the device after different numbers of cycles. The device remains functional after being cycled for more than 2000 times. The failure mechanism can possibly be the debonding of the components from the Cu pads or the breakage of the interconnects in some strain concentrated areas, which is still under active investigation.

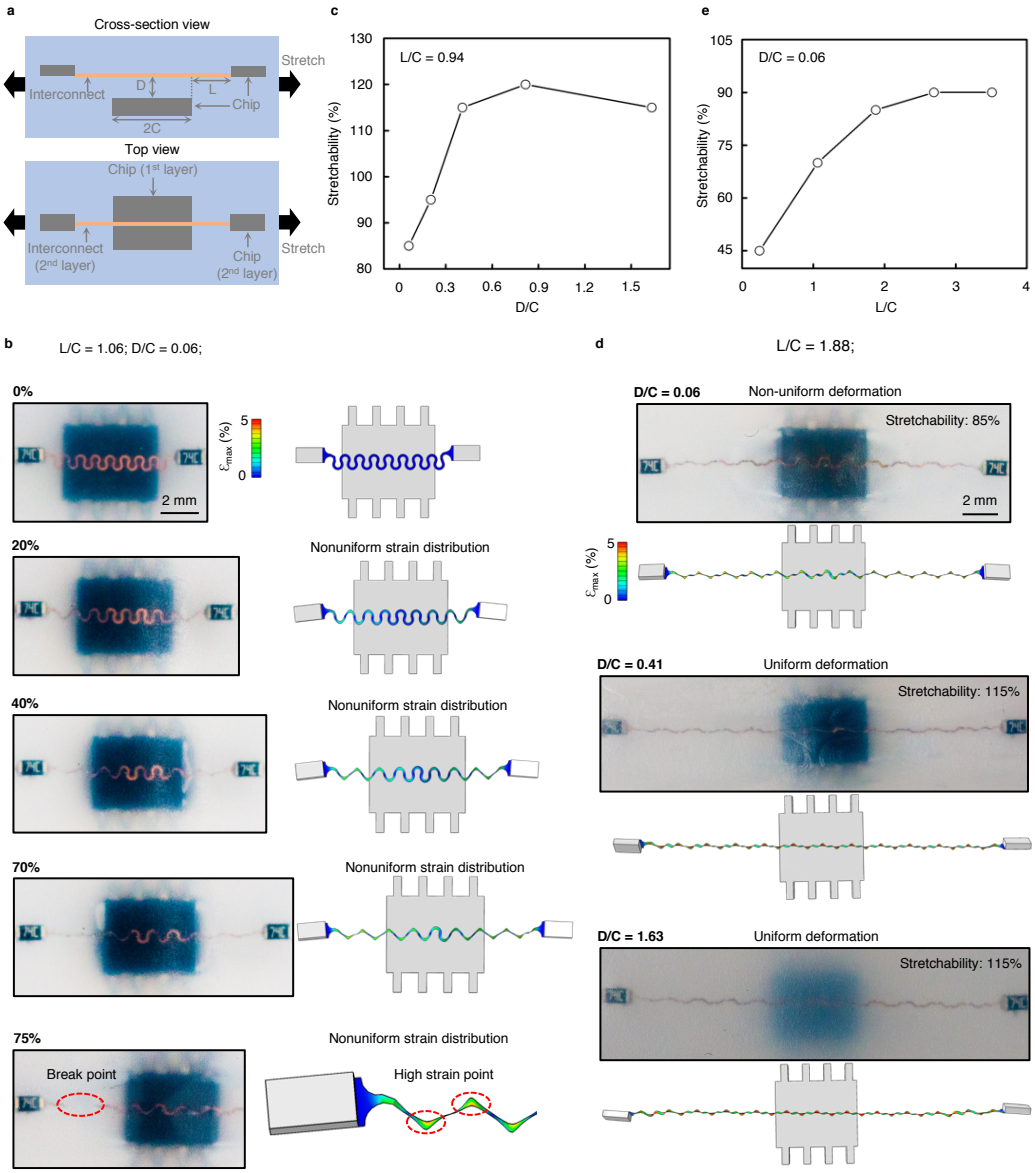

Supplementary Figure 6. Experimental and finite element analysis (FEA) studies of the mechanical coupling between layers of the multilayered device. a, Schematic cross-section and top view of a representative part of interest in the multilayered device. **b**, Experimental and FEA results with a uniaxial strain from 0% to 75%. Due to the constraint from the rigid chips, the strain distribution is nonuniform, as shown from the FEA strain distribution (ε_{max}) in the interconnect. With 75% strain, the serpentine interconnect was broken at the points of highly localized principal strain. **c**, The overall stretchability as a function of the normalized serpentine-chip separation distance D/C. Stretchability is enhanced by increasing the separation distance when D/C<0.4 for the decreased mechanical coupling, and then tend to saturate when D/C>0.4. **d**, Experimental and FEA results to show the decreased mechanical coupling between the layers by increasing the D/C. The interconnect strain distribution is nonuniform for low D/C (e.g., 0.06) and tend to be uniform for high D/C (> 0.4). **e**, The overall stretchability as a function of normalized non-constrained interconnect length L/C. Stretchability is enhanced by increasing the non-constrained interconnect length when L/C<2.7, and then plateaus when L/C>2.7.

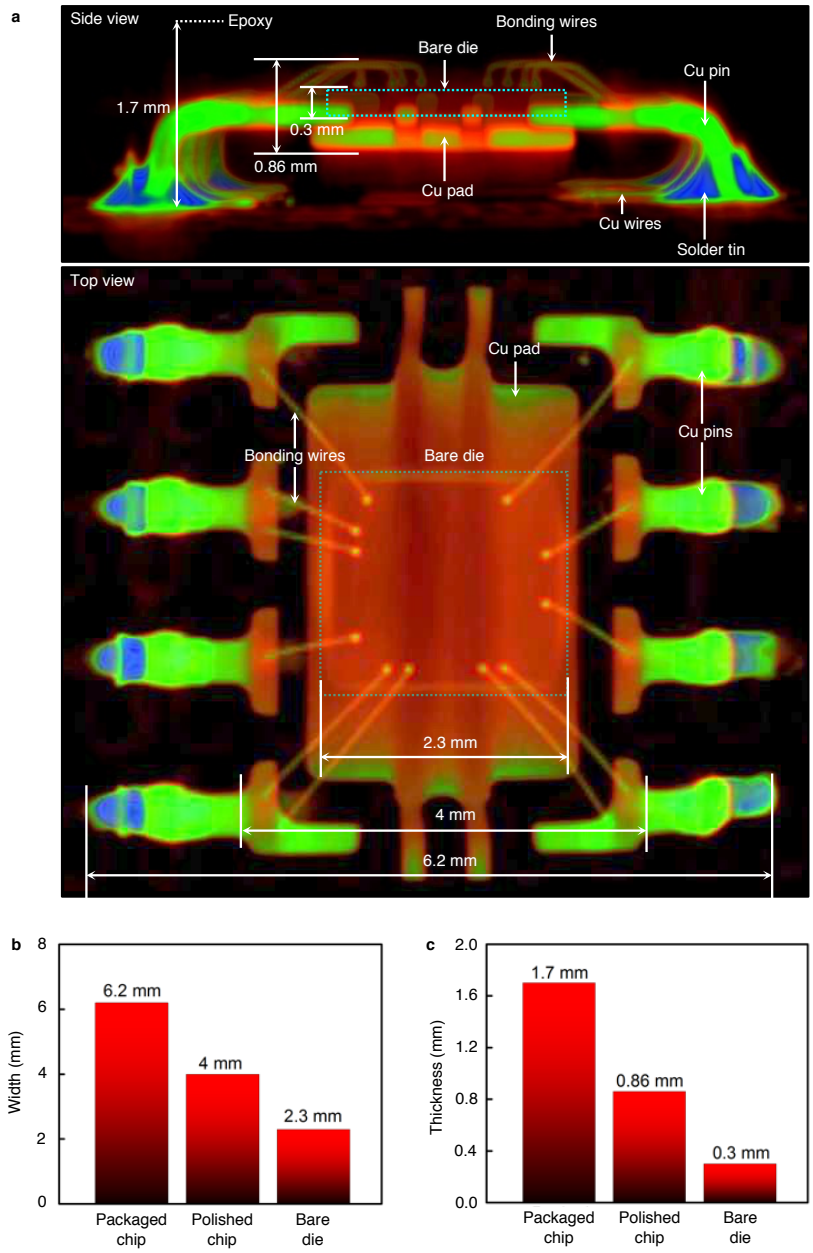

Supplementary Figure 7. XCT images of a typical functional chip (i.e., the amplifier) and summarized dimensions of the packaged chip, polished chip, and bare die. a, XCT images showing the amplifier structure in side and top views. It mainly contains the functional silicon bare die, Cu pins, bonding wires between the bare die and pins, and epoxy packaging (transparent in the XCT images). **b-c**, Summarized width and thickness of the chip with packaging, after polishing, or only bare die. This information can provide design guidelines for using different types of components to build stretchable electronics for different purposes, such as to decrease the device size or mitigate the constraints between layers.

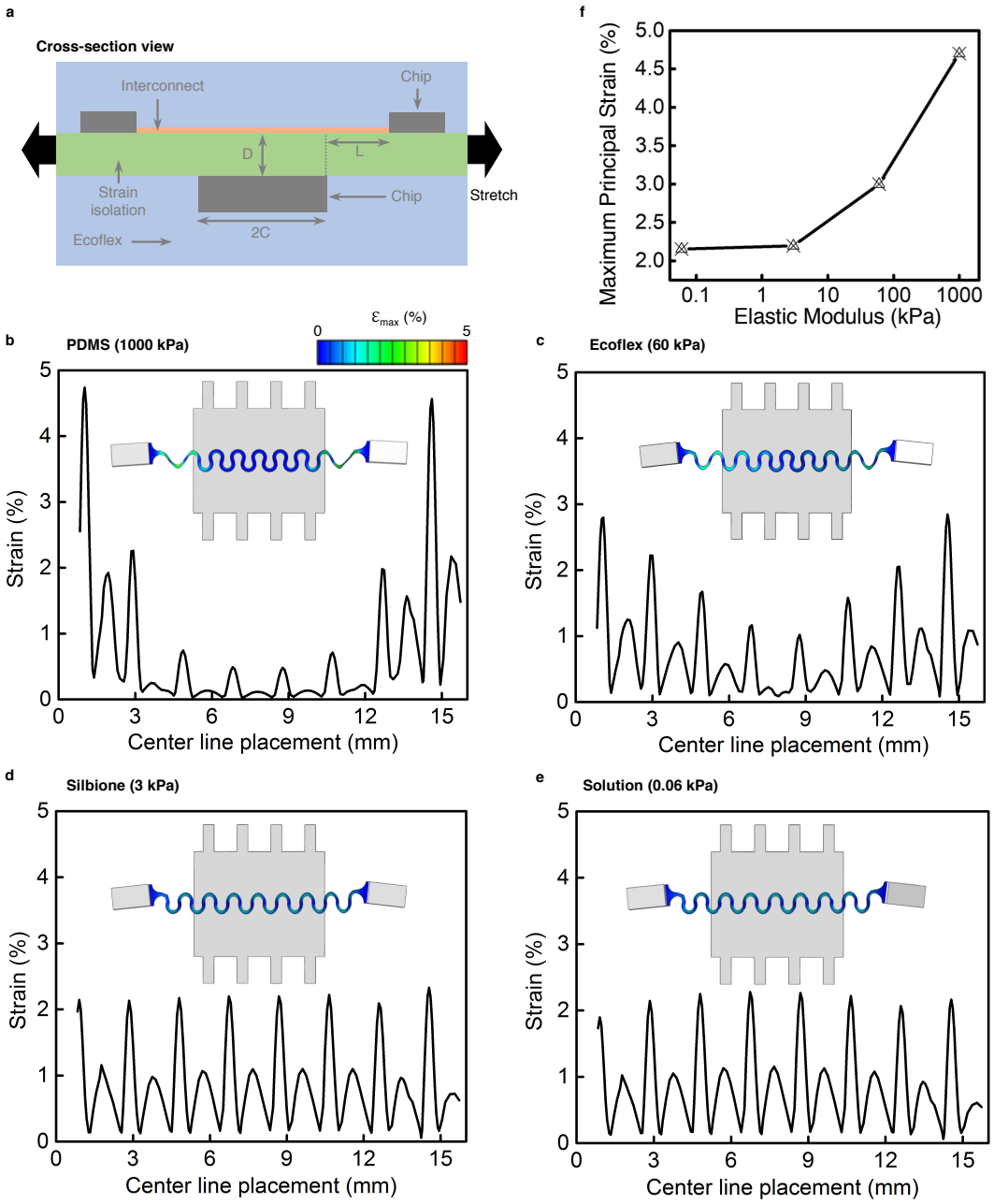

Supplementary Figure 8. Effect of strain isolation layer modulus on the overall stretchability. a, Cross-section view of the multi-layer device integrated with a strain isolation layer between adjacent layers. Key dimensions are labeled. To control the thickness of the device, the strain isolation layer was limited to thickness D = 0.15 mm with D/C = 0.06. And the interconnect length/chip width ratio L/C was controlled to be 1.06. **b-e**, FEA simulation results showing the interconnect center line strain distribution and the entire interconnects strain distribution (inset figure) when the device is under 20% stretching, with different strain isolation layer materials varied from PDMS to Ecoflex, Silbione, and liquid. **f**, The maximum principal strain of the interconnects with different isolation materials.

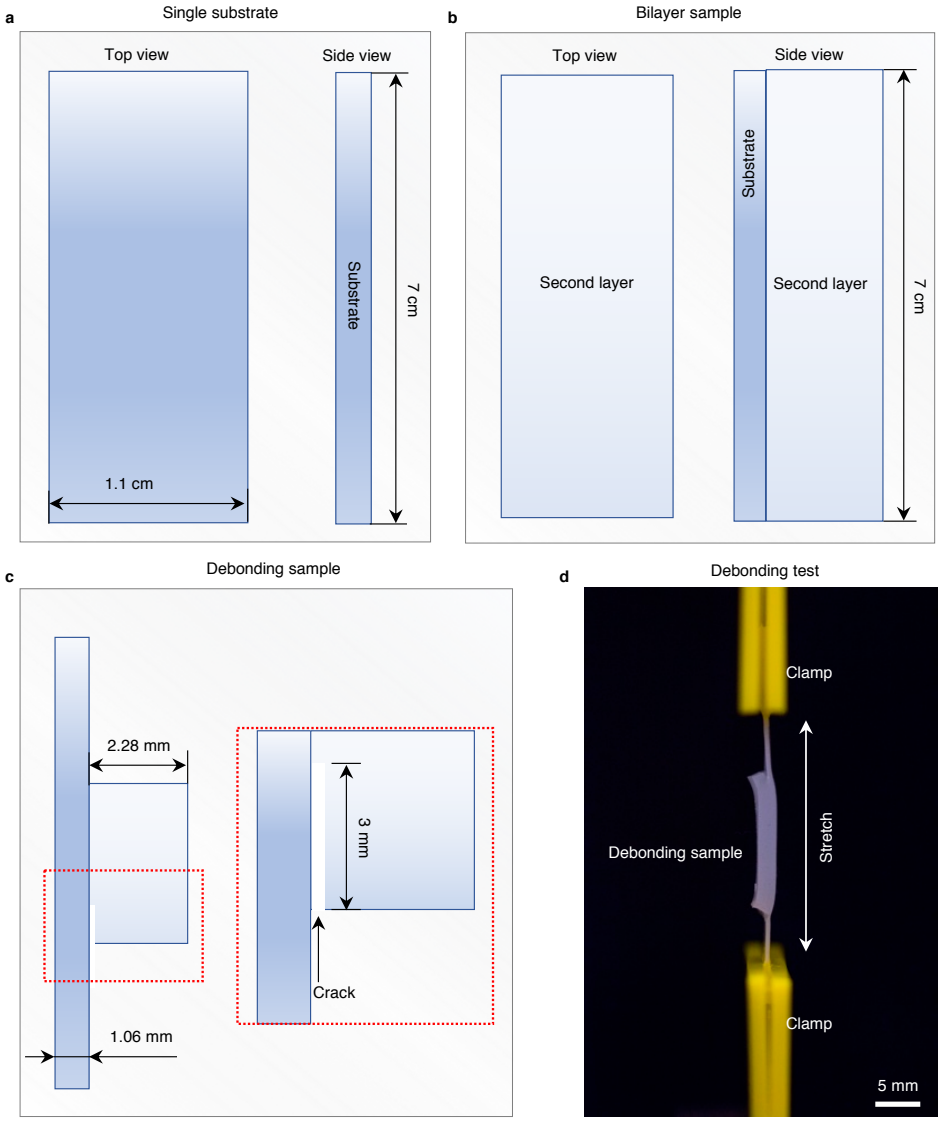

Supplementary Figure 9. Debonding test to show the adhesion between the Ecoflex layers in the 3D integrated stretchable system. a, Schematics of the top and side views of the single layer substrate. **b**, Schematics of the top and side views of the bilayer Ecoflex. **c**, Schematics of the side view of the debonding sample, with a pre-embedded crack (3 mm in depth). **d**, An image of the debonding experiment setup.

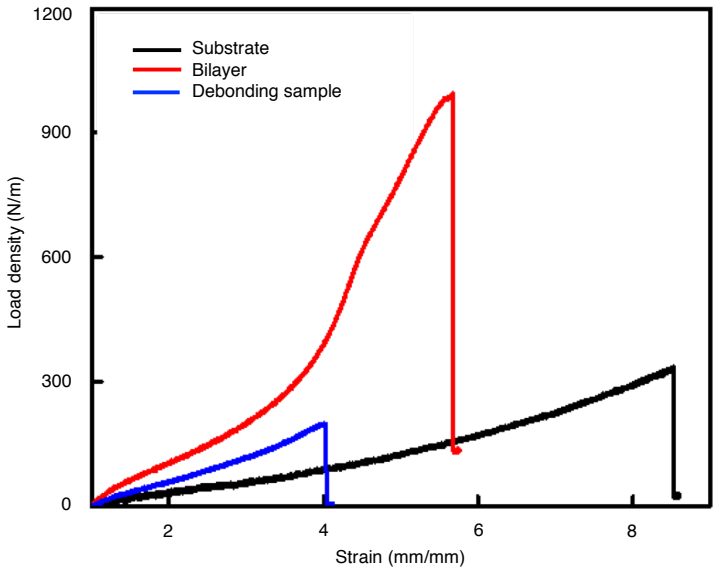

Supplementary Figure 10. Strain-Load density curve of the single Ecoflex substrate (black), bilayer sample (red), and debonding sample (blue) for debonding energy test between Ecoflex in different layers. For our samples, when the strain reached 400% in the debonding test, there was no deviation of the curve, which meant the delamination did not propagate. The sudden drops in the figure are the failure points when samples were broken due to the limited stretchability rather than the debonding.

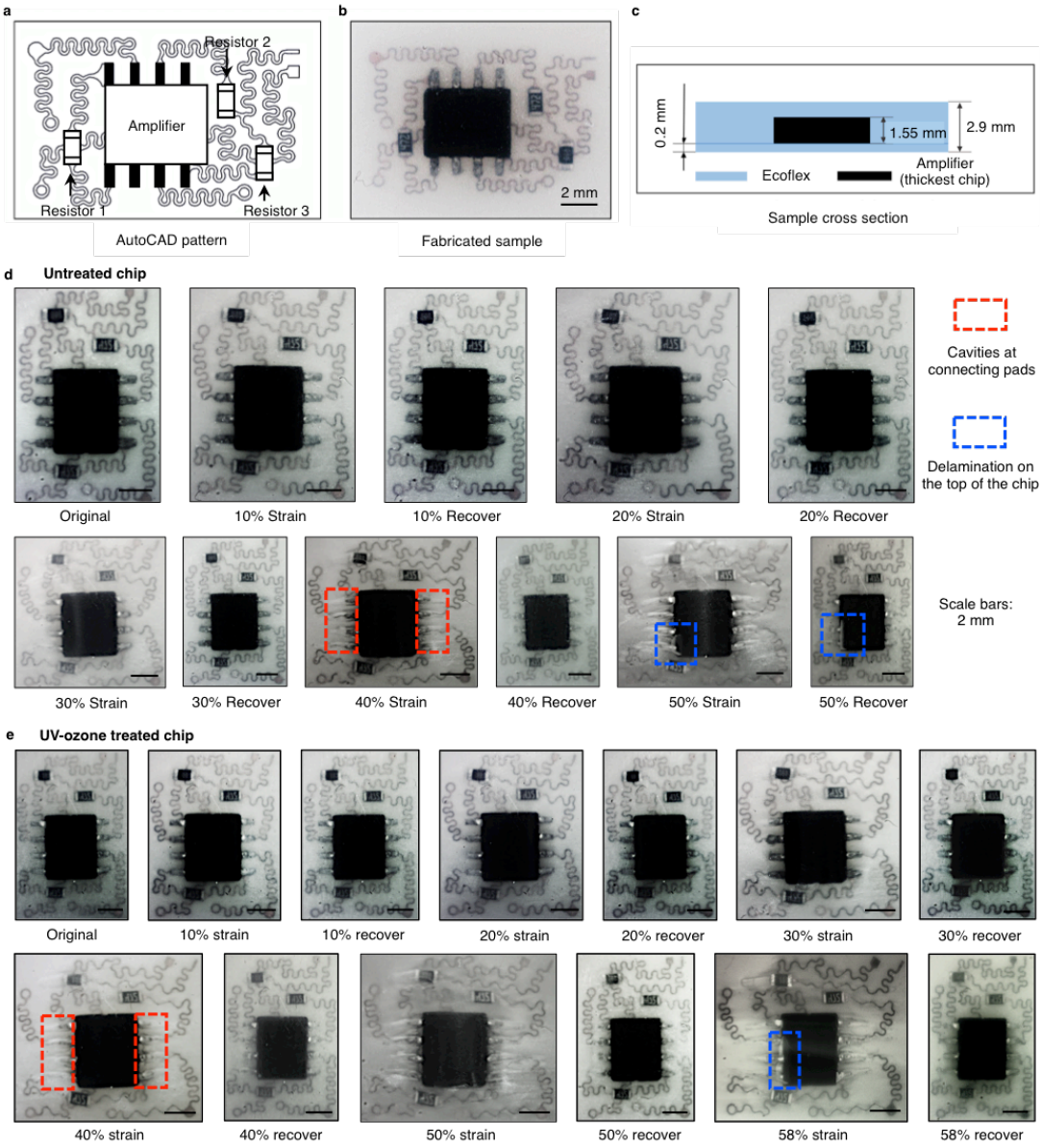

Supplementary Figure 11. Debonding test between the Ecoflex and chips. a, Layout design for a sub-unit of the circuit, which includes a main amplifier chip and several passive chips. **b**, The photograph of the corresponding fabricated sample. **c**, Sample cross section to illustrate the encapsulation scheme of the sample. **d**, Images to show the adhesion between the Ecoflex and untreated chips at different levels of strain. The delamination appears first on connecting pins at around 40% strain. Delamination from the epoxy material on the chip top surface starts at a strain of 50%. Additionally, the delamination on connecting pins can recover because of the smooth surfaces of both the pin and the as-mounded Ecoflex, but delamination on the epoxy still exist after releasing the strain because of the rough surfaces of the epoxy and as-mounded Ecoflex. **e**, Images to show the adhesion between the Ecoflex and UV-ozone treated chips at different levels of strain. With UV ozone treatment, there is no delamination on the epoxy until 58% strain, which is larger than the untreated chips, indicating the enhanced bonding with UV ozone processing.

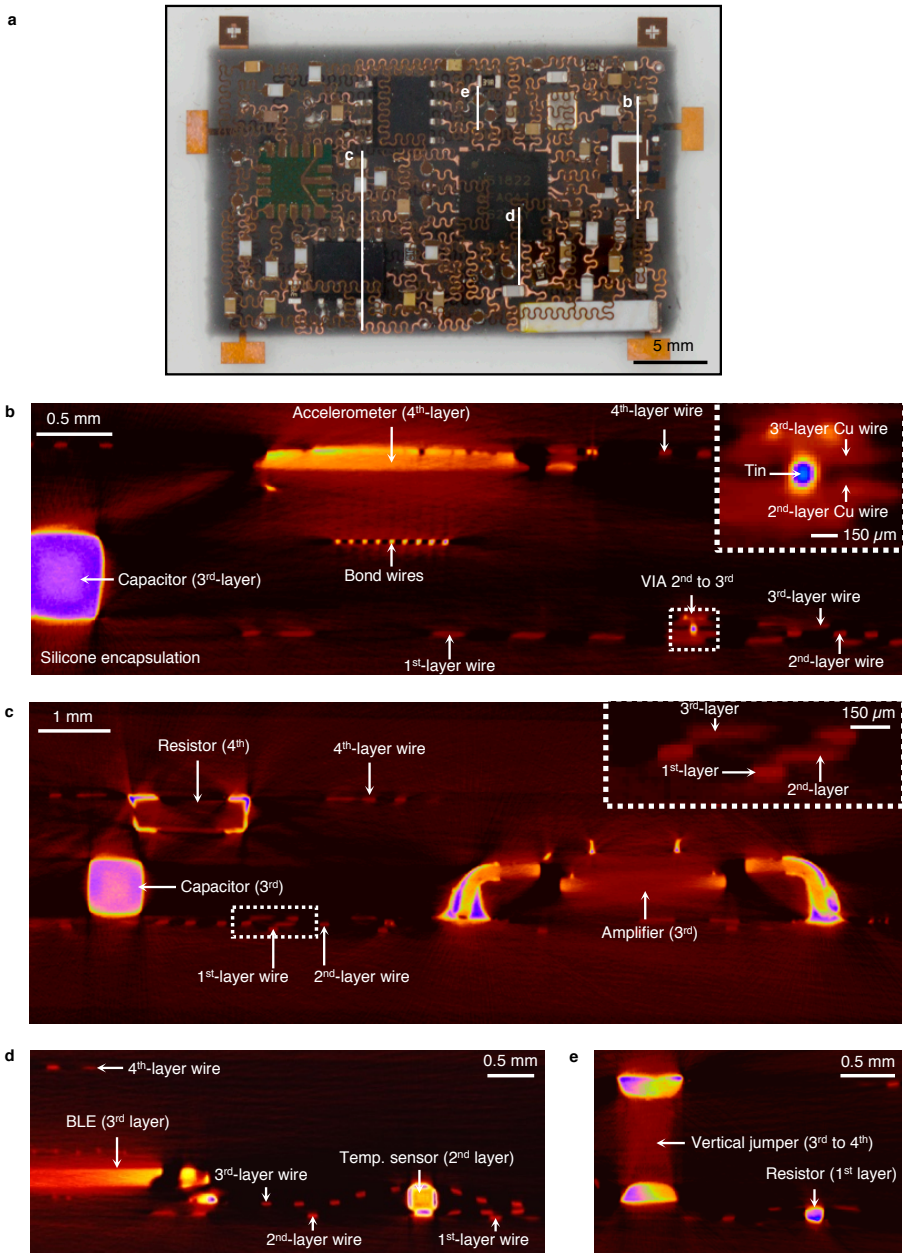

Supplementary Figure 12. X-ray computed tomography (XCT) images showing the cross-sectional structure of the three-dimensional integrated stretchable device. a, An optical image of the integrated device, with markers showing the cross-sectional positions corresponding to (**b**), (**c**), (**d**), and (**e**). The key components and structures are labeled.

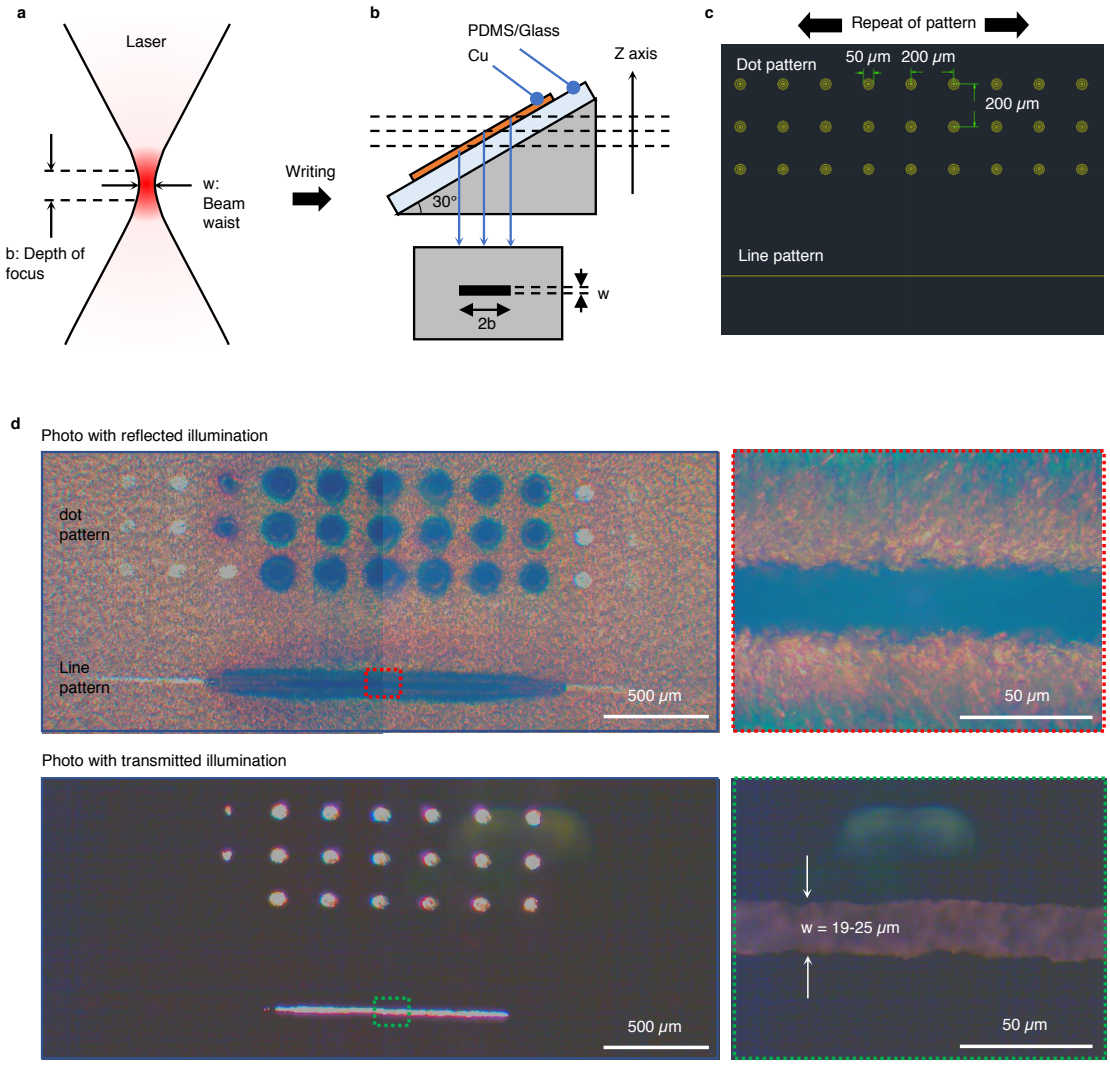

Supplementary Figure 13. Evaluation of the effective laser beam size and depth of focus. a, Schematic illustration of the laser beam. There are two key parameters: beam waist (w) and depth of focus (b). **b**, A Cu foil on a 30° tilted surface to be processed using the laser with the pattern design shown in (**c**). According to the ablation results, shown in (**d**), and tilted angle degree, the laser beam waist and depth of focus can be calculated to be ~25 μm and ~600 μm, respectively.

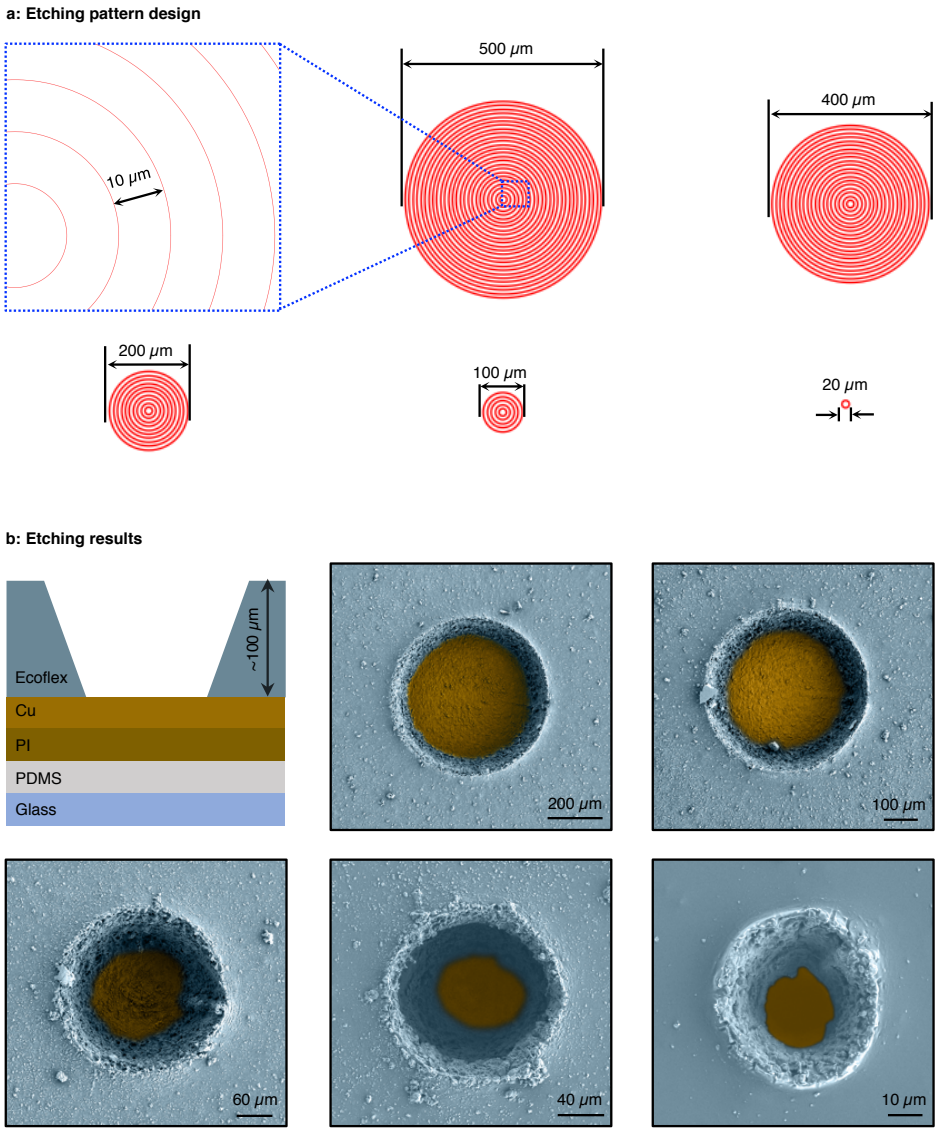

Supplementary Figure 14. Evaluation of the laser fabricated VIA resolution in silicone. a, Pattern design of laser ablation with diameters from 500 μm to 20 μm. **b**, Selective ablation of silicone on the top of the Cu with the corresponding laser pattern shown in (**a**). The smallest diameter of VIA that can be fabricated on 100 μm thick silicone is ~45 μm, as shown in the lower right image in (**b**).

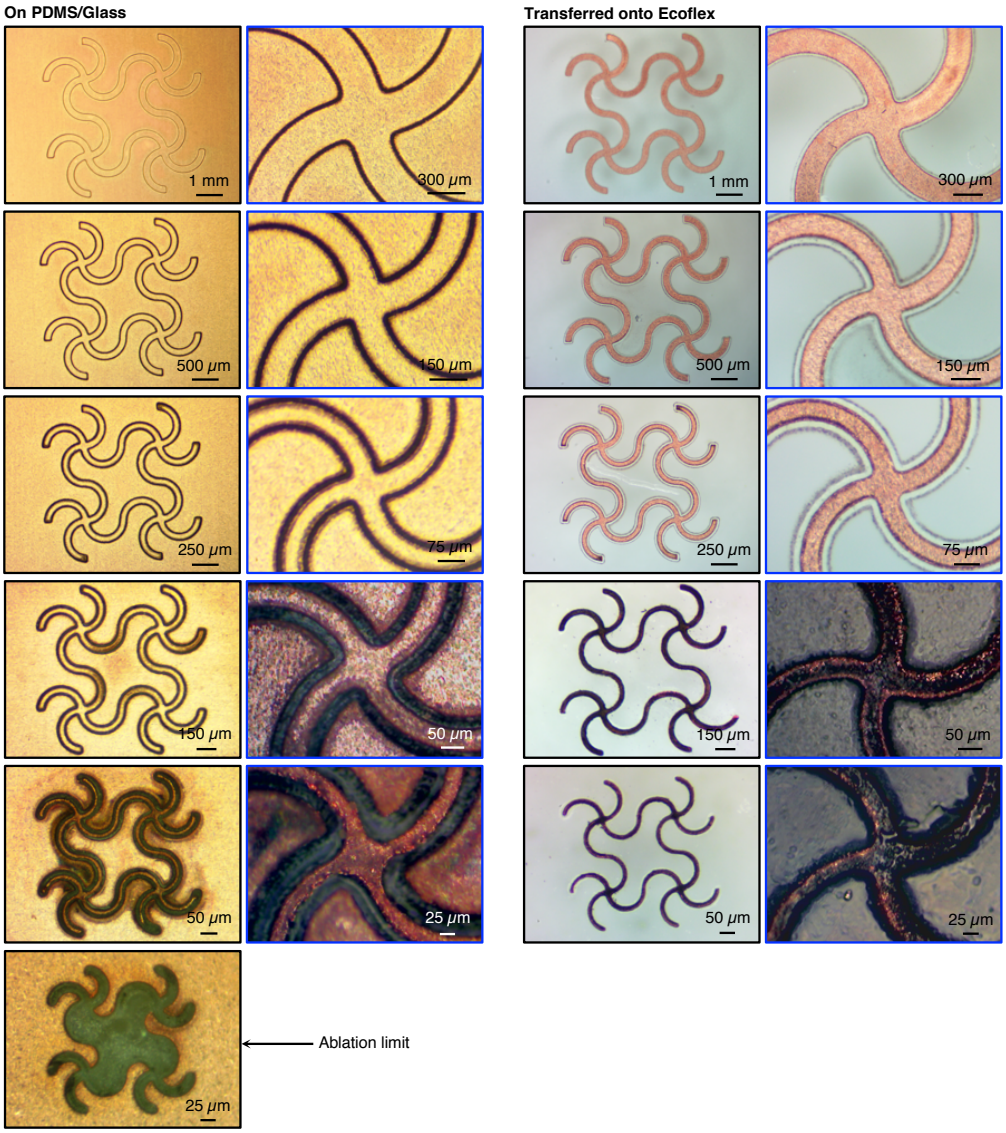

Supplementary Figure 15. Evaluation of pattern resolution of laser ablation in Cu/PI films. Parameters of wavelength 1064 nm, pulse energy 0.42 mJ, and 10 cycles are used to write the serpentine pattern in the Cu/PI on the PDMS/glass substrate. Then the patterned Cu/PI electrodes are transferred onto the Ecoflex substrate with a water-soluble tape. The patterned electrodes, before transfer (left two columns) and after transfer (right two columns), with the width ranging from 300 μm (first row) to 10 μm (second to the last row), are shown. For electrodes with the width less than 10 μm, as shown in the last row, the PDMS substrate is not sticky enough to hold very thin electrodes that would be delaminated by the pressure waves from the laser ablation. The black color on the electrode is due to the thermal oxide on the Cu surface.

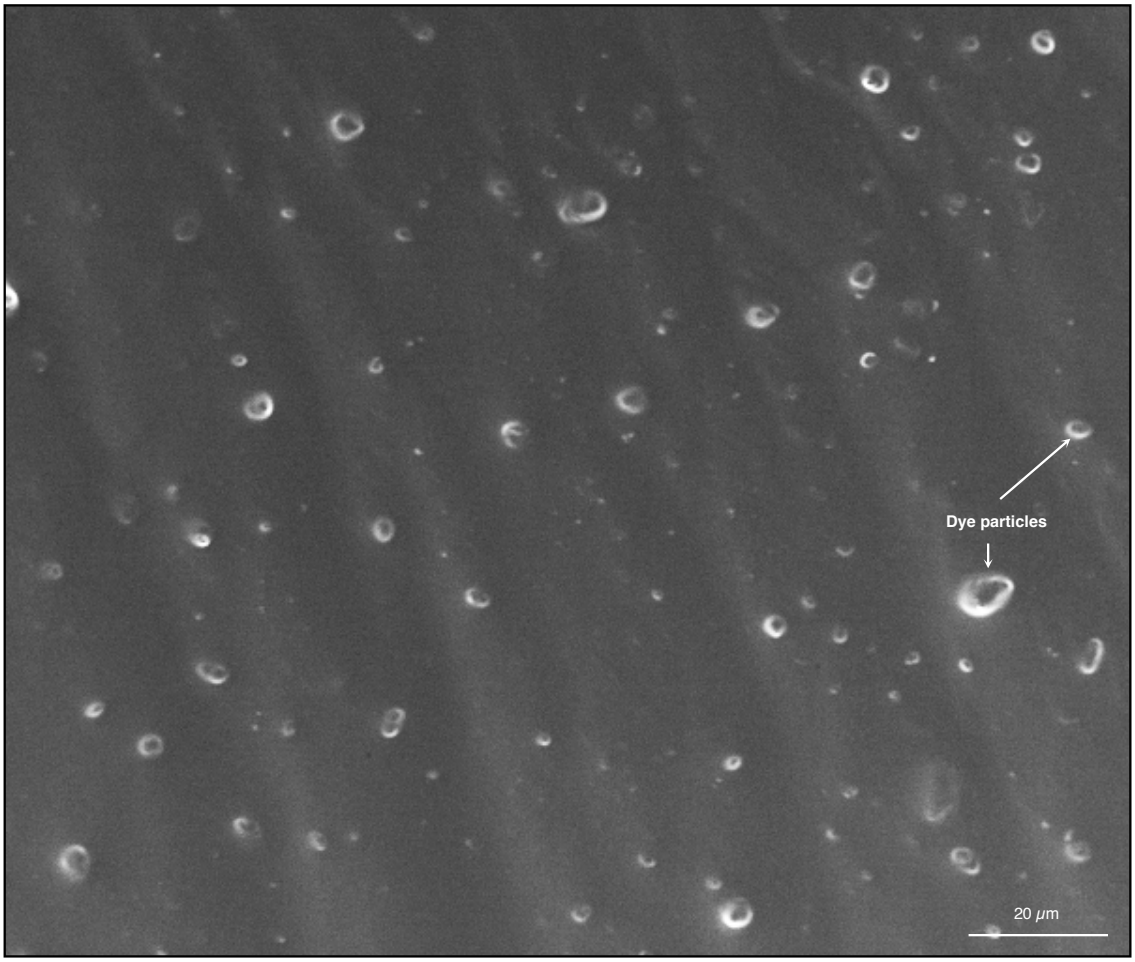

Supplementary Figure 16. An SEM image of the silicone modified with 3% wt black dye. The uniformly distributed small particles with diameters ranging from 2 to 5 μm can increase the light absorption of the silicone.

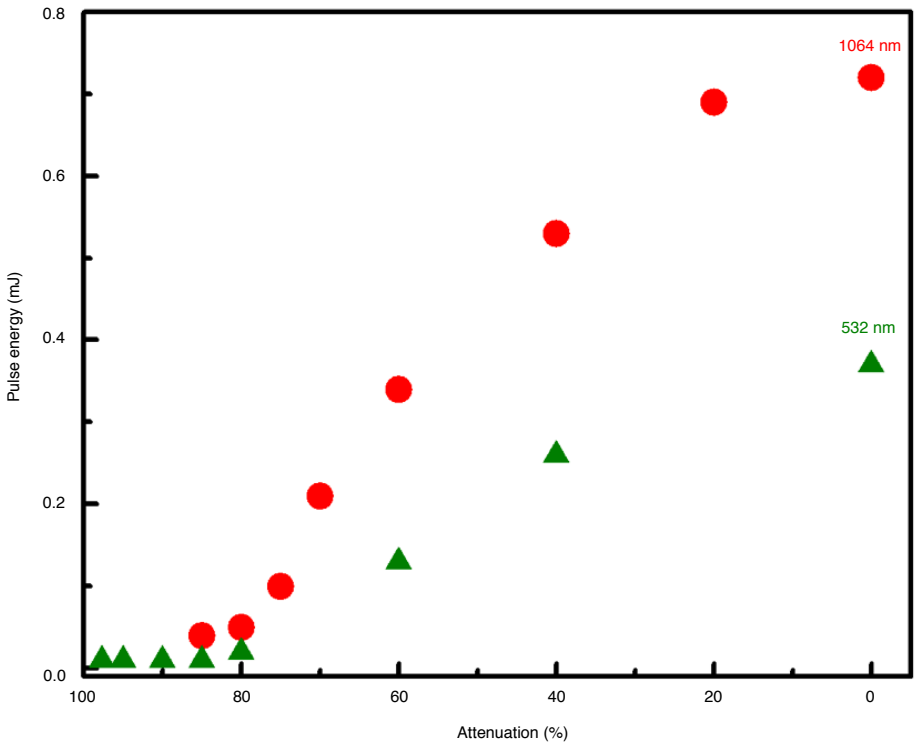

Supplementary Figure 17. Laser pulse energy controlled by the lens attenuation system. The Nd:YAG laser pulse energy is calibrated by an energy meter.

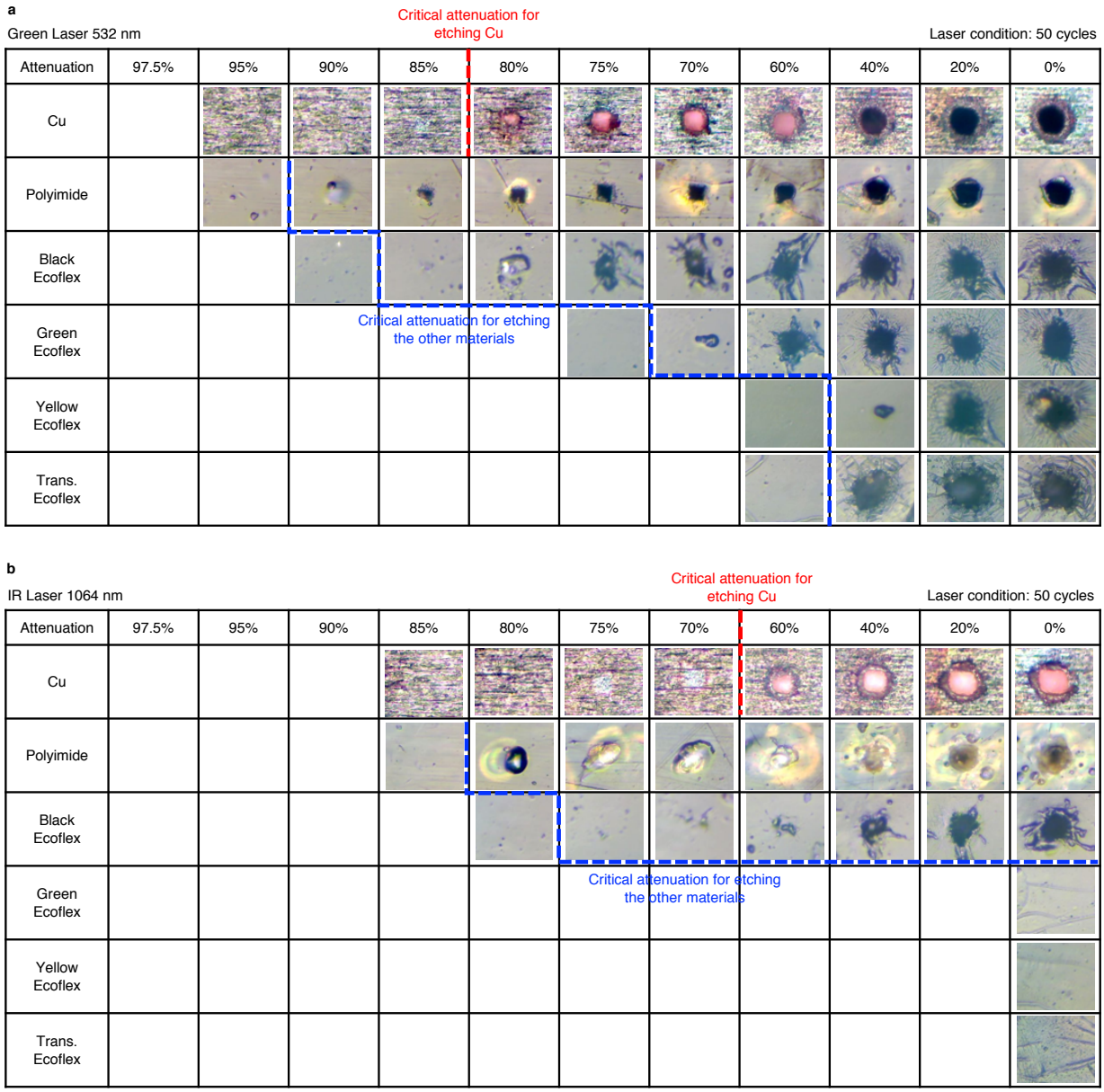

Supplementary Figure 18. Ablation of different materials with laser wavelengths of (a) 532 nm and (b) 1064 nm. The red lines are the critical attenuation that can ablate Cu. The blue lines are the critical attenuation for ablating other materials. For 532 nm, it can be used to etch Cu, PI, and silicone without and with dye modifications. For 1064 nm, it is suitable to etch Cu, PI, and the silicone modified with only the black dye. Materials, whose critical attenuation is larger than Cu, can be selectively ablated in the presence of Cu.

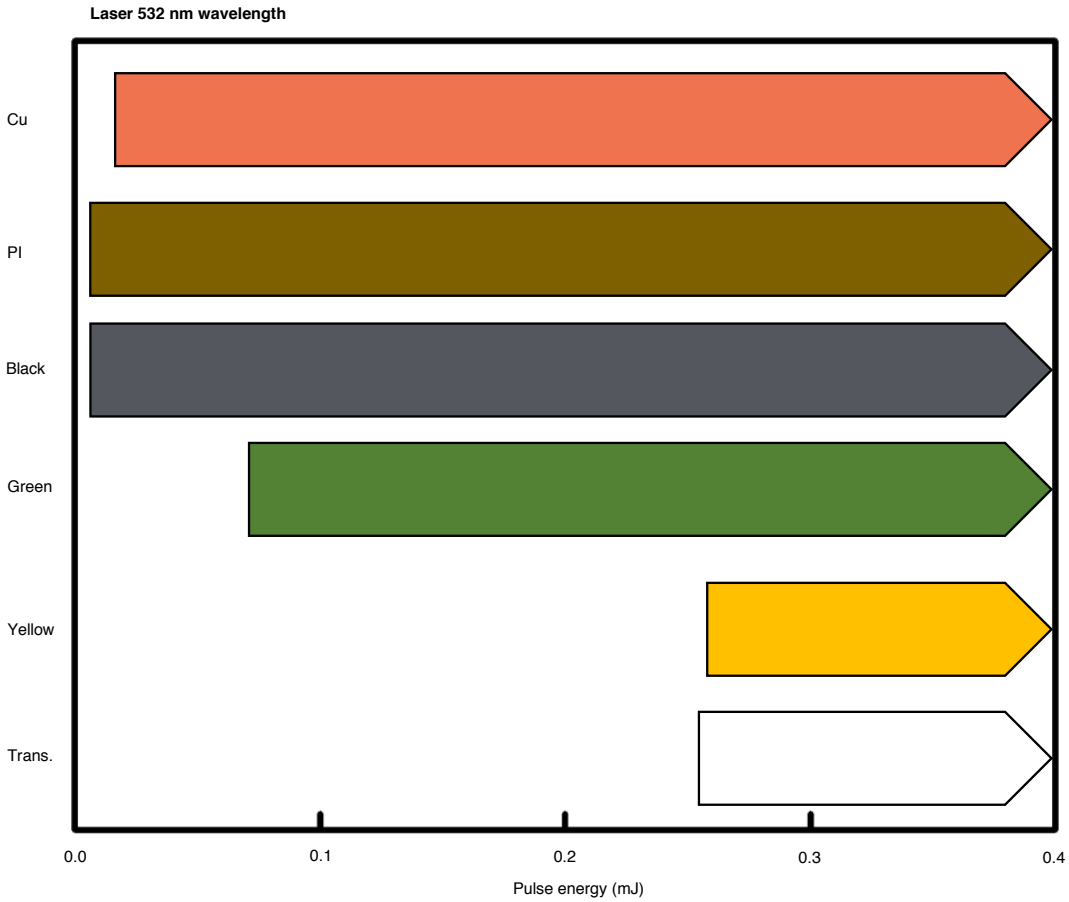

Supplementary Figure 19. Ablation pulse energy of the laser with 532 nm wavelength for Cu, PI, and silicone with different colors. The threshold pulse energies for Cu, PI, and black silicone are too close to allow selective ablation.

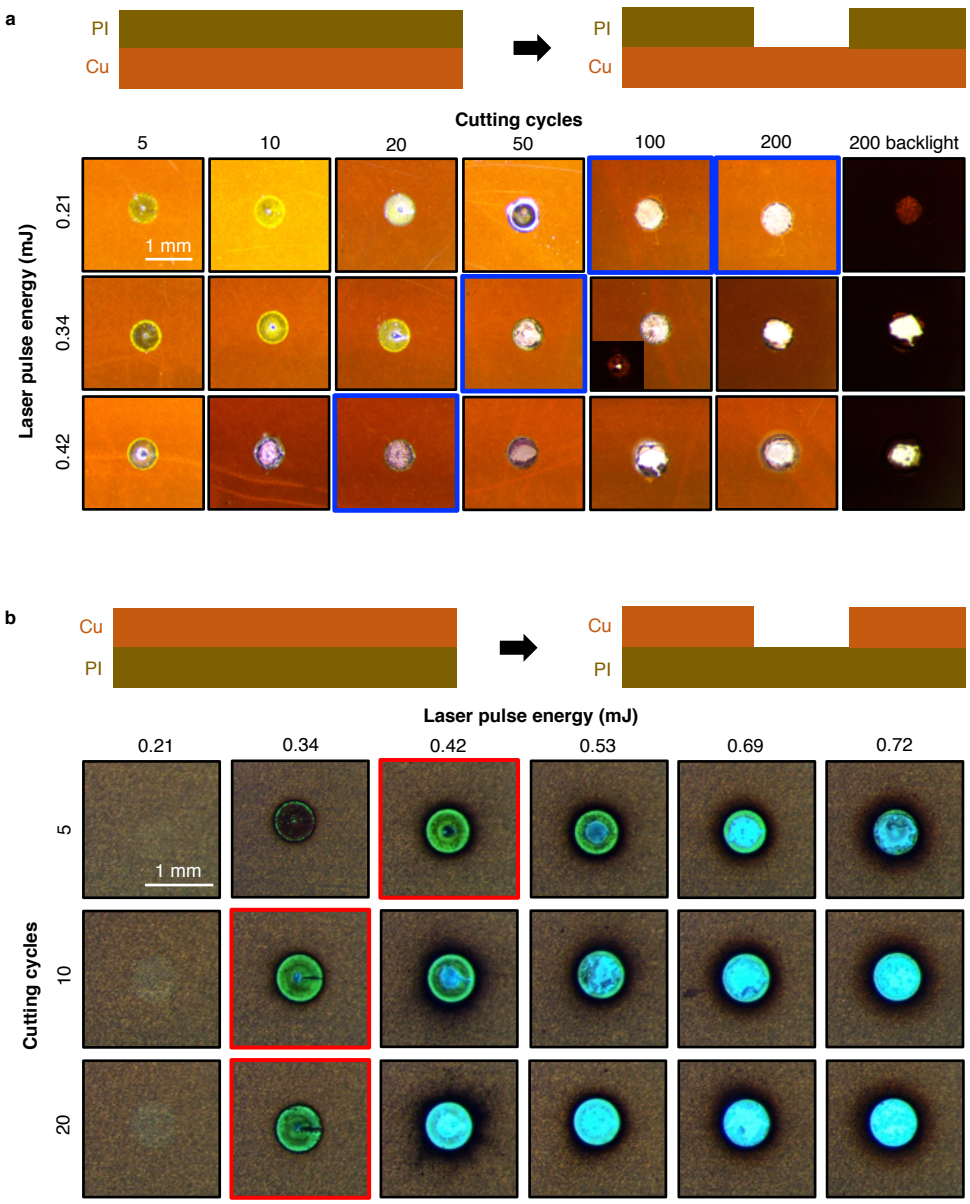

Supplementary Figure 20. Selective laser ablation of Cu (~20 μm) and PI (~14 μm). Laser (1064 nm) with different pulse energies or ablation cycles is used to selectively remove PI on Cu (**a**) or Cu on PI (**b**). As the critical pulse energy for PI (0.05 mJ) is lower than Cu (0.34 mJ), it's easy to selectively remove PI from the bottom Cu by controlling the laser pulse energy at 0.21 mJ. No matter how many processing cycles are used, the bottom Cu is still safe, as shown in the first row of (**a**). To remove Cu from PI is very tricky, but can be achieved by controlling the processing cycles. If more cycles are used, the bottom PI will also be ablated, as shown in (**b**).

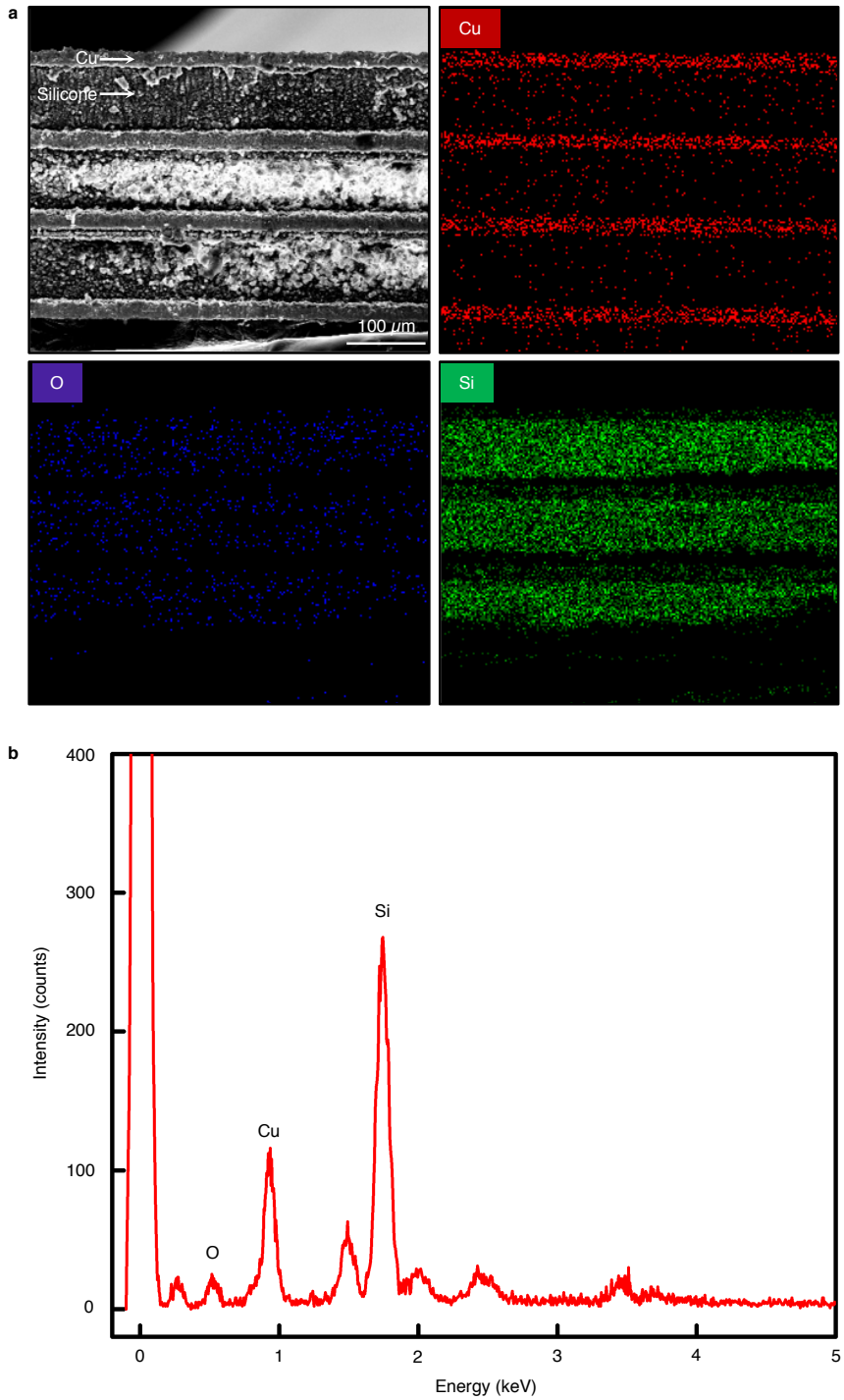

Supplementary Figure 21. Multilayer Cu insulated by soft silicone to fabricate the VIAs. a, A SEM image and corresponding EDS mapping graphs of the multilayer structure. **b**, EDS spectrum showing the elements included in the sample.

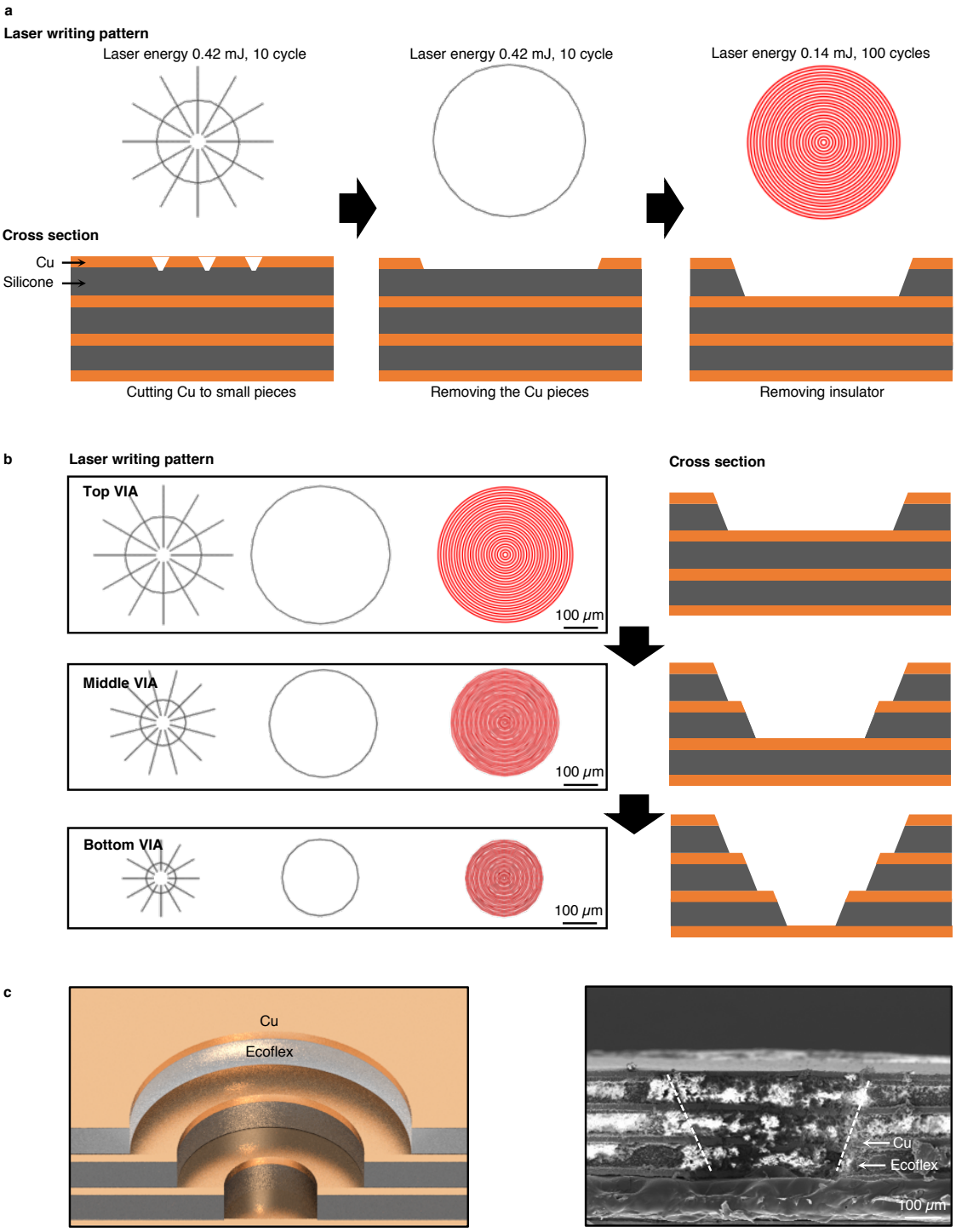

Supplementary Figure 22. Design of laser (1064 nm) ablation process for selectively ablating Cu and black silicone to build a through VIA. a, Laser cutting pattern design (top row) and corresponding schematics showing the ablation results (bottom row). With the first pattern, Cu will be cut into small pieces. With the second pattern, Cu will delaminate from the silicone substrate automatically, due to the residual thermal stress. **b**, Serial pattern designs to build the through VIA. **c**, Schematics (left) and an SEM image (right) of the through VIA.

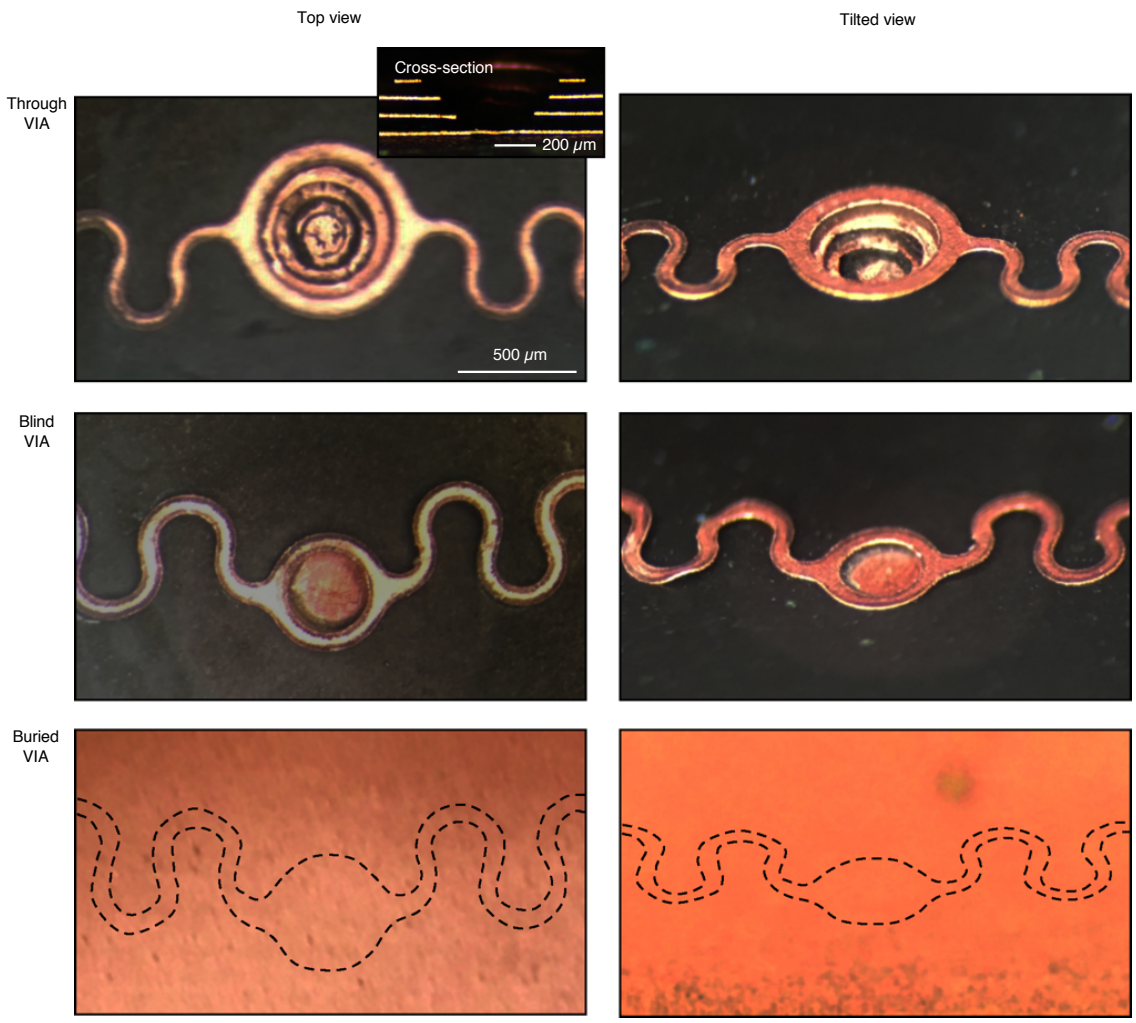

Supplementary Figure 23. Images of all three types of VIAs. Optical images show the top view and tilted view of the VIAs. All images share the same scale bar. The inset figure shows the cross-section of the through VIA.

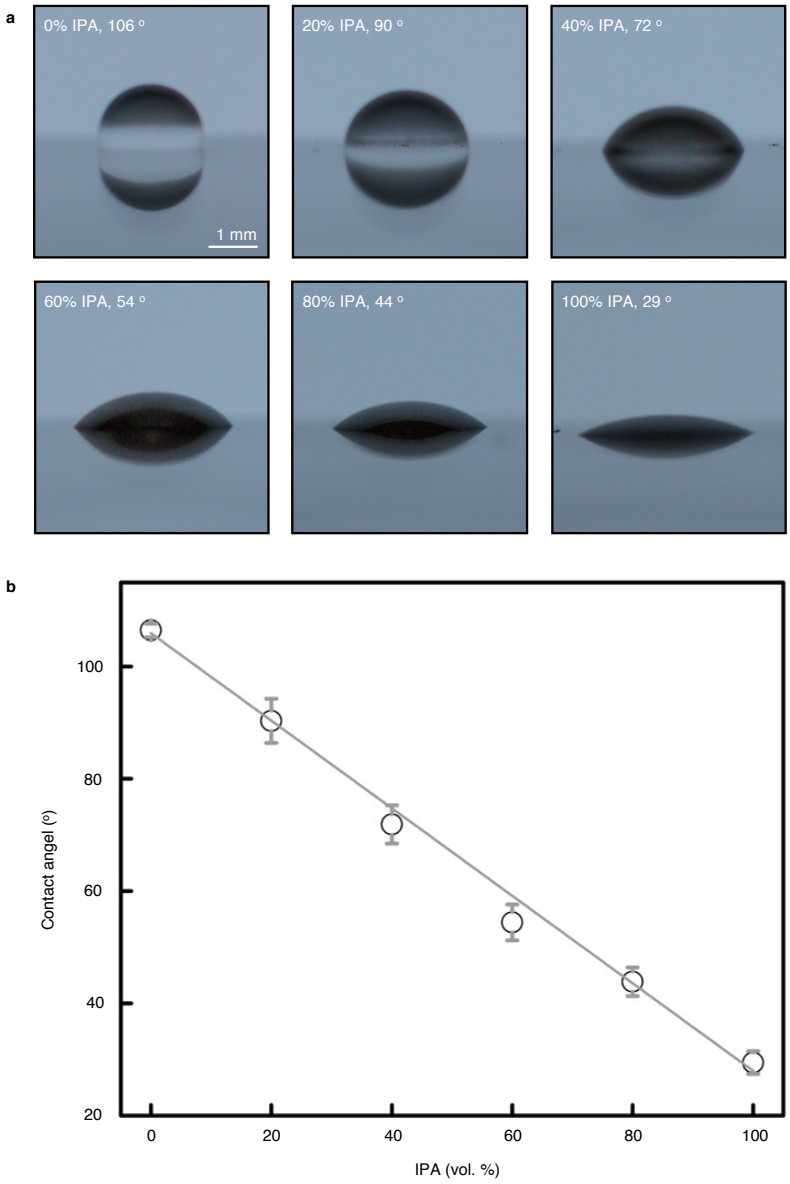

Supplementary Figure 24. Control of the contact angle of flux (aqueous solution) with silicone (black Ecoflex) by mixing with IPA. a, Images showing the contact angle of flux mixed with IPA of volume percentile from 0% to 100%. All images share the same scale bar. **b**, The linear relationship between the contact angle and the IPA volume percentile.

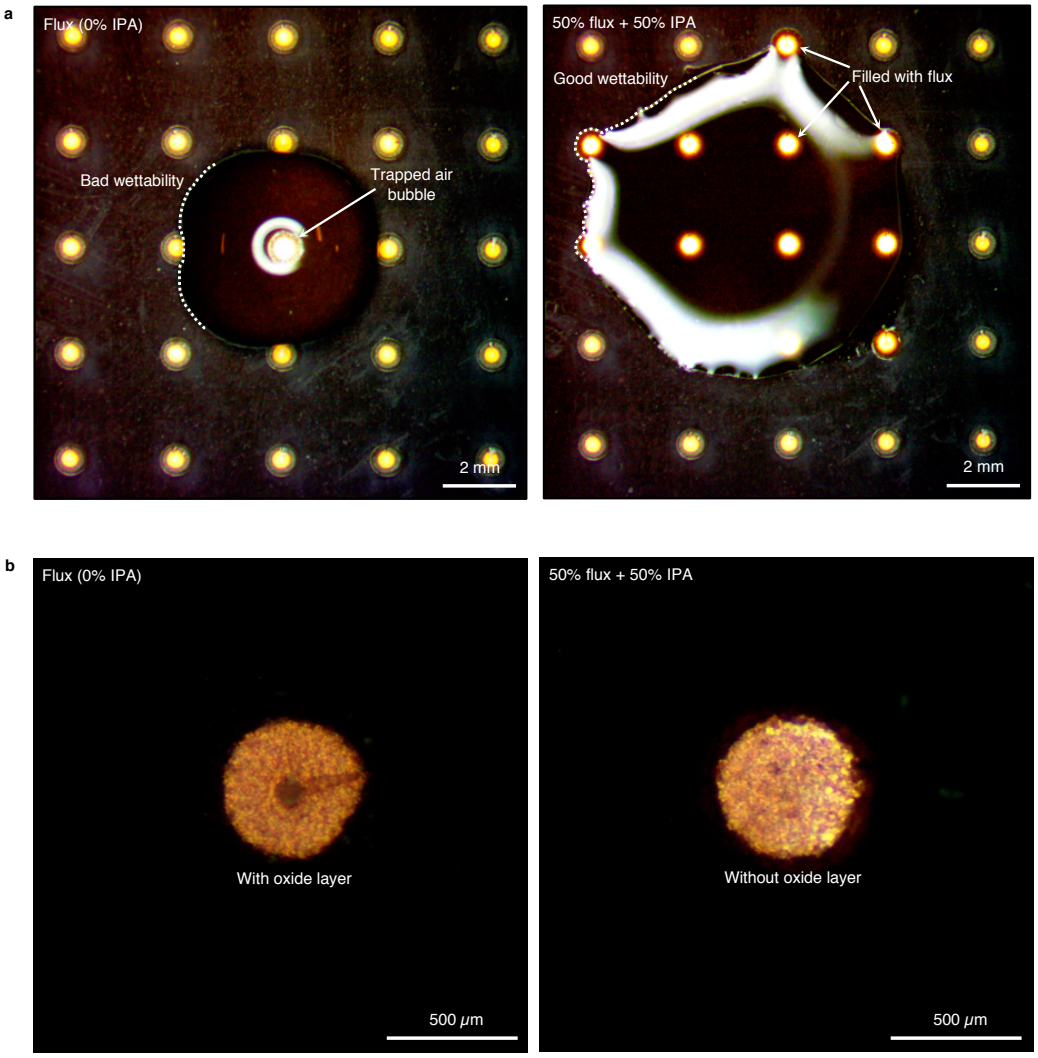

Supplementary Figure 25. Comparison of the VIA surface with and without Cu oxide by flux. a, Wettability of flux only (left) and 50% flux + 50% IPA (right). The flux cannot go into the VIAs due to its large contact angle with silicone. With 50% IPA, the contact angle decreases, which improves the wettability on silicone. Each droplet volume is ~80 μL. **b**, The comparison of cleaned Cu surfaces with flux only (left) and 50% flux + 50% IPA (right).

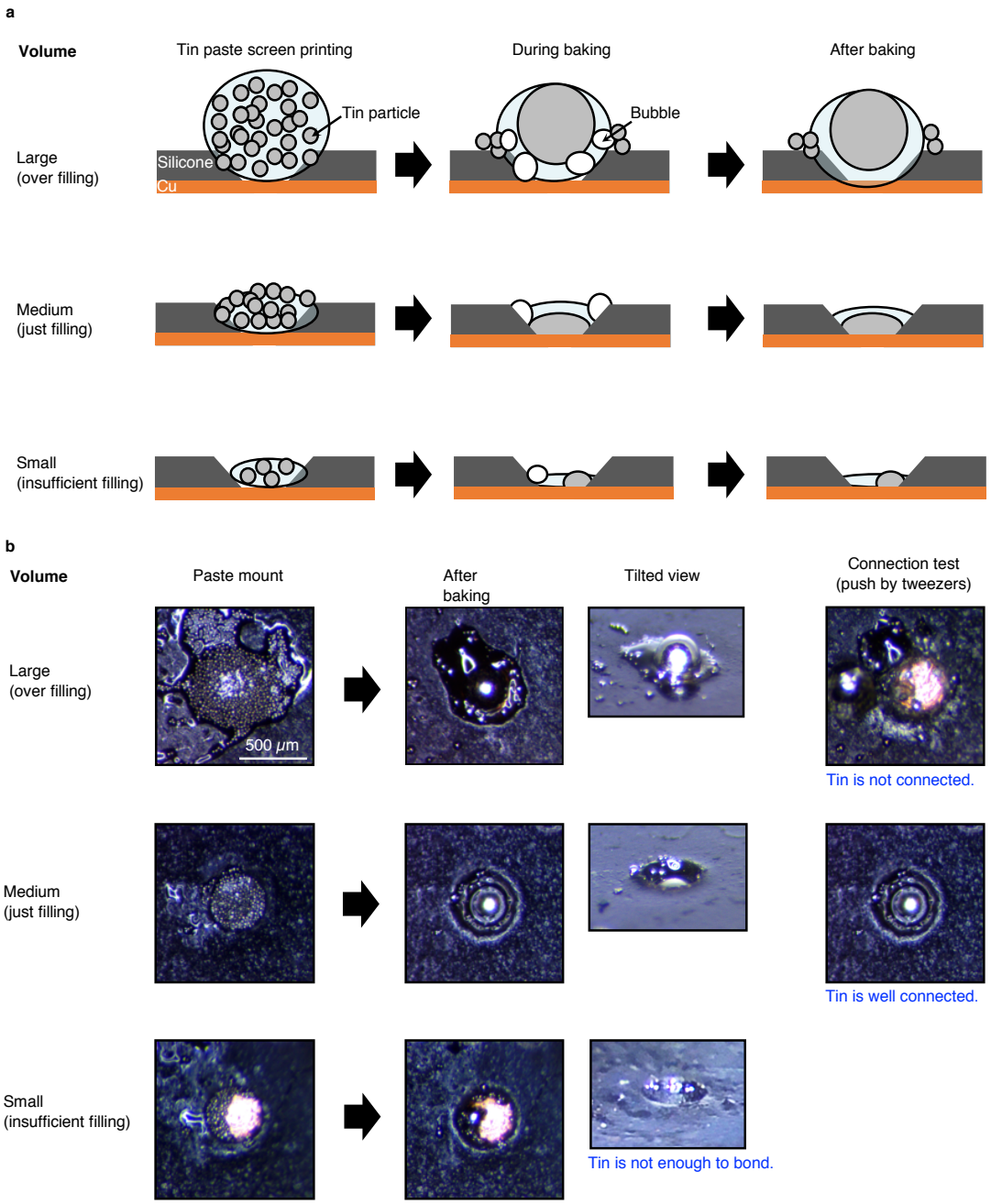

Supplementary Figure 26. Schematic illustration of curing the tin paste with different amounts by screen-printing. a, During baking, small tin particles will melt and merge to form big tin balls. At the same time, the flux will boil and generate some bubbles. If there is too much paste, the flux will generate too many bubbles that will push the tin ball to separate from the bottom Cu. On the other side, if the paste amount is not enough, it will not be able to cover the entire bottom Cu pad surface. Therefore, a suitable amount of paste is necessary to form robust and reliable bonding with the exposed Cu pads. **b**, Experimental results showing the bonding behavior. All images share the same scale bar.

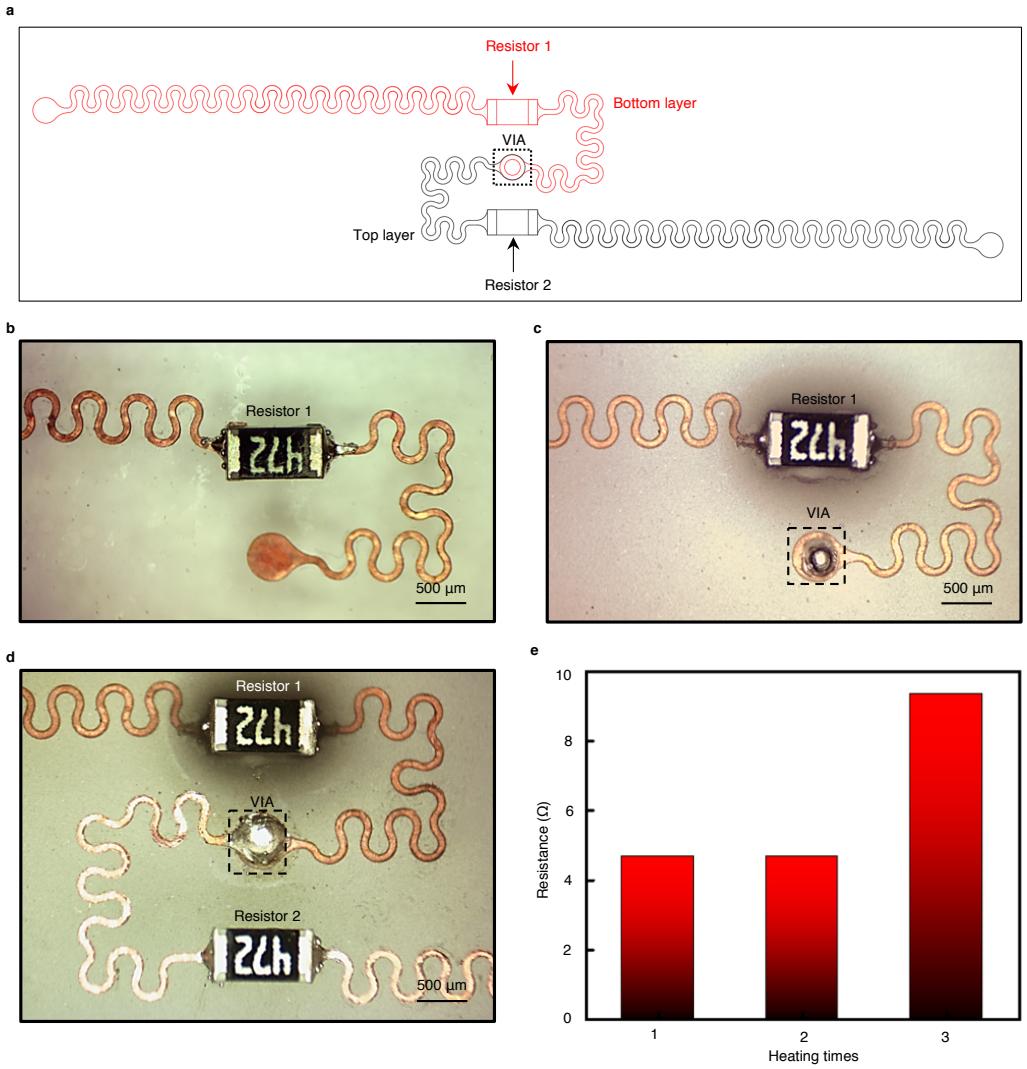

Supplementary Figure 27. Electrical performance testing after thermal expansion of the Ecoflex. We designed a simple experiment to test how the second heating impacts the previously soldered parts. Electrical characterizations were carried out after each separate fabrication step. **a**, Circuit diagram with two 4.68 kΩ resistors in two separate layers that are connected by a VIA. **b**, Image of the bottom layer after bonding (first heating). **c,** Image of the bottom layer after the tin VIA formation (second heating). **d**, Image of the two-layer circuit after the second layer bonding (third heating). **e**, Resistance value during the circuit fabrication process. The series resistance exactly equal to the sum of the top and the bottom resistance value. That means the second heating did not change the value of the firstly-soldered part, or likely to damage it.

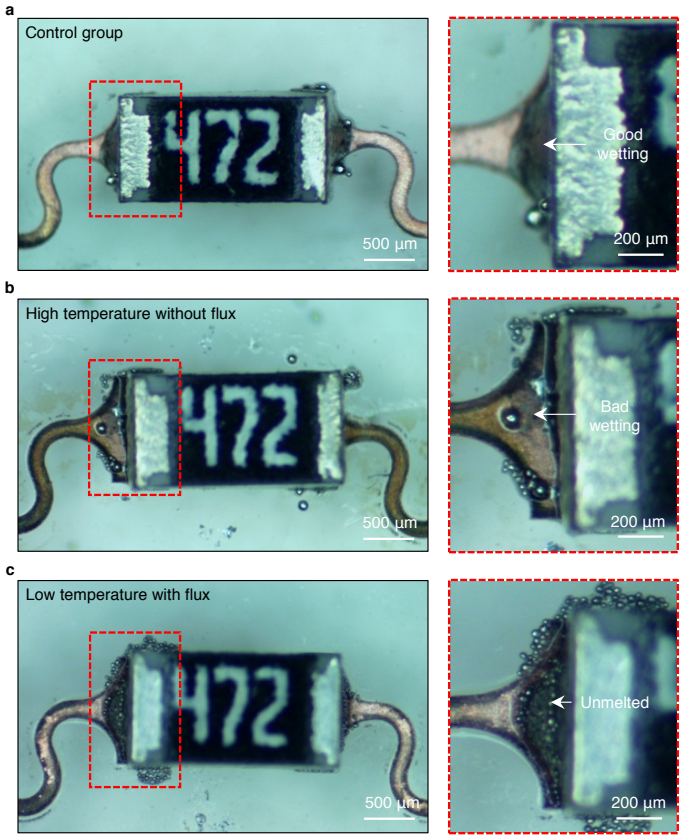

Supplementary Figure 28. Comparison experiments to highlight the influence of flux cleaning and reflow temperature on the welding behavior. a, Solid and strong alloy bonding formed by using flux to remove the copper oxide and high reflow temperature (150 °C), which results in good wetting on the contact pad (right panel, the zoomed-in image of the left pin of the resistor). **b**, Poor wetting behavior with high temperature (150 °C), but without flux cleaning. The presence of copper oxide precludes the alloying between tin and copper. Therefore, the solder beads up on the contact pad and the chip is displaced from the contact pad (right panel, the zoomed-in image of the left pin of the resistor). **c**, Incomplete solder paste melting by low reflow temperature (140 °C), resulting in poor bonding and possibly an open circuit (right panel, the zoomed-in image of the left pin of the resistor). The flux can help remove the copper surface oxide, which would otherwise prevent the formation of solid alloys at the interface and thus lead to large contact resistance and weak bonding. Temperature has to be controlled carefully to melt the $Sn_{42}Bi_{57.6}Ag_{0.4}$ paste. If it is too high, it melts the solidified alloys in previous layers. If it is too low, the solder paste does not melt thoroughly.

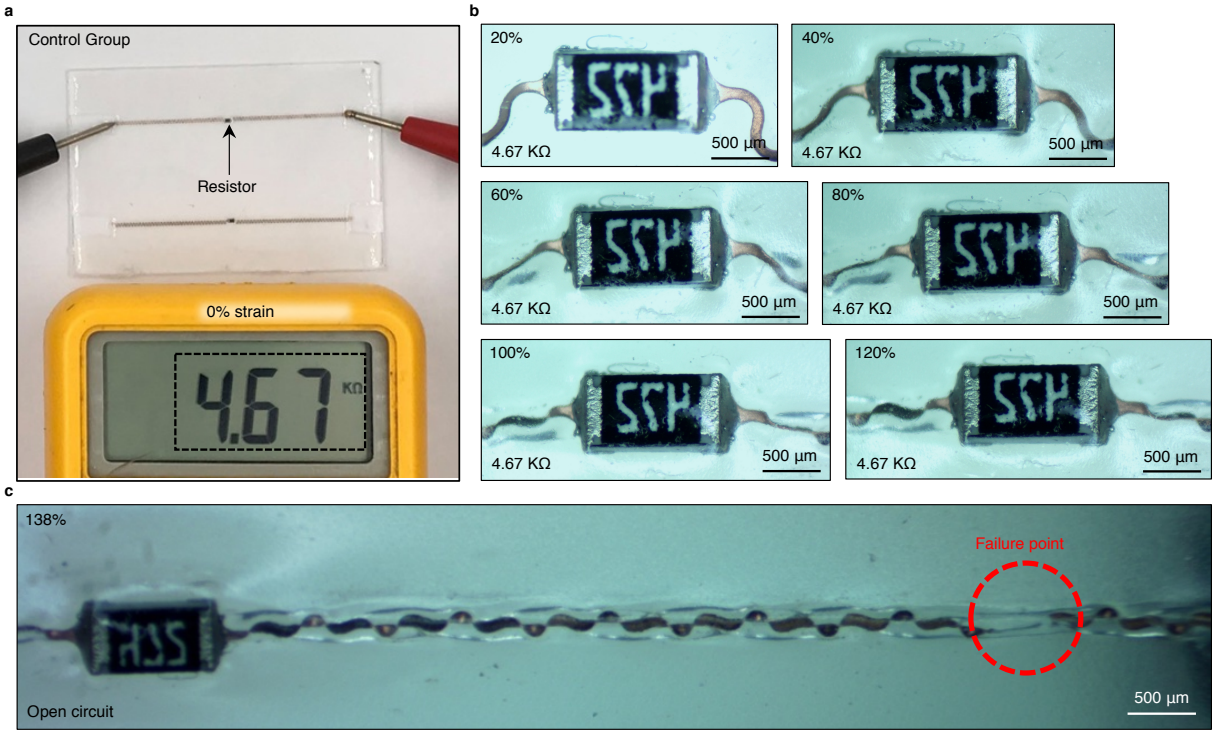

Supplementary Figure 29. Electromechanical testing of the bonding strength between the chip and the interconnect pads. To characterize the robustness of the bonding between rigid chips and interconnects, the sample bonded with high heating temperature (150 °C) and flux treatment was used to test its stretchability. **a**, Resistance measurement with 0% strain. **b**, Continuous resistance measurements from 20% to 120% tensile strain, showing the mechanical robustness of the entire device. **c**, The failure strain of the device is determined to be ~138%. During the entire stretching process, the interface bonding between the rigid chip and interconnect pads was very stable and did not show any evidence of delamination. The serpentine interconnect was broken before the bonding between the rigid chip and interconnect pads fails, when it was stretched to 138%.

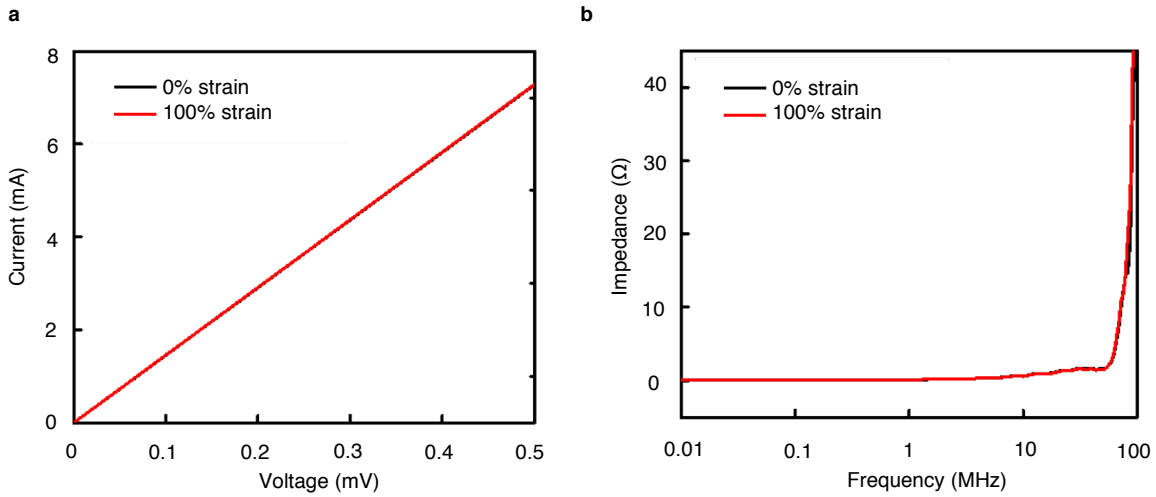

Supplementary Figure 30. High electrical performance of the VIAs. The laser ablation and solder paste injection methods form the VIAs through thick (100 μm) and stretchable silicone. The as-formed VIAs were used to connect circuits in different layers, adjacent and non-adjacent. Besides, the VIA material was $Sn_{42}Bi_{57.6}Ag_{0.4}$ metal alloy, which had very high conductivity. Furthermore, when heated, a layer of Cu-Sn alloy will form between the VIA and the copper interconnects (for both top and bottom copper wires), which built strong bonding between the VIAs and the interconnects in different layers and made the VIAs very stable. **a**, I-V curves of the VIA before and after stretching (100% strain). The straight line means it is an ohmic contact between the VIA and copper interconnects. The resistance of the VIAs is only round 68.7 mΩ. The overlapped two lines indicate the resistance didn't change noticeably with the strain from 0% to 100%. **b**, VIA impedance spectroscopy under free standing and 100% tensile strain states. The impedance increases with frequency, because of the skin effect for r.f. transmission wires and the increased inductive reactance value at higher frequencies (inductive reactance $X_L = 2\pi fL$, where f is the frequency and L is the wire inductance). For our VIA, the impedance slightly increased when the frequency was higher than 1 MHz, and dramatically increased when the frequency was above 50 MHz.

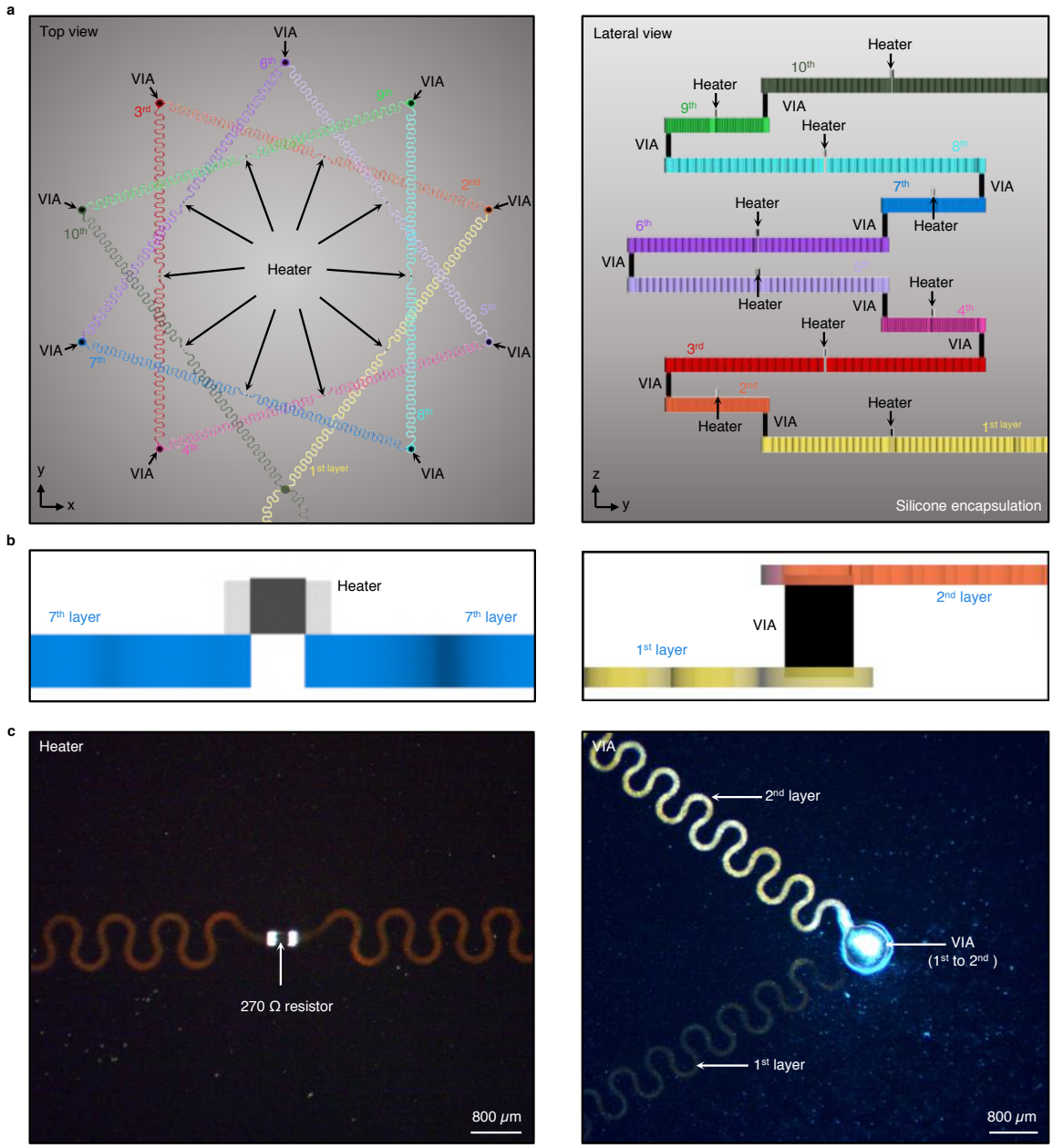

Supplementary Figure 31. Illustration of the 10-layer stretchable decagram device structure. a, Schematic top view (left) and cross sectional view (right) to show the multilayered device structure. The device has 10 layers, with a heater in each layer and a VIA vertically connecting the adjacent layers in series. The entire device is fully encapsulated by silicone. (**b**) Detailed schematics and (**c**) optical images of the heater (left) and VIA (right).

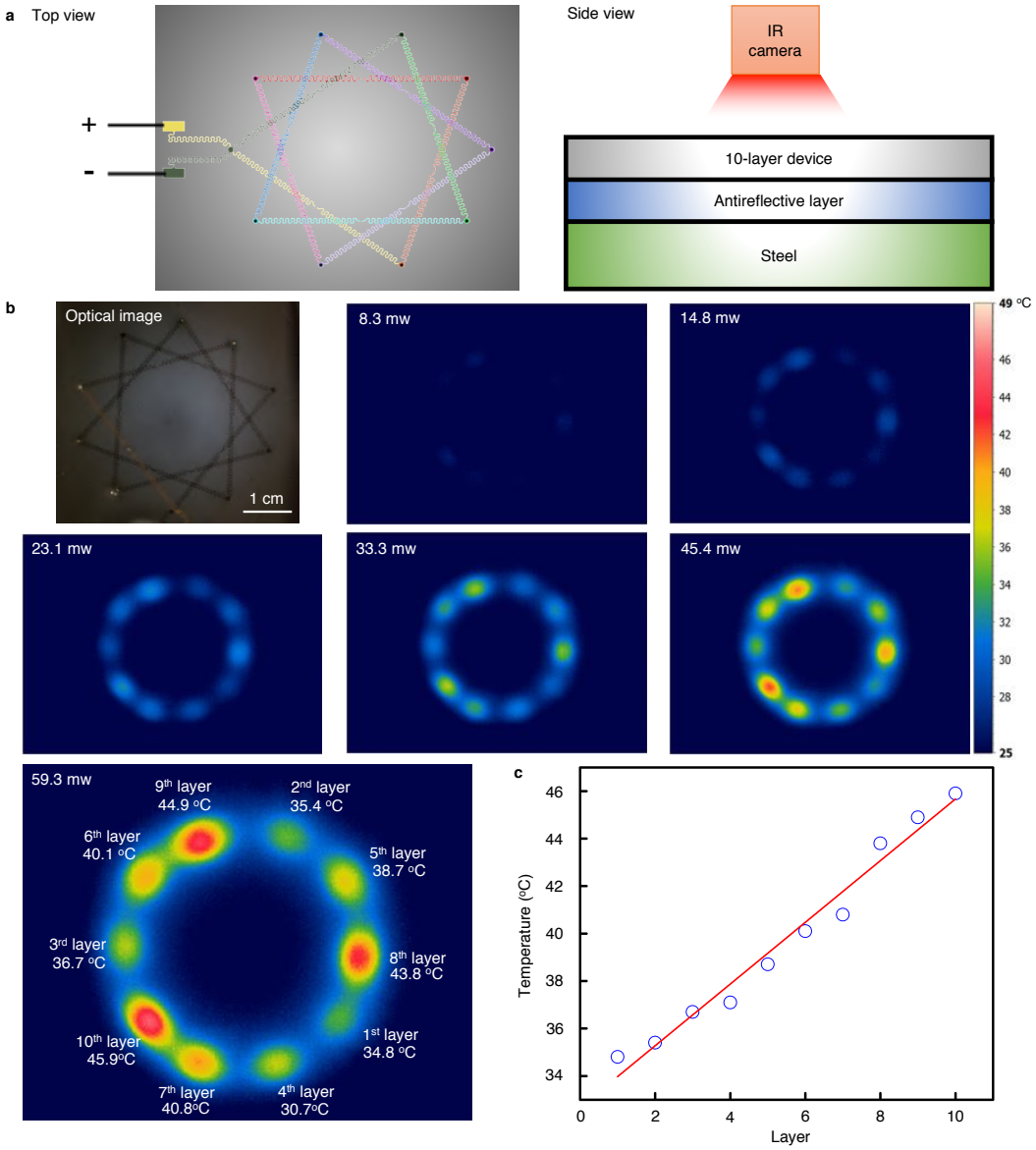

Supplementary Figure 32. Thermal imaging setup for the 10-layer stretchable decagram device. a, Schematic top and cross-sectional views of the setup. An external DC supply is used to drive the device. An IR camera (Therm-App® TH, resolution 384x288 pixels, sensitivity < 0.07 K) is used to image the temperature distribution on the device surface. A steel board at the bottom is used as the heat sink to increase the thermal dissipation of the device. An antireflective layer (a white paper or black plastic) is used to decrease the IR reflection from the environment. **b**, Thermal images of the device with different heating power. **c**, Temperature summary of heaters in different layers.

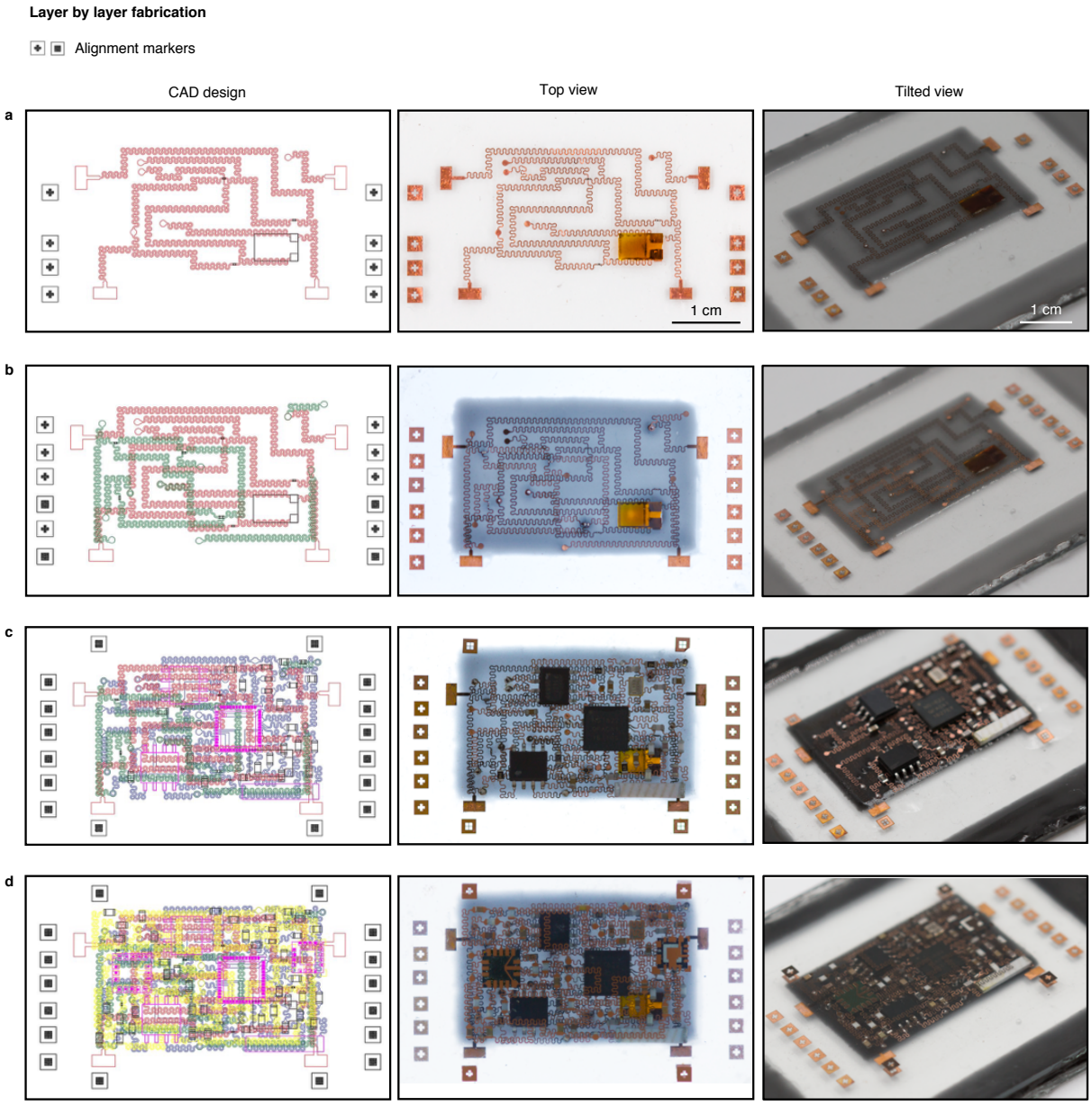

Supplementary Figure 33. Layer by layer fabrication process for the four-layer stretchable system. The images show the fabrication process from the **(a)** 1st layer to the **(d)** 4th layer, in CAD design (first column), device top view (second column), and device titled view (third column).

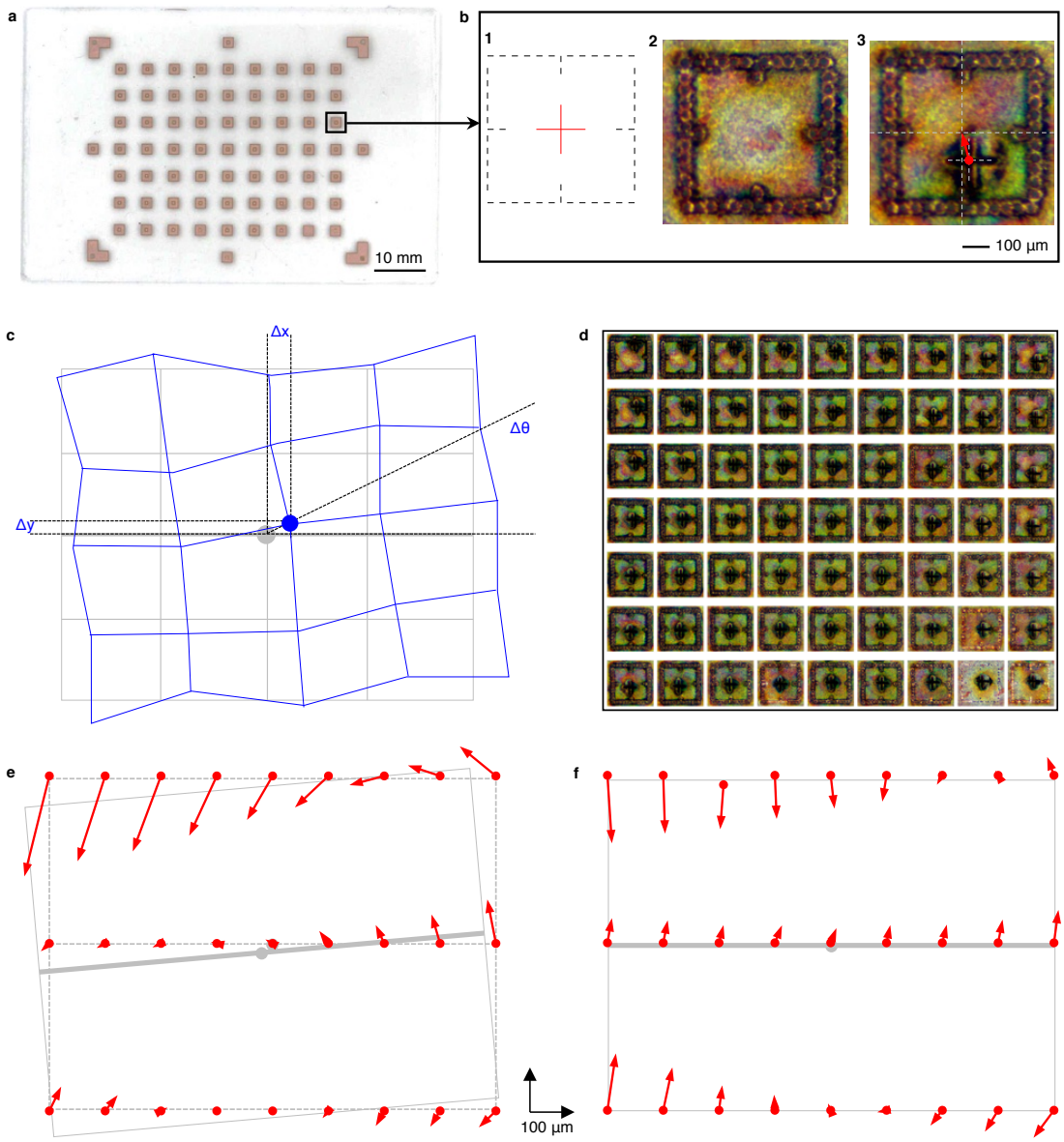

Supplementary Figure 34. Evaluation of interconnection distortion during the transfer printing process. a, Overview of a test sample. **b**, (1) Alignment marker design, the black line for 1st ablation (before transfer) and the red line for 2nd ablation (after transfer); Examples of actual laser marker (2) before transfer and (3) after transfer. Red vector shows the location discrepancy between the 1st and the 2nd ablations. **c**, Schematic laser alignment error (with horizontal shift Δx, vertical shift Δy, and rotation Δθ) and sample distortion after transfer. **d**, A compiled photo of alignment markers at each location. **e**, The arrows show the total misalignment between the 1st and 2nd laser ablation patterns, which include both the laser alignment error and transfer distortion. By calculation, the location discrepancies and laser alignment error are Δx, Δy, Δθ: -29 µm, -24 µm, 0.14°, respectively. **f**, Transfer distortion, regardless of the laser alignment. (Maximum distortion: 152 µm, Average distortion in rms: 14 µm).

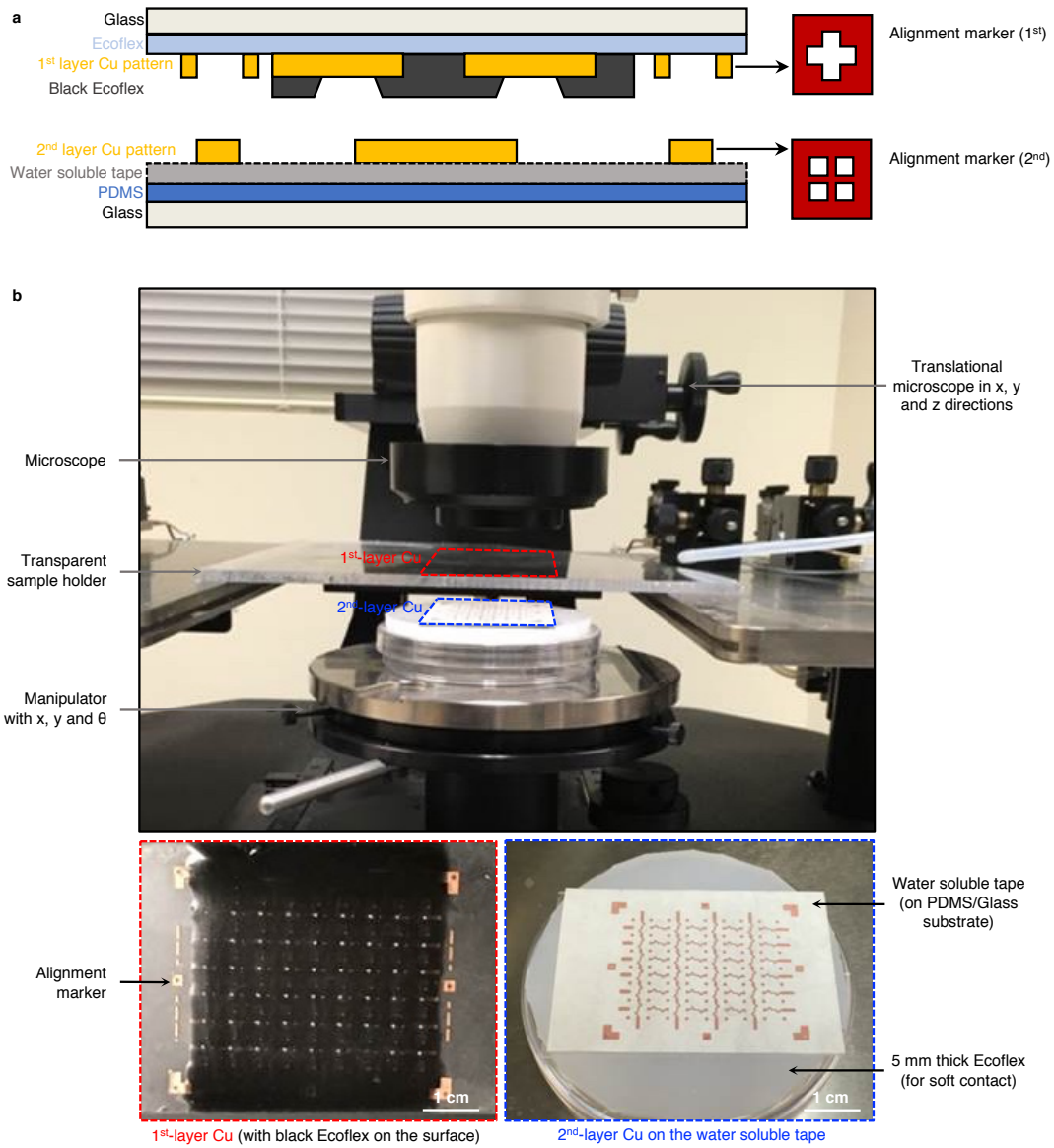

Supplementary Figure 35. Setup for aligned transfer printing. The multilayered device is fabricated layer by layer. The subsequent layer should be well-aligned with the existing layers for VIA connections. **a**, Schematic illustration of the alignment. Every layer has the marker for alignment. The layer to be transferred is on water soluble tape and fixed by PDMS temporarily. **b**, The alignment system, composed of a microscope and a mechanical stage. The first layer is fixed on a transparent holder and the second layer is placed on a 5 mm thick Ecoflex. The Ecoflex is used as the buffer for soft contact with the first layer, which will protect the sample from excessive pressure.

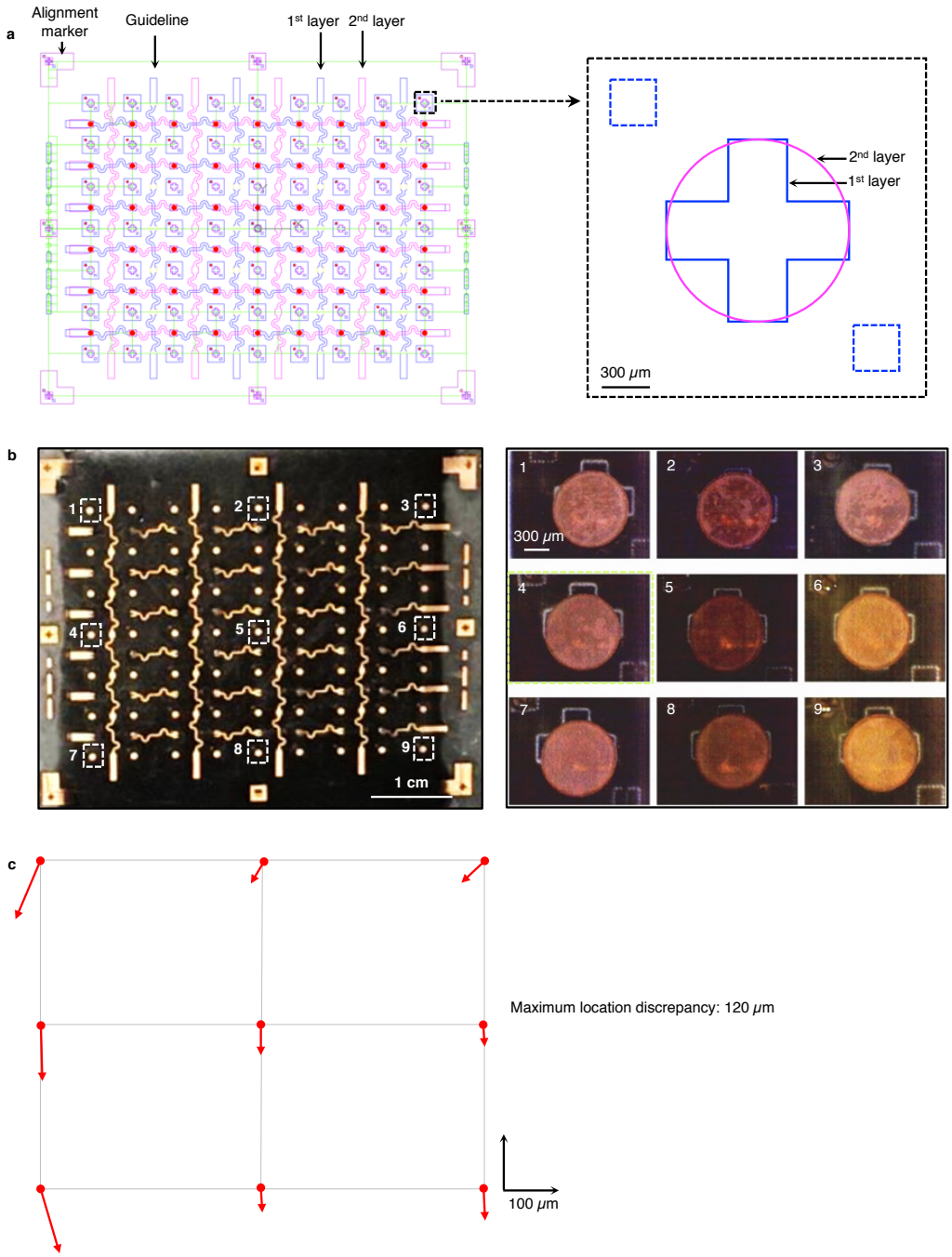

Supplementary Figure 36. Error evaluation of aligned transfer printing. a, Two-layer pattern design for the transfer error evaluation. The blue layout is the first layer and the carmine layout is the second layer. Shown on the right is the ideal alignment of the markers. **b**, The integrated two-layer device after transfer printing. Shown on the right is the marker distribution on the device. After checking the marker shift, the aligned transfer printing error is evaluated, as shown in (**c**). The max error is ~120 μm.

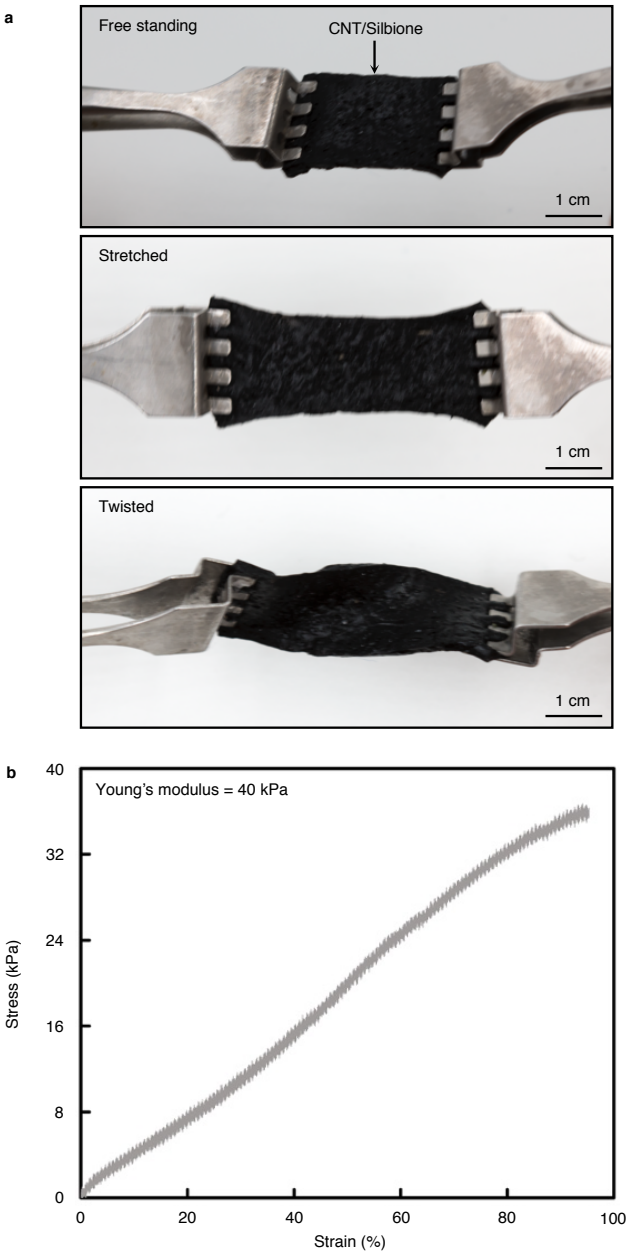

Supplementary Figure 37. Mechanical properties of the soft CNT/Silbione EP sensors. a, Optical images showing the sensor can be stretched and twisted. **b**, Stress vs. strain relationship of the EP sensor indicating its ultra-low Young's modulus of 40 kPa.

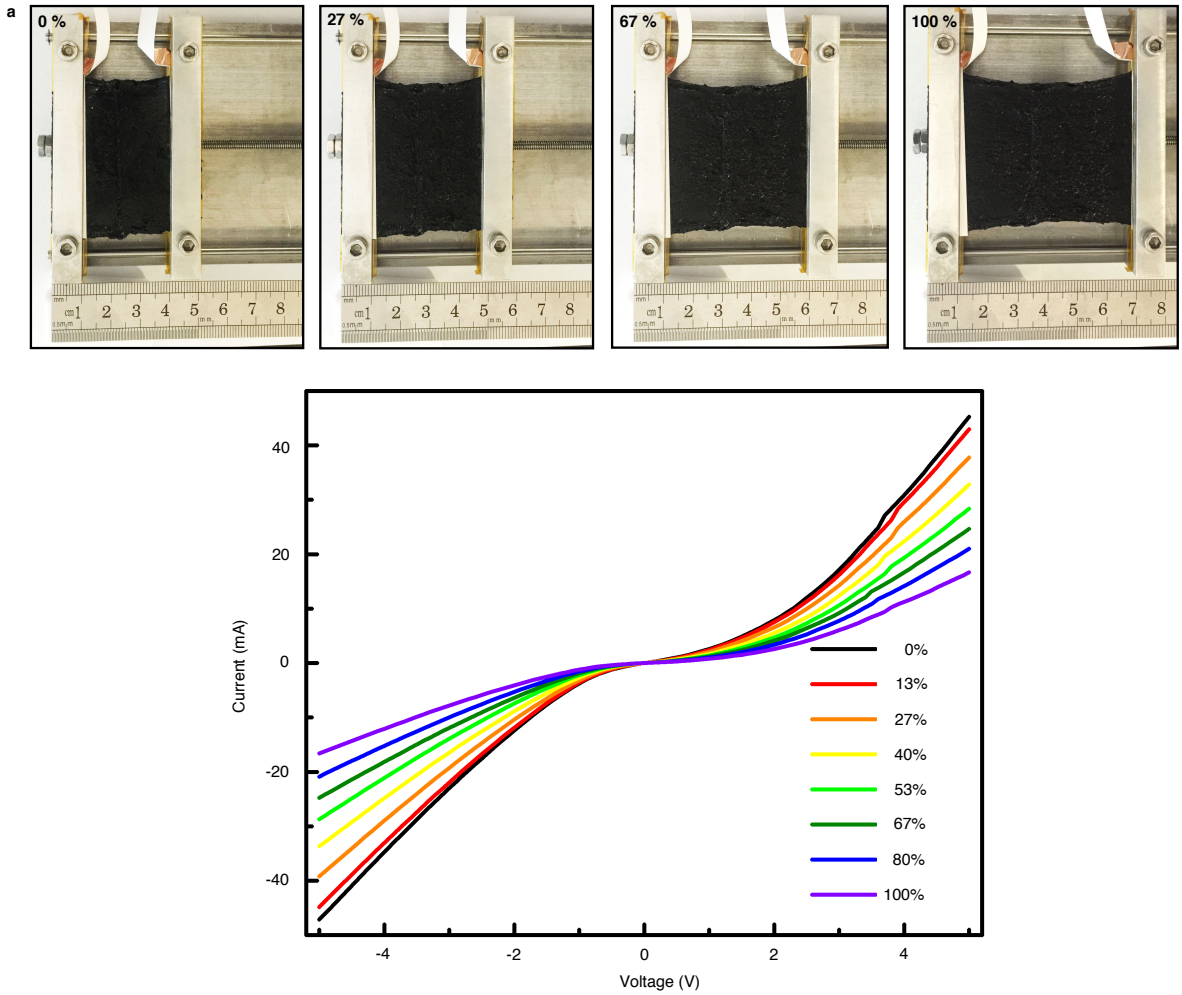

Supplementary Figure 38. Electrical properties of the soft CNT/Silbione EP sensors. a, Optical images of the sensor (with dimensions ~30×56×1 (L×W×T) mm^3) under different levels of uniaxial strain and associated I-V curves. **b**, The sensor itself can be used as a stretchable electrical connection to light up a LED at 3 V.

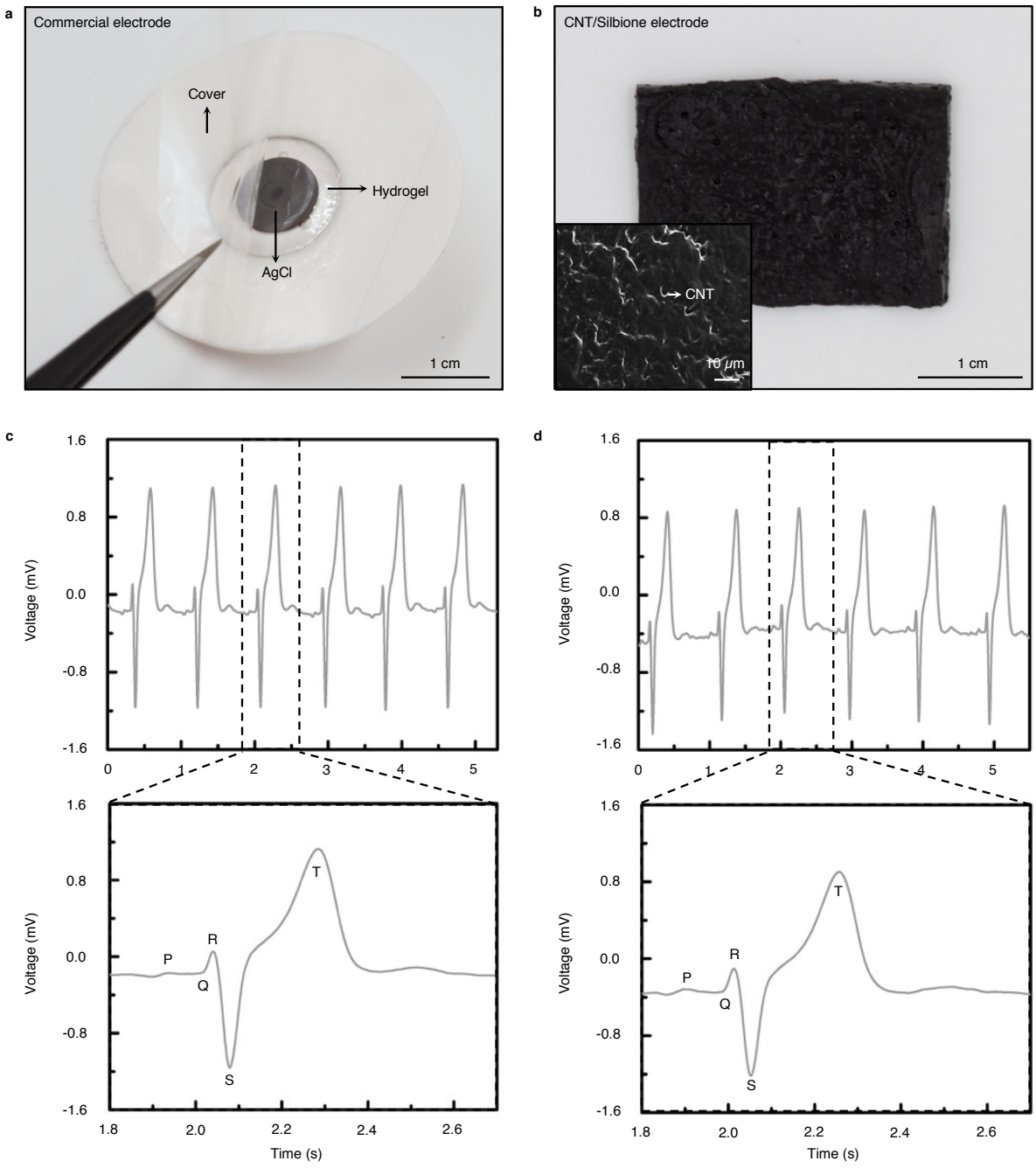

Supplementary Figure 39. ECG signals acquired with fresh commercial electrodes and homemade soft CNT/Silbione electrodes. The similar results of these two types of electrodes with high signal-to-noise-ratios (SNR) and the well defined P, Q, R, S, and T waveforms indicate the excellent sensing capability of the soft CNT/Silbione electrodes. Optical images of (**a**) the commercial AgCl/Ag-hydrogel electrode and (**b**) soft CNT/Silbione electrode, respectively. The inset of (**b**) shows the magnified CNT/Silbione composites in SEM. ECG signals acquired from the chest with (**c**) the commercial and (**d**) CNT/Silbione electrodes, respectively.

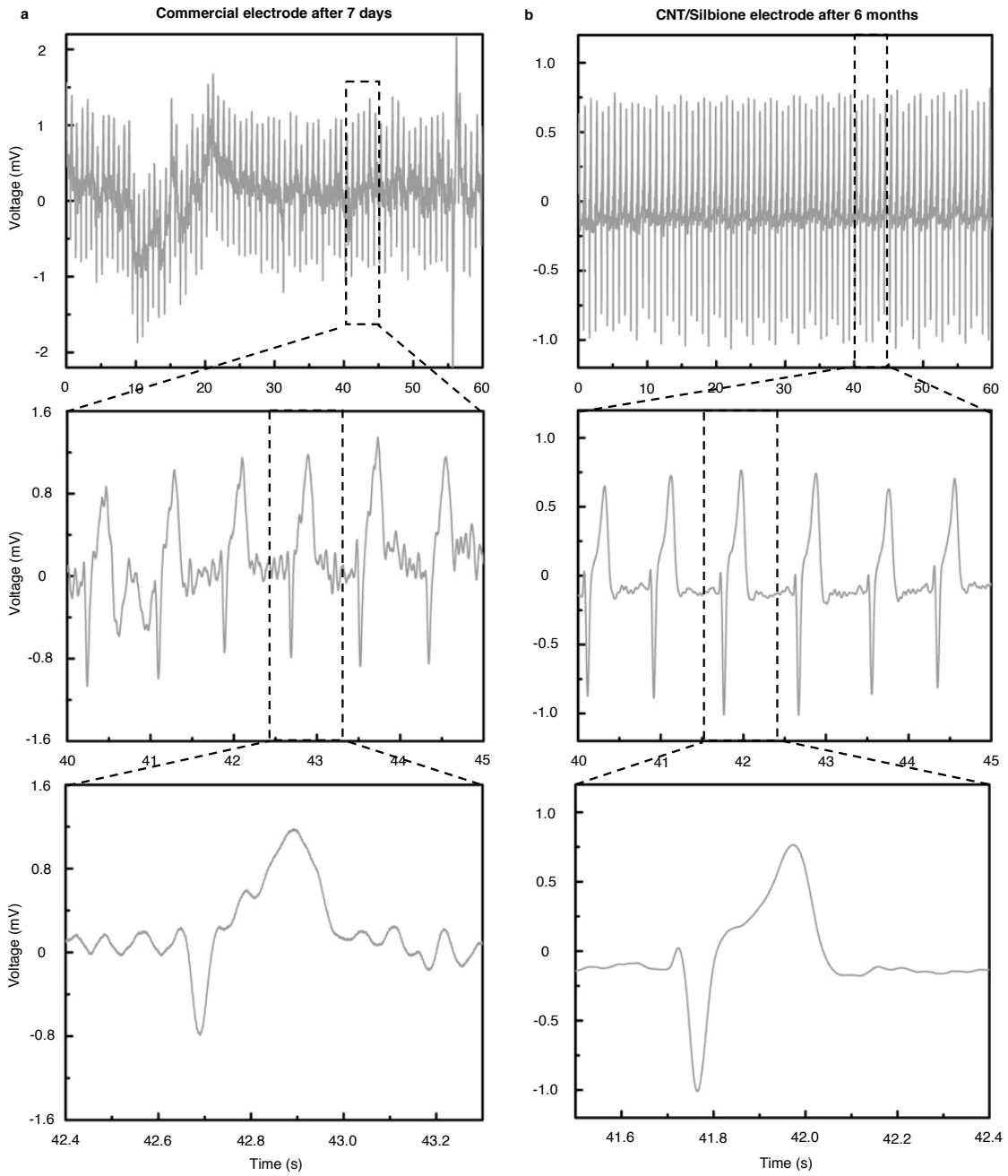

Supplementary Figure 40. Durability comparison between the commercial electrode and our soft CNT/Silbione electrode. a, The ECG signals acquired by the commercial electrode, which has been exposed in air for 7 days with the plastic covers removed. The fluctuating and noisy signals are due to the hydrogel that is dried out when exposed in air, which increases the impedance between the electrode and the skin. **b**, The stable ECG signals acquired by the CNT/Silbione electrode, which has been exposed to air for around 6 months, showing the electrode's superb durability.

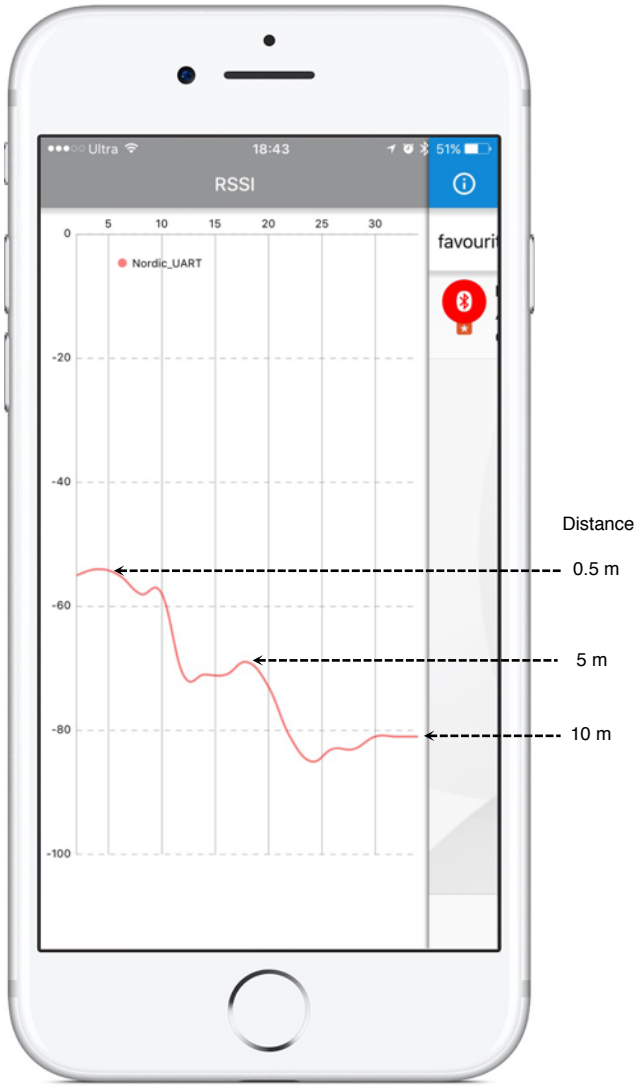

Hardware: iPhone 6 Plus; Software: NRF Connect

Supplementary Figure 41. Test of the Bluetooth signal strength from the multilayered stretchable device by the received-signal-strength-indicator (RSSI). The measurement hardware is a smartphone (iPhone 6 Plus with software NRF Connect).

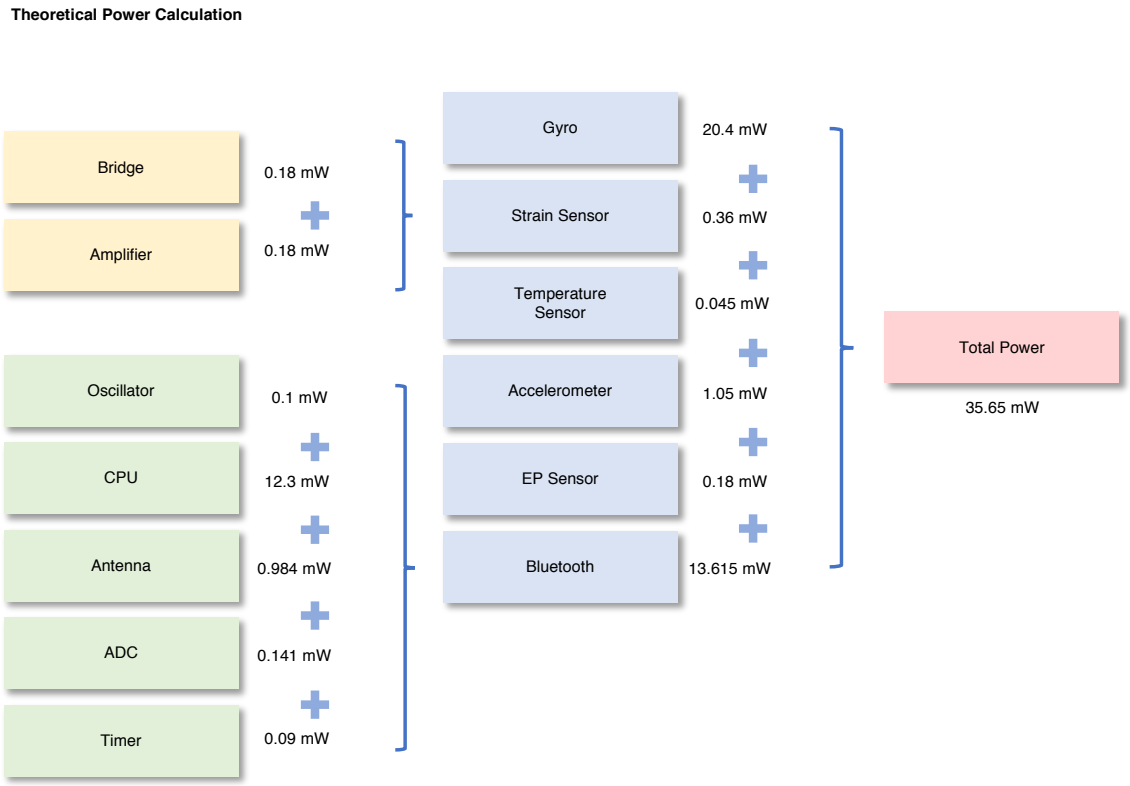

Supplementary Figure 42. Theoretical power calculation workflow and results. The total power dissipation is composed of six parts, including the gyro, strain sensor, temperature sensor, accelerometer, EP sensor, and Bluetooth. Only one main chip is used for these four parts: gyro, temperature sensor, accelerometer, and EP sensor part. Thus, the power consumption of each one of these parts can be calculated from the corresponding chips. The strain sensor, however, includes two parts, a bridge and an amplifier. Thus, its power consumption should be the sum of those two parts. Similarly, the power consumption of Bluetooth should be the sum of the six component chips. All the data are calculated from the official datasheet of the corresponding chips. The calculated total power is 35.65 mW (theoretical value).

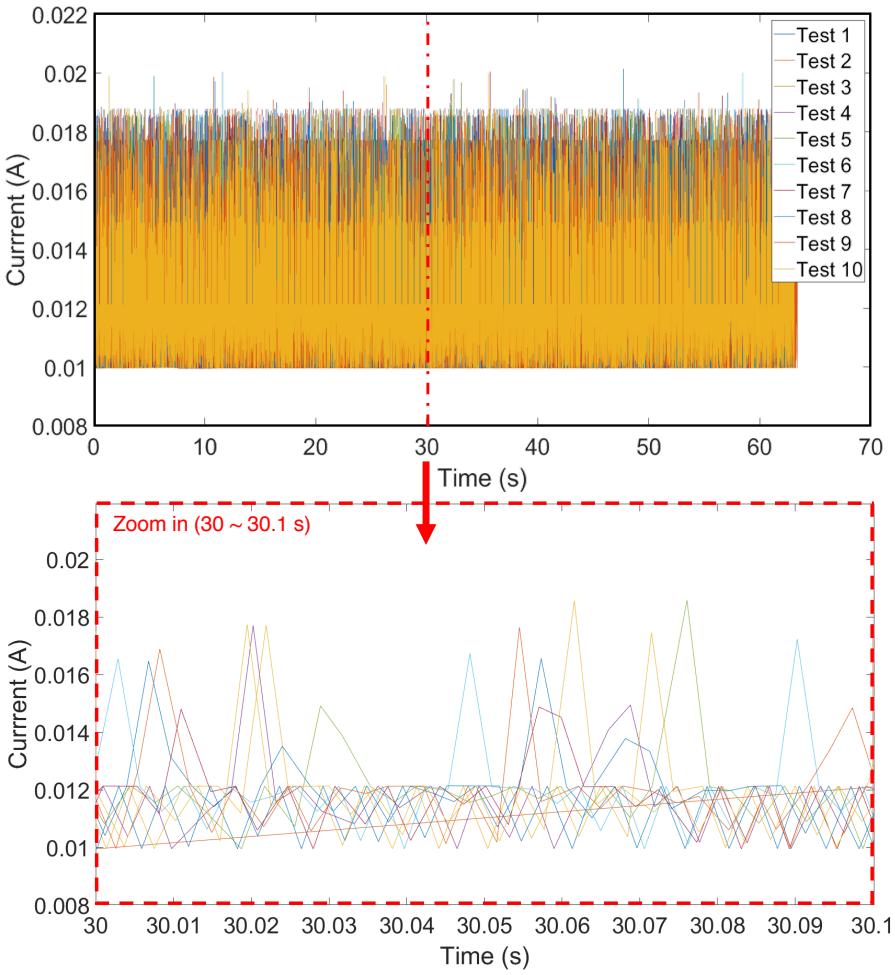

Supplementary Figure 43. Dynamic current consumption for the working device at 3 V DC supply. The current flow of the entire stretchable device was measured with a source meter (Keysight B2901). A DC voltage of 3 V was applied to drive the device. Data from 30~30.1 s is zoomed in to show the dynamic current consumption in each test. The average power was calculated by: $\overline{P} = \frac{1}{T} V \int_0^T I\,dt$, where $\overline{P}$ is the average power, V is the device working DC voltage, I is the working current, and T is the total time of one test. Ten tests were carried out to calculate the average power dissipation, which was around 35.62 mW (experimental value), which is very similar to our theoretical value 35.65 mW (Supplementary Fig. 42).

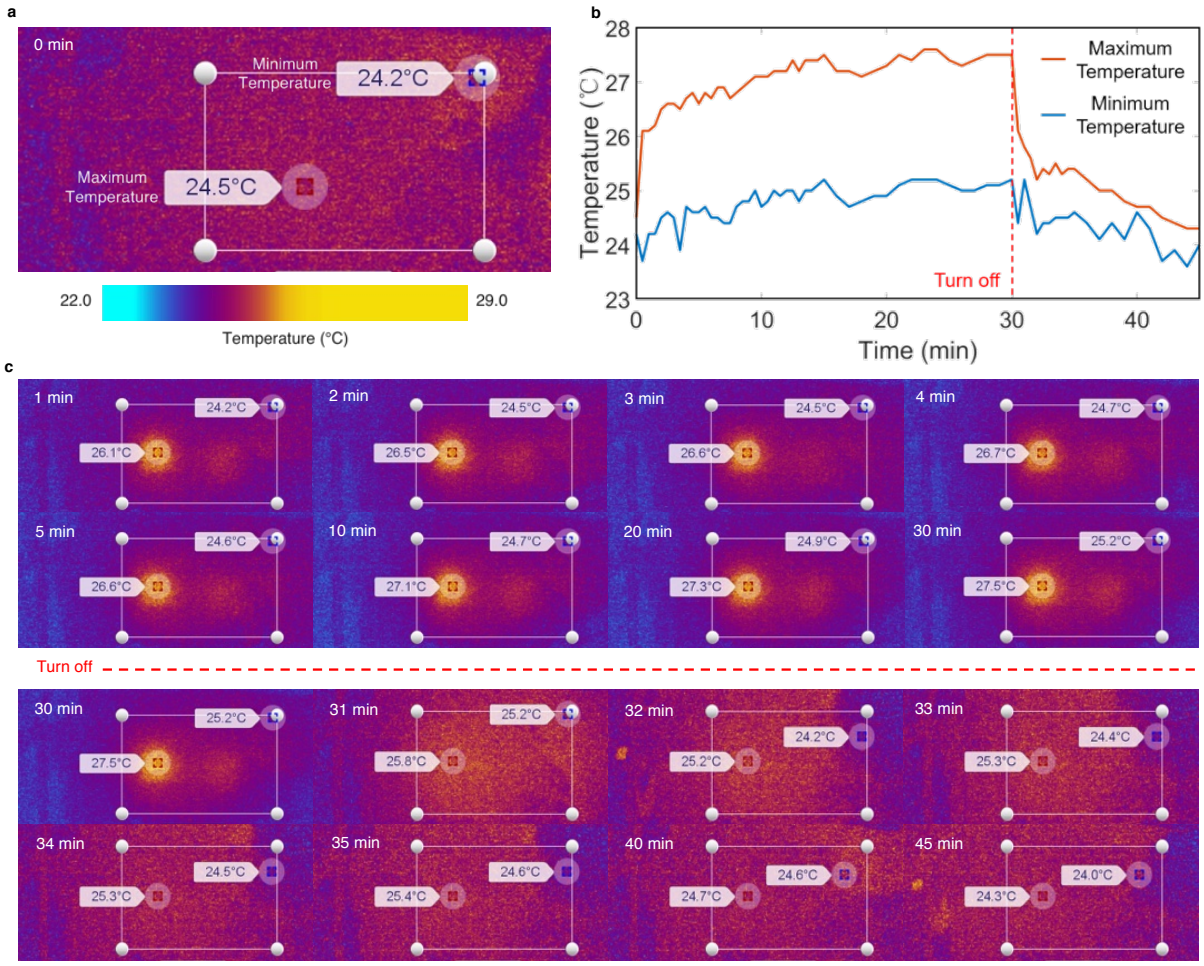

Supplementary Figure 44. Temperature variation of the device when working and resting (measured by an IR camera, on the bench at room temperature 24 °C). a, Temperature profile of the device right after being turned on. The rectangular area represents the actual device. Points with maximum and minimum temperature in the area are labeled. **b**, Maximum and minimum temperature variations of the device after turning on at 0 min and turning off at 30 min; **c**, IR images of the device after turning on 1~45 min. The device is turned off at 30 min. The highest temperature is located on the gyro chip, which has the biggest power dissipation. The temperature of the gyro chip increases 2.7 °C in the first 10 mins and is stable at 27.2 °C. When the system is shut down, the device temperature recoveres to the room temperature in ~10 mins.

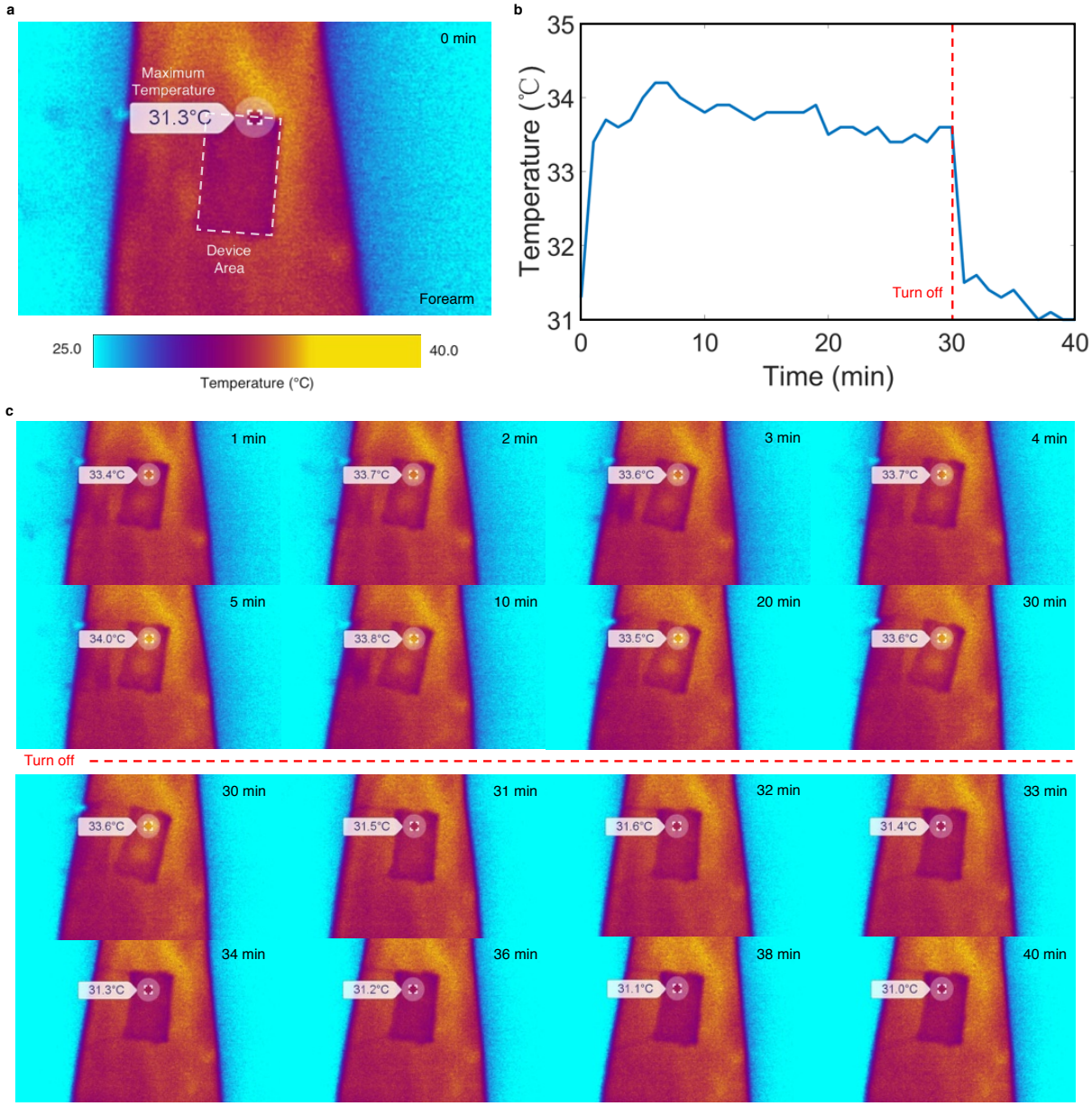

Supplementary Figure 45. Temperature variation of the device when working and resting (measured by an IR camera, on human forearm). a, Temperature profile of the device right after being turned on. The rectangular area represents the actual device. Points with maximum and minimum temperature in the area are labeled. **b**, Maximum temperature variations of the device after turning on at 0 min and turning off at 30 min; **c**, IR images of the device after turning on 1~40 min. The device is turned off at 30 min. The highest temperature of the system increases to 33.6 ^{o}C in 5 mins, only 2.3 ^{o}C higher than resting state 31.3 ^{o}C, which is acceptable for human skin.

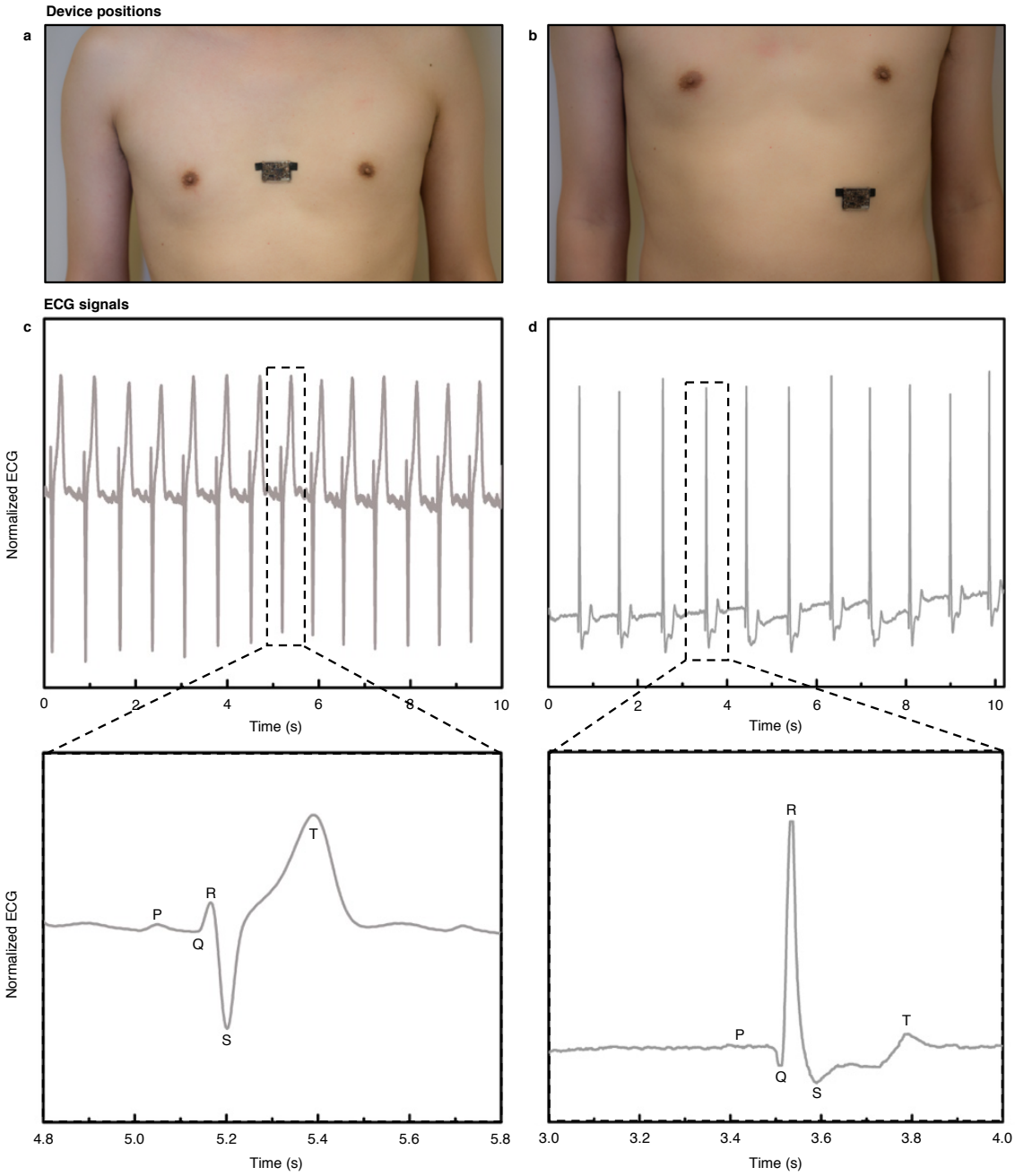

Supplementary Figure 46. ECG signals acquired from different positions of the human body. Images showing the device attached on (**a**) the chest and (**b**) the abdominal area. The power source for these measurements is omitted in the images for clarity purposes. Corresponding ECG signals acquired from (**c**) the chest and (**d**) the abdominal area, respectively.

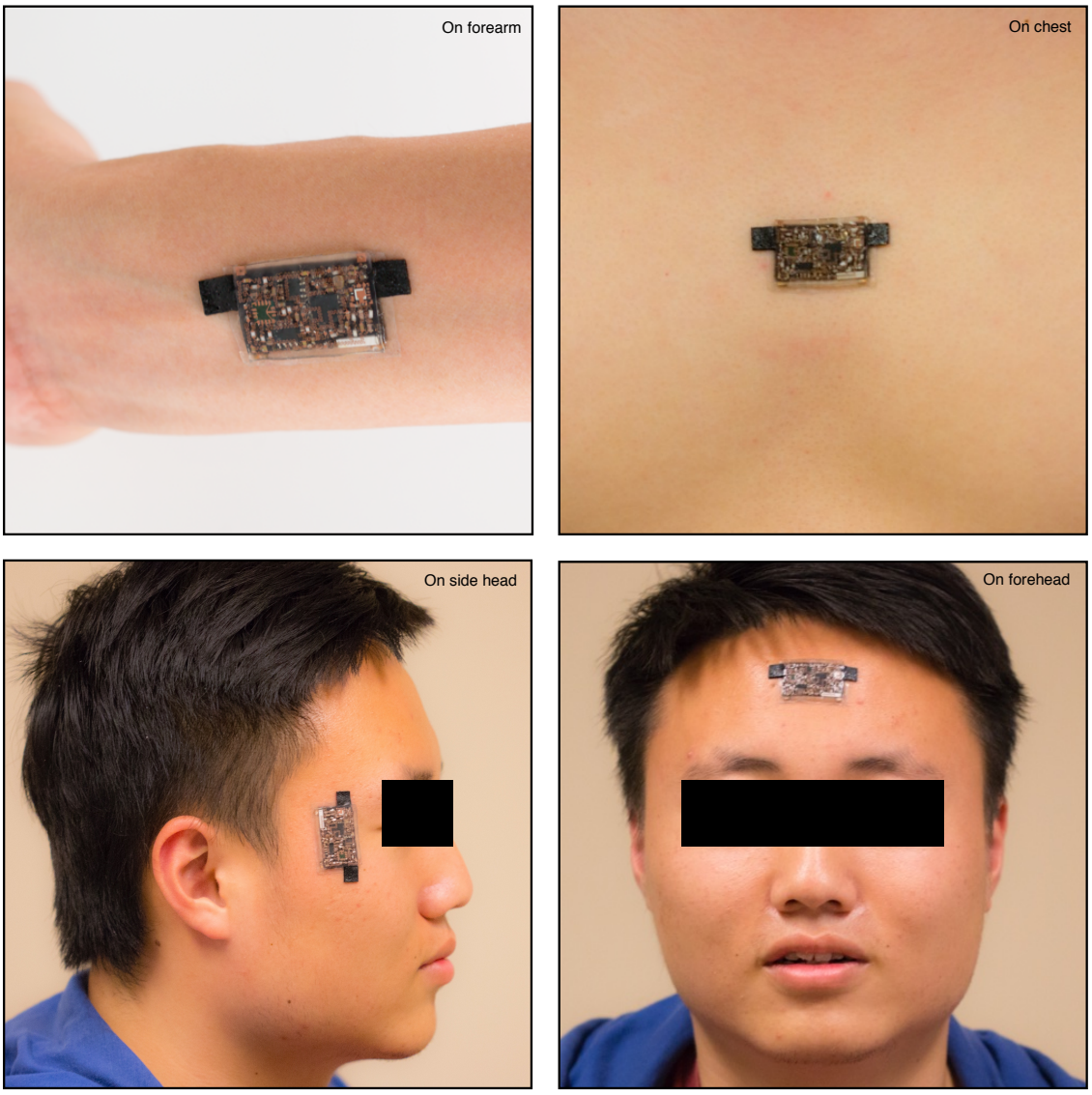

Supplementary Figure 47. Optical images showing the positions where the EP signals are acquired: on the forearm for EMG, on the chest for ECG, on the side head for EOG, and on the forehead for EEG. The power source for these measurements is omitted in the images for clarity purposes.

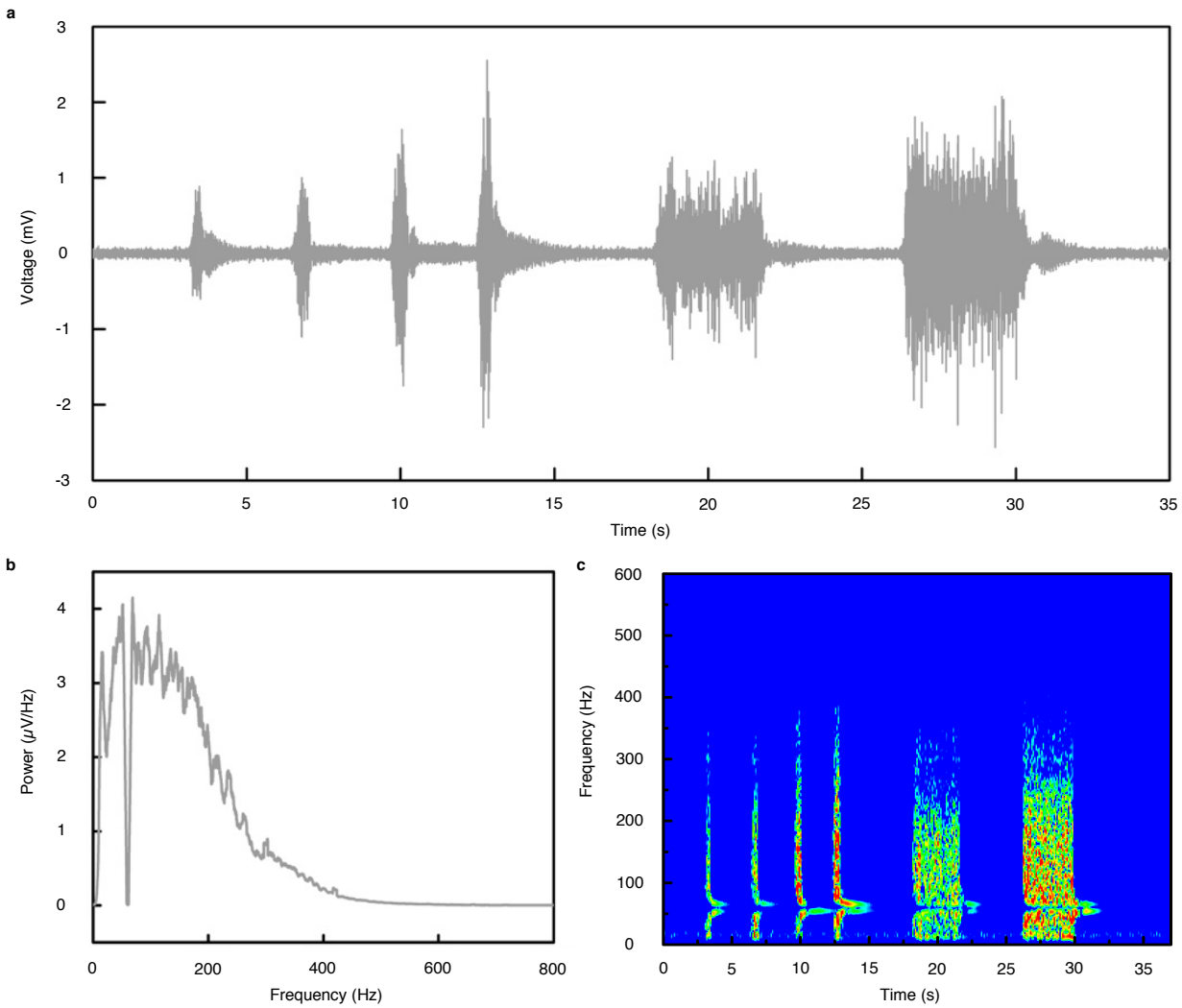

Supplementary Figure 48. EMG signals acquired from the forearm to show the signal frequency spectrum. a, EMG time-domain signals with 60 Hz notch filter. **b**, EMG signals from Fast Fourier Transform (FFT) analysis, showing the frequency distribution of the signals. The dip at around 60 Hz is from the notch filter. **c**, EMG power spectral density analyzed by Short-Time Fourier Transform (STFT), showing the time-domain EMG power distribution.

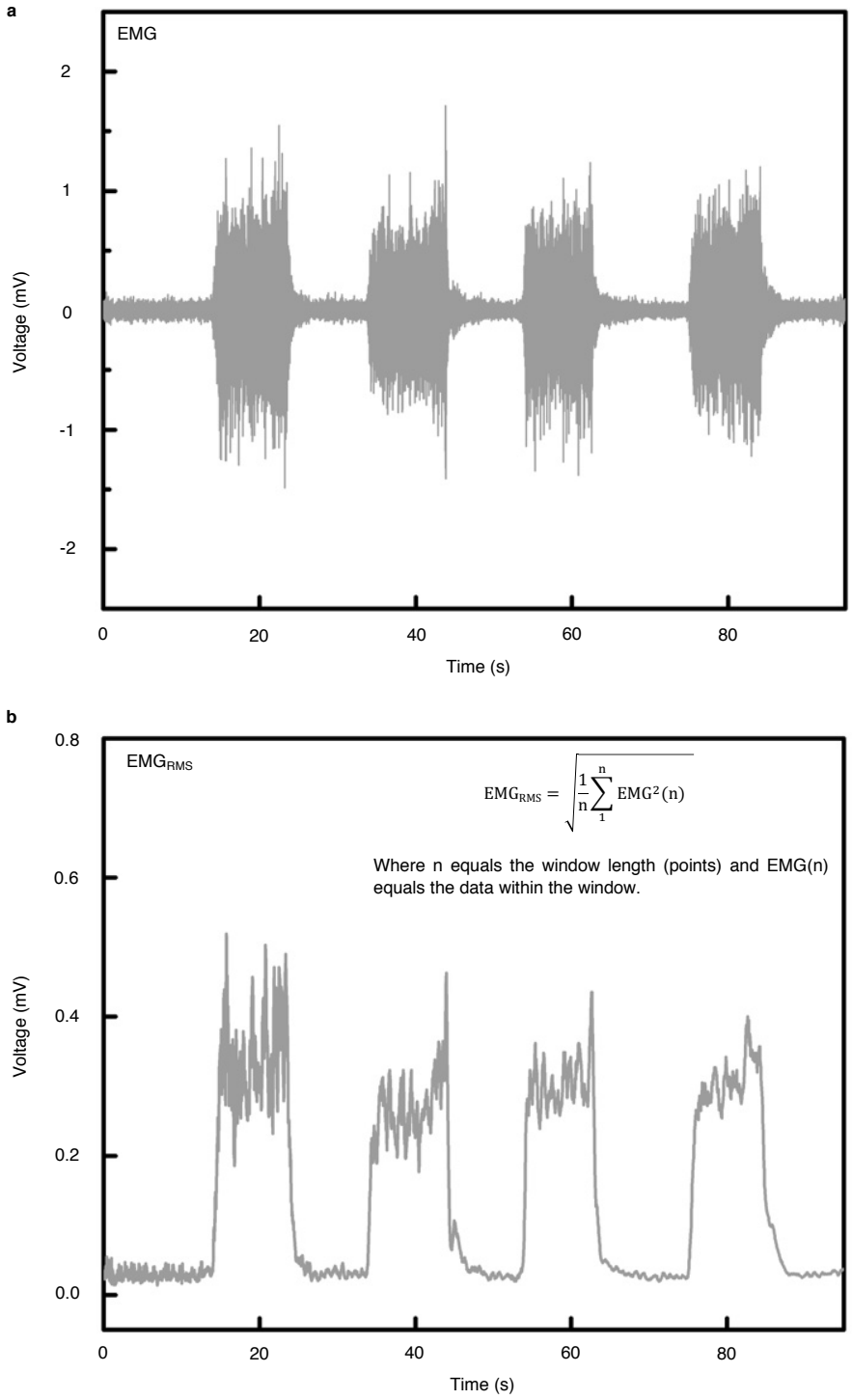

Supplementary Figure 49. EMG power analysis with root-mean-square envelope. a, The raw data of EMG signals acquired from the forearm with periodic clinching. **b**, Amplitude analysis with root-mean-square EMG envelope to quantify the signals.

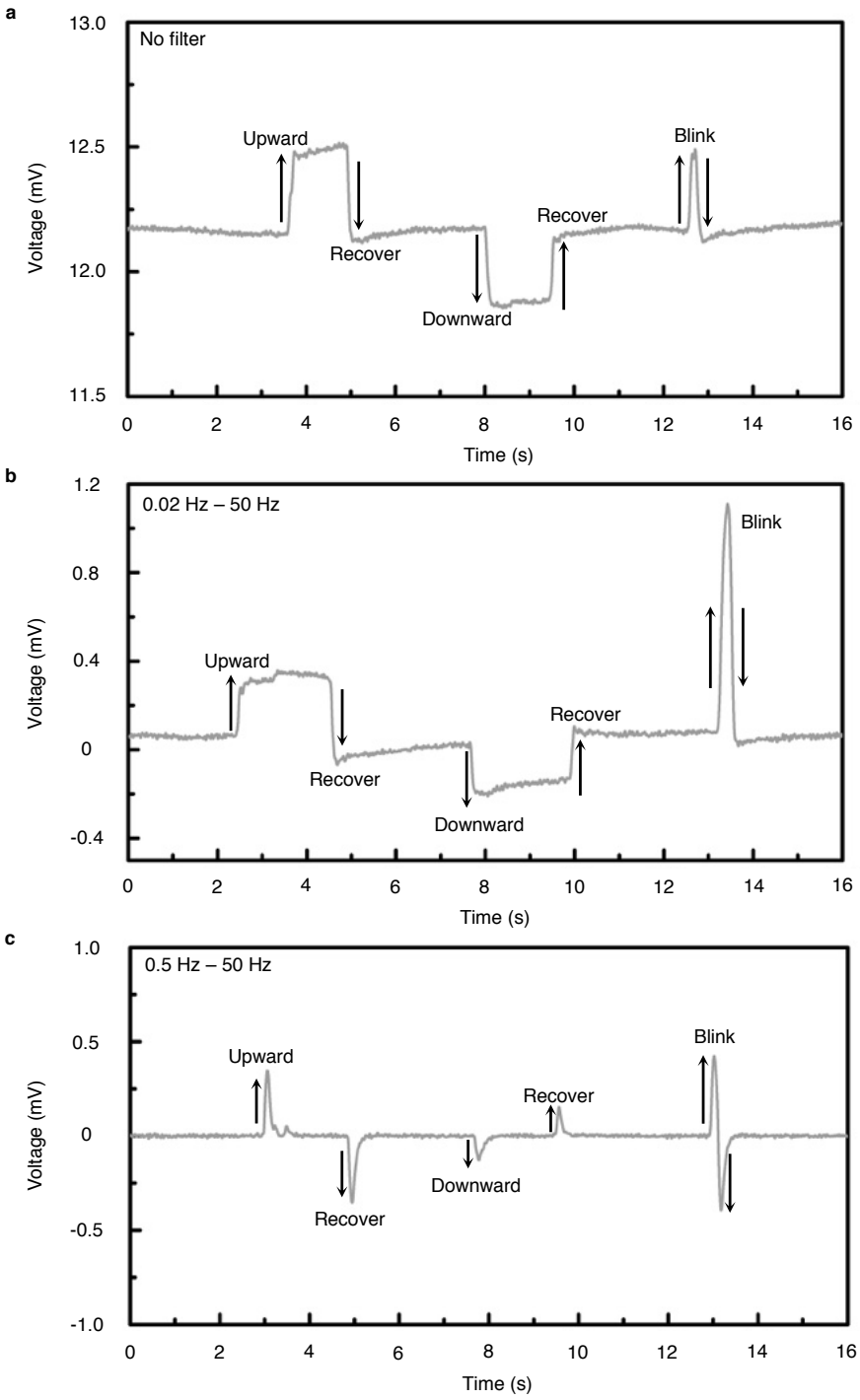

Supplementary Figure 50. EOG signals processed with different filters. a, EOG signals without a filter. There is a bias voltage of ~12.2 mV in the baseline, which is due to the charge accumulation between the two EP sensors. EOG signals with band-pass filters of (**b**) 0.02 Hz – 50 Hz and (**c**) 0.5 Hz – 50 Hz. The low frequency signal bias is removed. In **(c)** the EOG signals are also largely distorted from the original one. For our study, the filter of 0.02 Hz – 50 Hz is chosen.

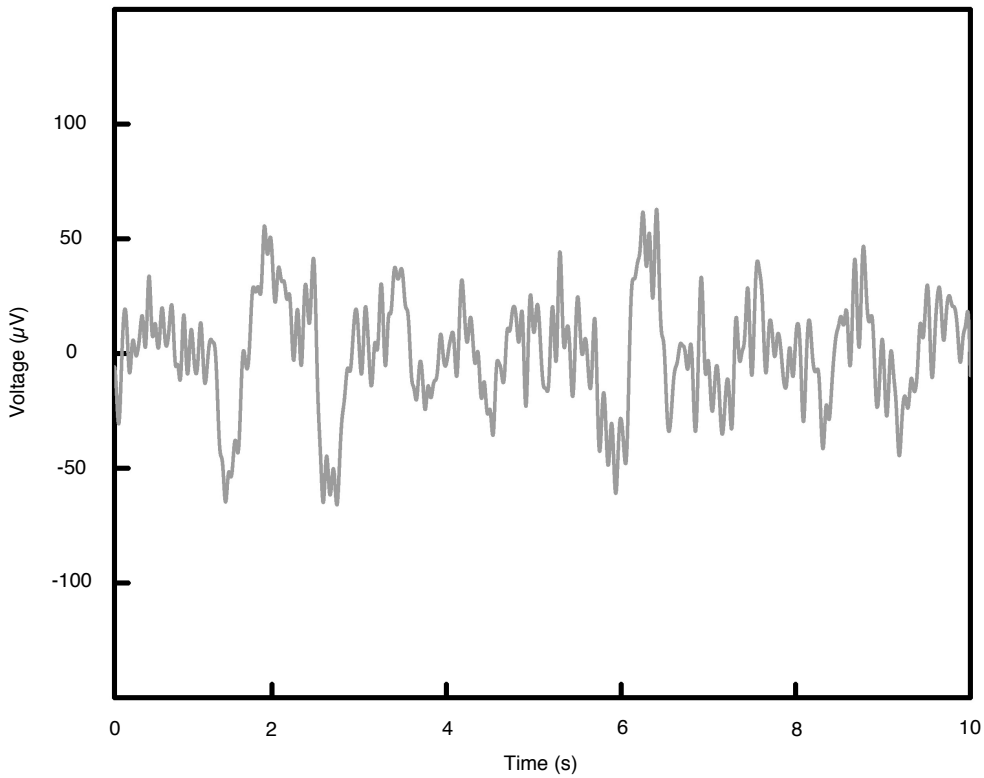

Supplementary Figure 51. EEG signals in the voltage-time domain. The signal noise level is around 15 μV with a signal/noise ratio ~7 for this measurement.

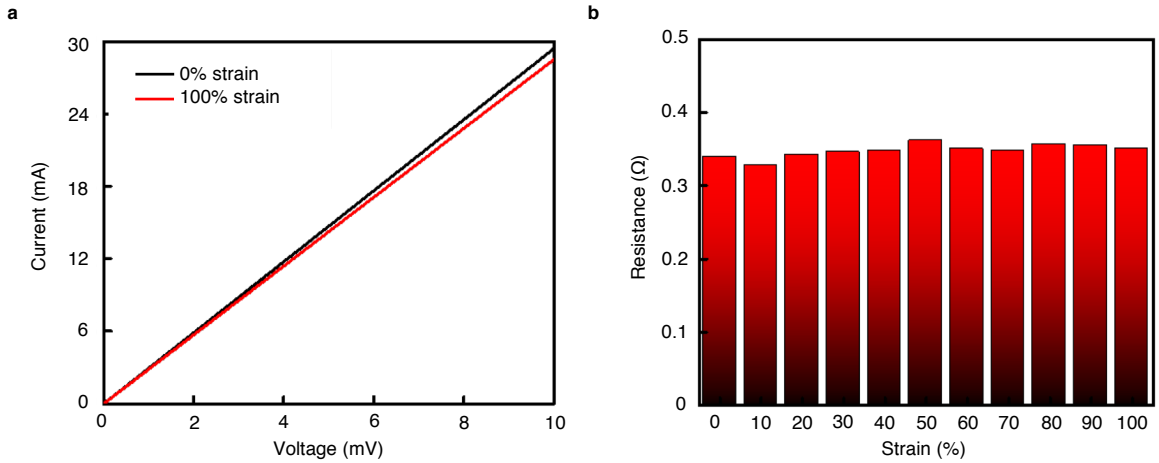

Supplementary Figure 52. Quantitative resistance evaluation of the interconnect under strain. a, I-V curves of the copper interconnect (width: 0.15 mm; pad-to-pad length: 5.68 mm; thickness: 0.02 mm) tested under 0% and 100% strain. From the slope of the straight line, the resistance of the copper interconnect can be calculated to be 0.34 Ω (0%) and 0.35 Ω (100%). **b**, With strain from 0% to 100% (increment 10%), the interconnect resistance was measured. The resistance varied in a narrow band from 0.33 Ω to 0.36 Ω, which indicates stable electrical properties of the interconnects.

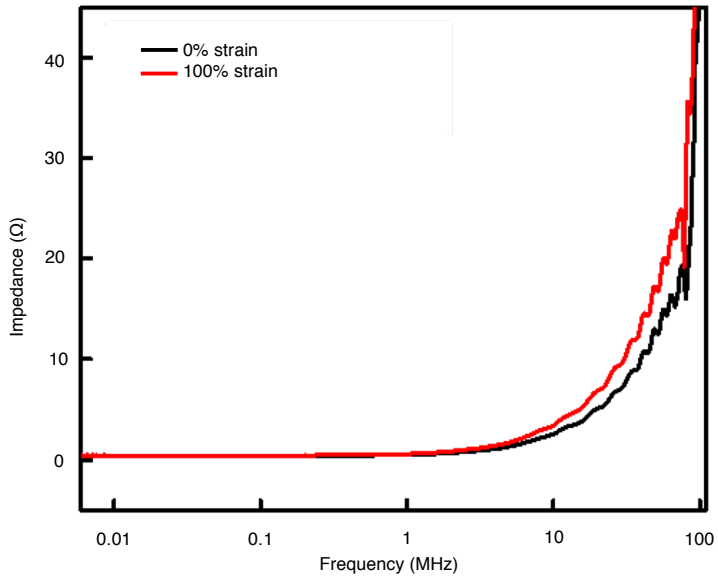

Supplementary Figure 53. Interconnect impedance spectroscopy of serpentine under free standing and 100% strain states. To evaluate the serpentine interconnect performance at high frequencies, the 5.75 mm pad-to-pad length serpentine's (width: 0.15 mm; thickness: 0.02 mm) impedance spectroscopy under 0% and 100% strain states was measured from 6 KHz to 100 MHz. Two conclusions can be drawn from the data. First, the interconnect impedance increases with increasing frequency, especially when the frequency is higher than 10 MHz due to the skin effect and increased inductive reactance at higher frequencies. Second, with interconnect strain increased from 0% to 100%, the impedance increases 7% with the frequency less than 1 MHz and increases up to around 34% especially in the high frequency range (larger than 10 MHz), which owns to the larger wire inductance due to the interconnect deformation.

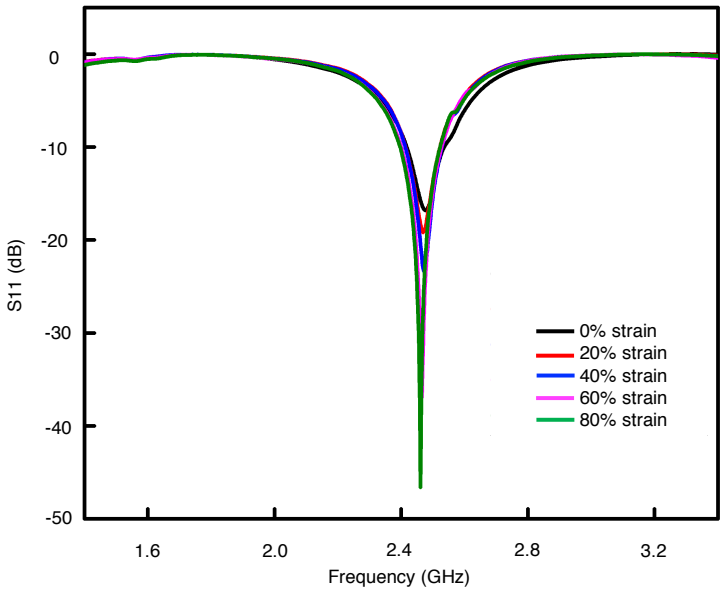

Supplementary Figure 54. S11 test of a 5.75 mm pad-to-pad length serpentine connected with the 2.4 GHz ceramic antenna under different levels of strain. The resonance frequency shift slightly from 2.475 GHz (0% strain) to 2.461 GHz (80% strain) due to the serpentine interconnect deformation and the corresponding S11 amplitude decreases from -16.79 dB to -46.59 dB, which means less reflection loss when the interconnect is deformed from serpentine geometry (0% strain) to buckled geometry (80% strain).

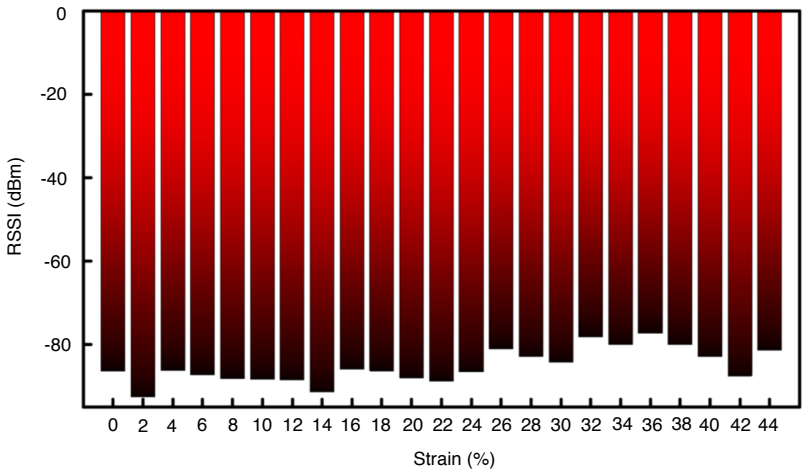

Supplementary Figure 55. The received-signal-strength-indicator (RSSI) of the Bluetooth signal from the multilayered device under strain from 0% to 44%. As the serpentine is very stable at low frequencies and is more sensitive to the strain when the frequency is higher than 10 MHz (Supplementary Figure 53), for the Bluetooth communication, we connect a 16 MHz oscillator to the BLE chip and a 2.4 GHz antenna is used for the wireless communication, which means the Bluetooth module may be the vulnerable part in the design. Therefore, we characterize the Bluetooth signal as a means for quantitative measurements of the multilayered system under strain. The received-signal-strength-indicator (RSSI) of the Bluetooth signal from the multilayered system is measured under different strain levels, with the receiver at a distance of several meters. It can be seen that the RSSI varied randomly from -75 dBm to -90 dBm with the strain from 0% to 44% of the entire system, which means the Bluetooth module work well with strain values up to 44%. For strain levels higher than 44%, the device is broken possibly due to the interconnect failure and no Bluetooth signal can be detected.

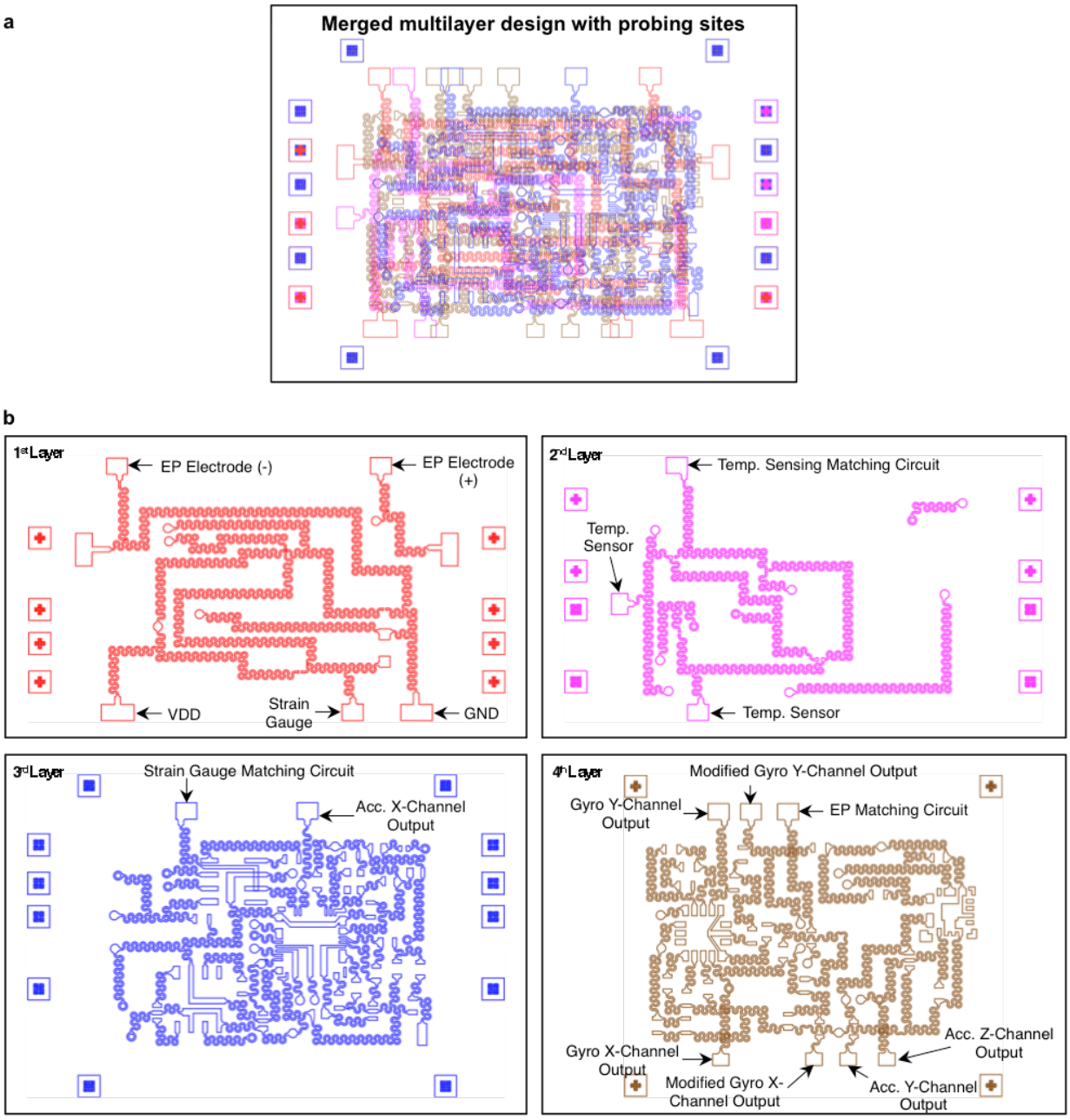

Supplementary Figure 56. The redesigned four-layer system with probing sites to evaluate the signal accuracy and qualify acquired by the sensors and processed by the chips. a, Schematics showing the merged new multilayer design with probing sites embedded. **b**, Layout designs for each separated layer with probing sites labeled.

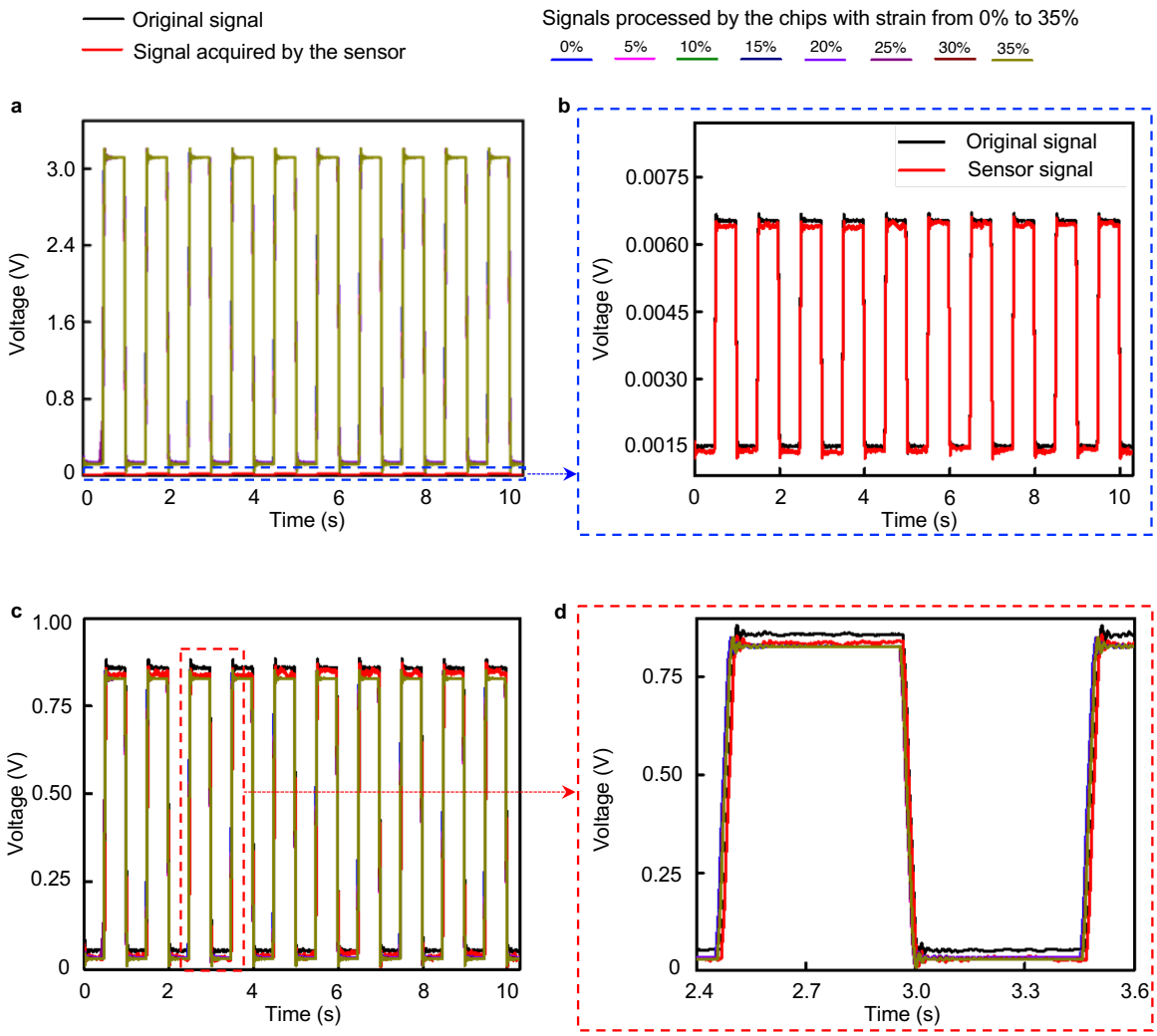

Supplementary Figure 57. Evaluation of signal accuracy and qualify acquired by the sensors and processed by the chips with different levels of strain in the system. a, The comparison of the original signal, signals acquired by the sensor, and signals amplified for 508 times and filtered by the chips when the systems are under different levels of strain from 0% to 35%. **b**, Zoom-in view of the original signal and sensor signal. **c**, Normalized original, sensor, and chip processed signals with different levels of strain in the system, with the zoom-in view shown in (**d**). The external strain has minimal impact on the device performance.

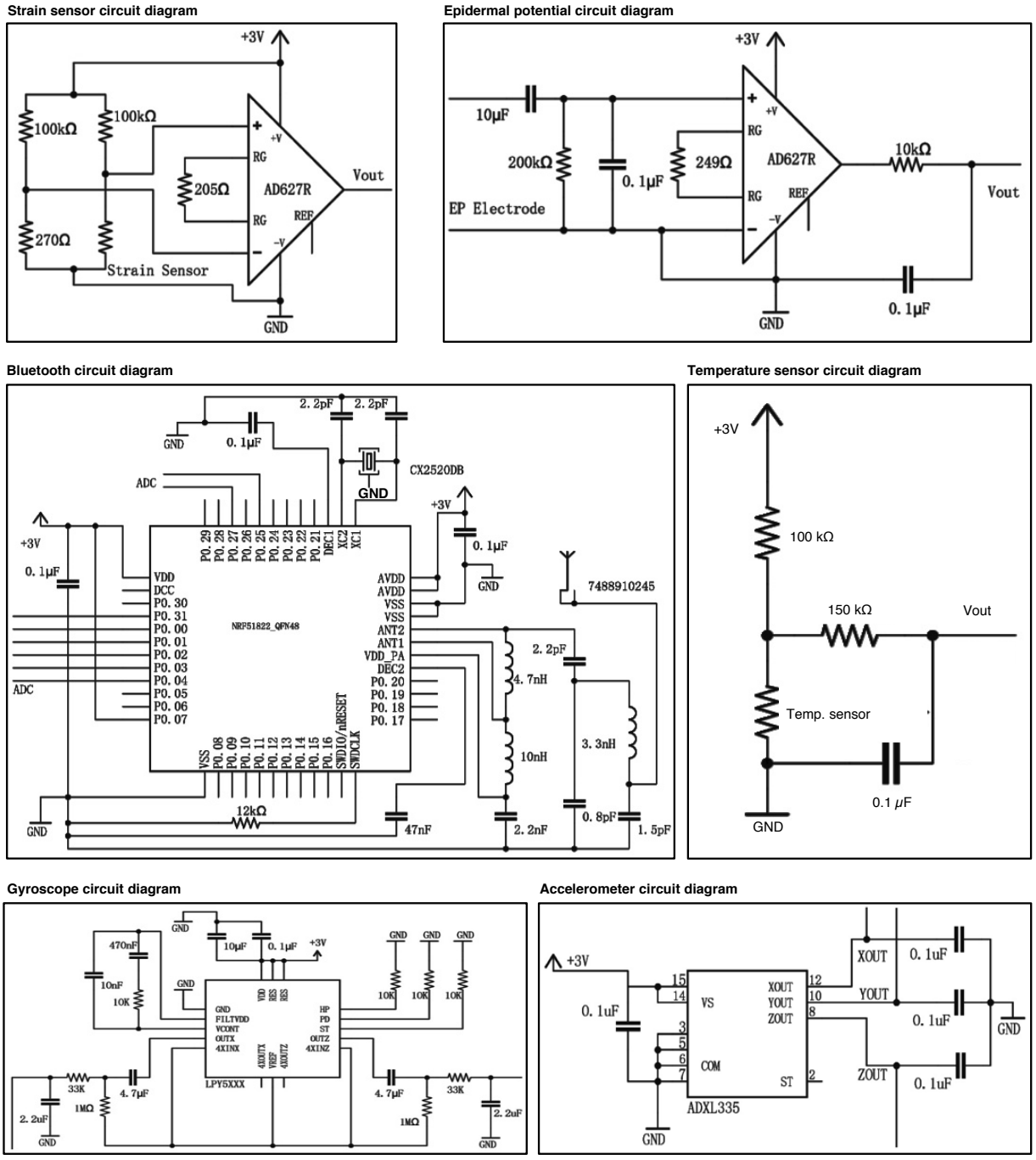

Supplementary Figure 58. Summary of the circuit design for the multilayered stretchable system. There are mainly six parts: a strain gauge, an electrophysiological potential sensor, a temperature sensor, a two-channel posture sensor, a three-channel acceleration sensor, and the Bluetooth. Low power medical instrumentation amplifiers (AD627B) are used to amplify signals for the strain and EP sensors. A matching circuit is designed to adjust the impedance of the Bluetooth to match the 2.4 GHz antenna impedance (50 Ohm), which helps increase the Bluetooth signal strength.

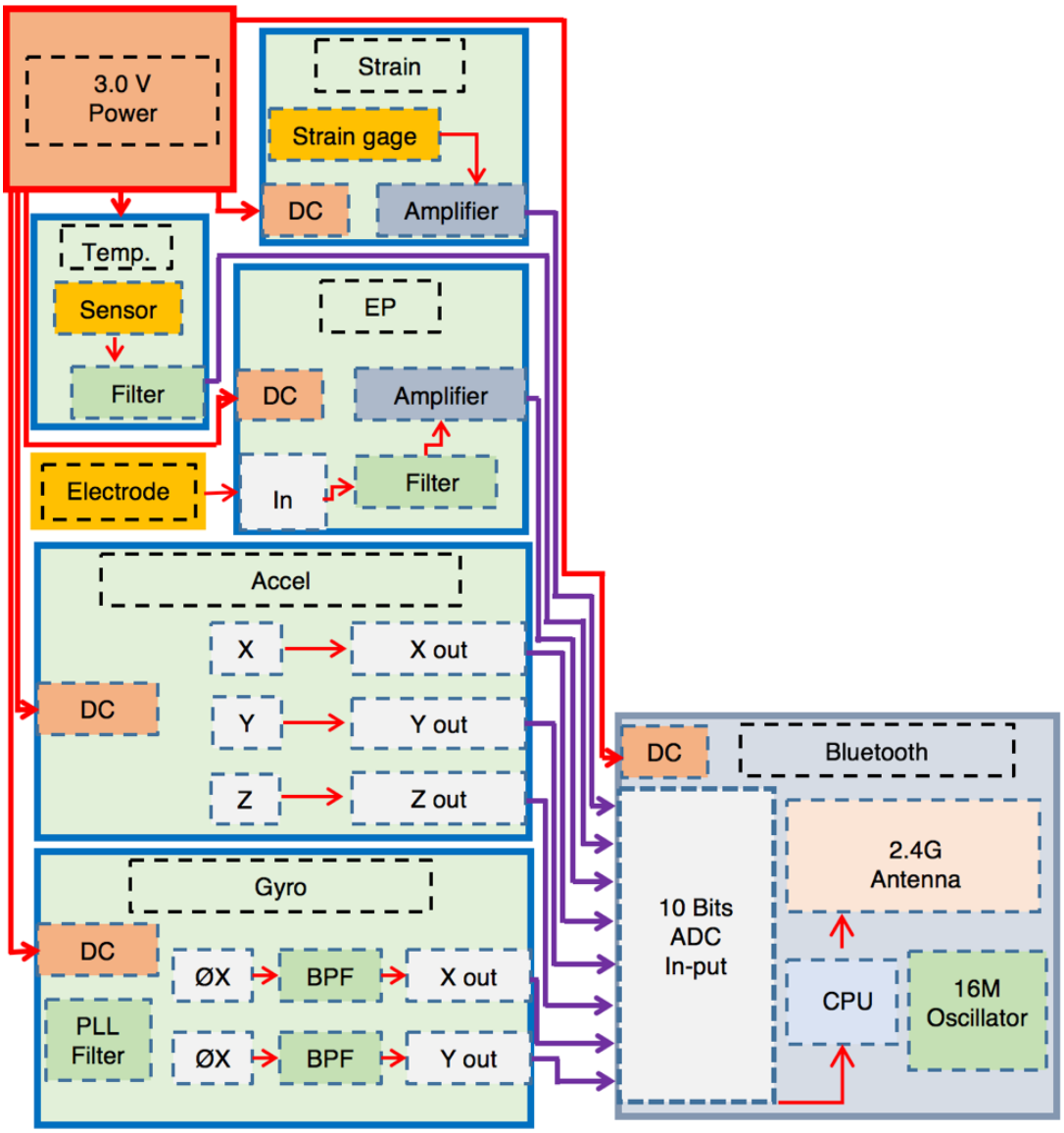

Supplementary Figure 59. Flow diagram showing the working principle of the multifunctional device. All the five sensing parts are connected with the Bluetooth for wireless data transmission. Analog sensing data are converted into digital signals with the built-in ADC from multi-protocol Bluetooth SOC (System on Chip). And then the data are transferred wirelessly with a 2.4 GHz antenna, oscillated by a 16 MHz external crystal. Both the sensing and wireless communication parts are powered by a 3 V battery.

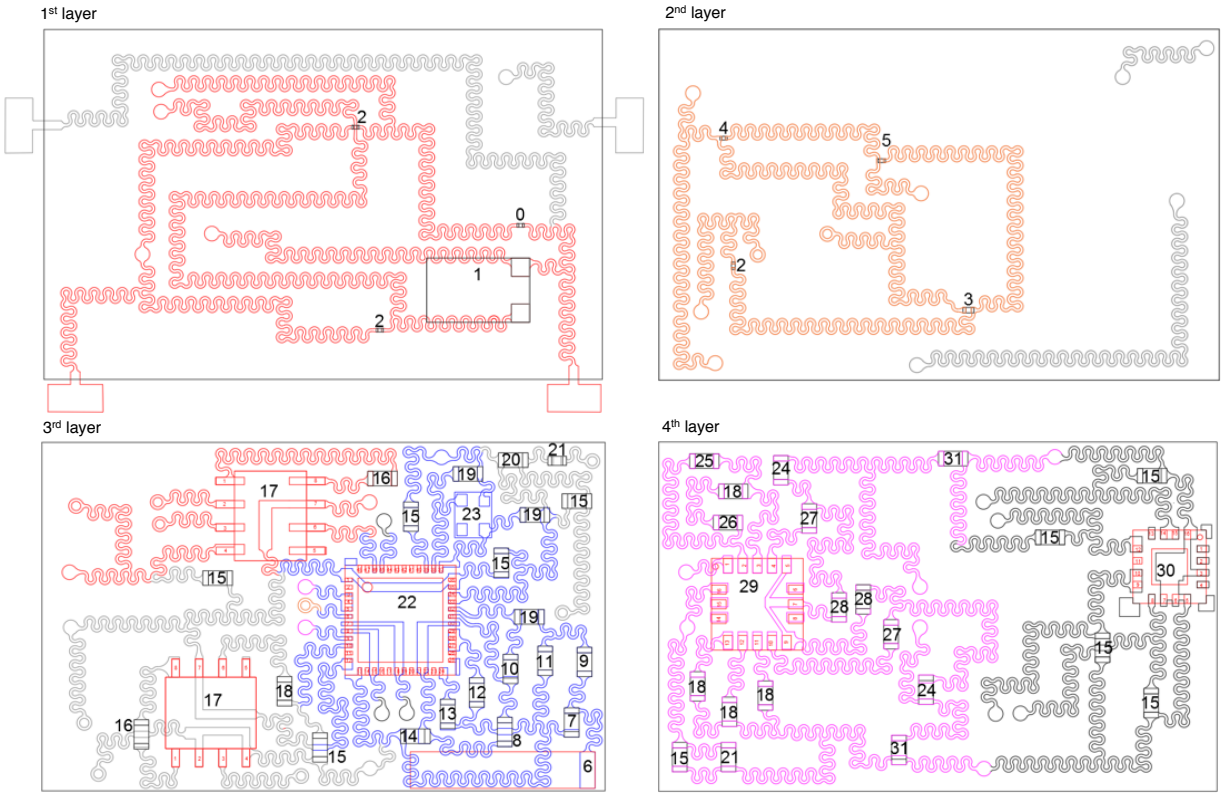

Device Number	Type	Value	Manufacturer Part Number	Device Number	Type	Value	Manufacturer Part Number
0	Resistor	270 Ohm	ERJ-XGNJ271Y	**16**	Resistor	249 Ohm	CR0603-FX-2490ELF
1	Strain sensor	N/A	BF350-3AA	**17**	Amplifier	N/A	AD627BRZ-R7
2	Resistor	100K Ohm	RC0402F104CS	**18**	Resistor	10K Ohm	CR0603-FX-1002HLF
3	Thermistor	N/A	NCP03WF104F05RL	**19**	Capacitor	2.2 pF	C0603C229C5GACTU
4	Capacitor	0.1 µF	CL02A104KQ2NNNC	**20**	Resistor	200K Ohm	CR0603-JW-204ELF
5	Resistor	150K Ohm	ERJ-XGNJ154Y	**21**	Capacitor	10 µF	GRM155C80J106ME11D
6	Antenna	N/A	7488910245	**22**	Bluetooth	N/A	NRF51822-QFAC-T
7	Capacitor	1.5 pF	CL10C1R5BB8NNNC	**23**	Crystal	N/A	CX2520DB16000D0GPSC1
8	Inductor	10 nH	L-14C10NJ4T	**24**	Resistor	33K Ohm	CR0603-FX-3302ELF
9	Inductor	3.3 nH	L-14C3N3SV4T	**25**	Capacitor	10 nF	GRM188R71H103KA01D
10	Inductor	4.7 nH	L-14C4N7SV4T	**26**	Capacitor	470 nF	C1608X7R1C474K080AC
11	Capacitor	0.8 pF	CL10C0R8BB8NNNC	**27**	Capacitor	4.7 µF	CL10B475KQ8NQNC
12	Capacitor	47 nF	C0603C473K1RACTU	**28**	Resistor	1M Ohm	CR0603-JW-105ELF
13	Resistor	12K Ohm	CR0603-JW-123ELF	**29**	Gyro	N/A	LPR503ALTR
14	Capacitor	2.2 nF	GRM1885C1H222JA01D	**30**	Accelerometer	N/A	ADXL335BCPZ
15	Capacitor	0.1 µF	GRM188R71C104KA01D	**31**	Capacitor	2.2 µF	GRM188R61C225KE15D

Supplementary Figure 60. Chip summary for the multilayered stretchable system. In total, 56 components, in 31 different types, are used in the design. All thick active components, such as the amplifiers, Bluetooth, antenna, gyroscope, and accelerometer, are integrated into the 3rd and 4th layer with an offset method to avoid direct overlap of thick chips.

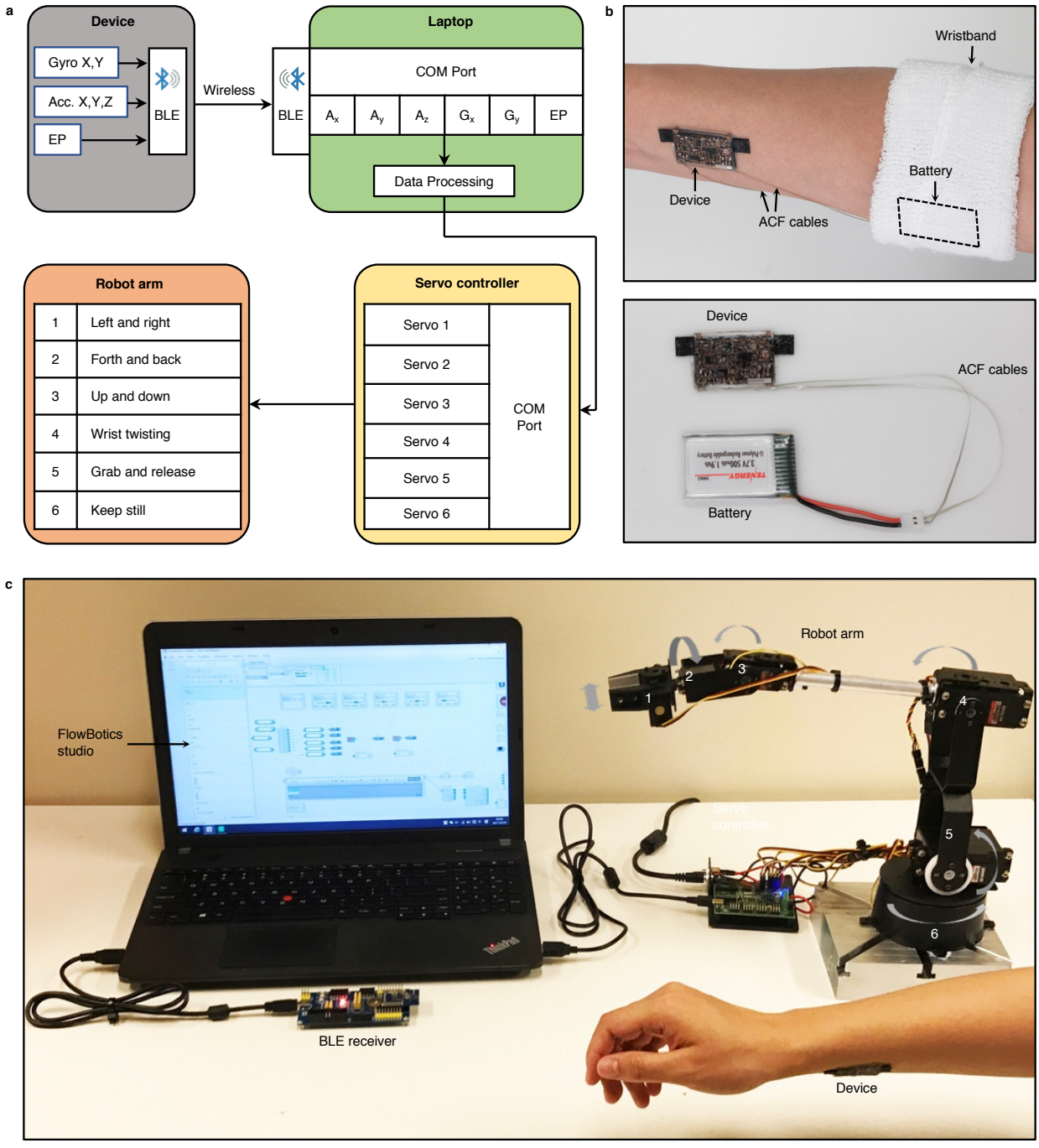

Supplementary Figure 61. Robotic arm controlling system. a, Work flow of the controlling system. **b**, The device is powered by a lithium polymer battery connected by the anisotropic conductive film (ACF) cables. The battery is fixed on the arm by a wristband. **c**, A picture showing the overall setup of the controlling system.

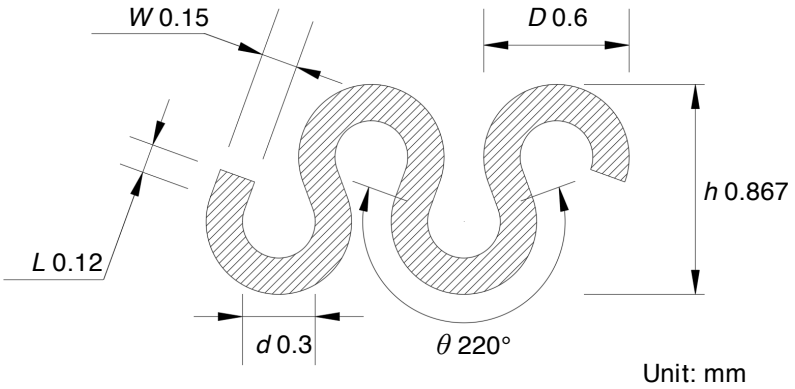

Supplementary Figure 62. Mechanical pattern design of the serpentine electrodes. Horseshoe serpentine design is employed as the interconnect between the components, with 0.6 mm for external diameter (D), 0.3 mm for internal diameter (d), 220° for curvature (θ), 0.12 mm for ribbon length (L), and 0.15 mm for ribbon width (W). The total height of each horseshoe h is 0.867 mm.

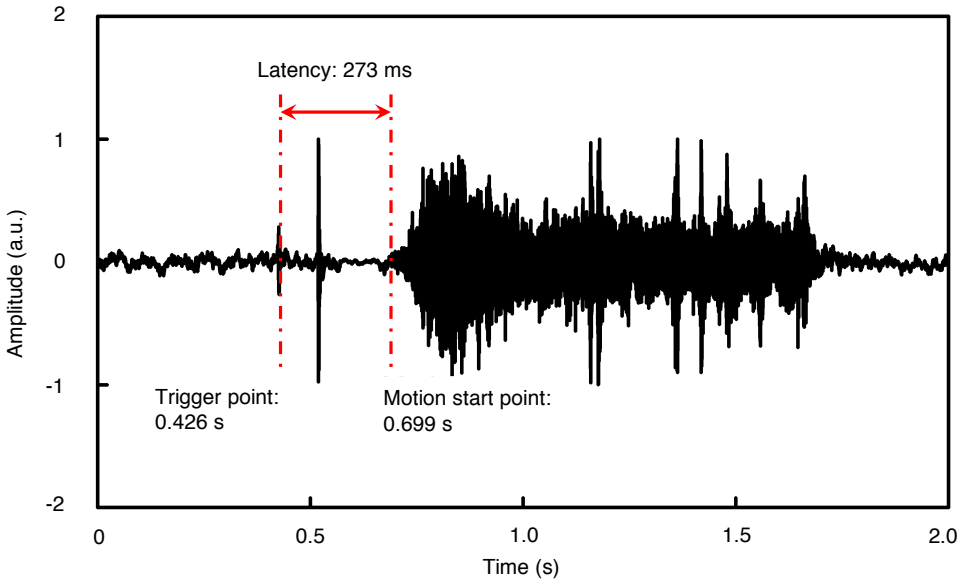

Supplementary Figure 63. The latency of the commercial robotic arm hardware and software. To quantify the delay from the robotic arm hardware (Lynxmotion AL5D arm with upgraded wrist rotate) and software (FlowBotics Studio), the audio signal of the system is recorded and the time between the trigger command and robot arm motion starting point is identified to be the robot system latency, which is around 273 ms.

Supplementary References

1. Ma, Y. et al. Soft Elastomers with Ionic Liquid-Filled Cavities as Strain Isolating Substrates for Wearable Electronics. *Small* **13**, (2017).
2. Tang, J., Li, J., Vlassak, J. J. & Suo, Z. Adhesion between highly stretchable materials. *Soft Matter* **12**, 1093-1099, (2016).
3. Li, J. et al. Tough adhesives for diverse wet surfaces. *Science* **357**, 378-381, (2017).
4. Johnson, H., Johnson, H. W. & Graham, M. *High-speed signal propagation: advanced black magic*, (2003).
5. Lin, Y. et al. Advances toward bioapplications of carbon nanotubes. *Journal of Materials Chemistry* **14**, 527-541, (2004).
6. Garibaldi, S., Brunelli, C., Bavastrello, V., Ghigliotti, G. & Nicolini, C. Carbon nanotube biocompatibility with cardiac muscle cells. *Nanotechnology* **17**, 391, (2005).
7. Park, Y.-H. et al. Assessment of dermal irritation potential of MWCNT. *Toxicology and Environmental Health Sciences* **2**, 115-118, (2010).
8. Ema, M., Matsuda, A., Kobayashi, N., Naya, M. & Nakanishi, J. Evaluation of dermal and eye irritation and skin sensitization due to carbon nanotubes. *Regulatory Toxicology and Pharmacology* **61**, 276-281, (2011).
9. Grunlan, J. C., Mehrabi, A. R., Bannon, M. V. & Bahr, J. L. Water-Based Single-Walled-Nanotube-Filled Polymer Composite with an Exceptionally Low Percolation Threshold. *Advanced Materials* **16**, 150-153, (2004).
10. Huang, J.-E., Li, X.-H., Xu, J.-C. & Li, H.-L. Well-dispersed single-walled carbon nanotube/polyaniline composite films. *Carbon* **41**, 2731-2736, (2003).
11. Supronowicz, P. et al. Novel current-conducting composite substrates for exposing osteoblasts to alternating current stimulation. *Journal of Biomedical Materials Research Part A* **59**, 499-506, (2002).
12. Jung, H.-C. et al. CNT/PDMS composite flexible dry electrodes for long-term ECG monitoring. *IEEE Transactions on Biomedical Engineering* **59**, 1472-1479, (2012).
13. Lam, C.-W., James, J. T., McCluskey, R. & Hunter, R. L. Pulmonary toxicity of single-wall carbon nanotubes in mice 7 and 90 days after intratracheal instillation. *Toxicological Sciences* **77**, 126-134, (2004).
14. Warheit, D. B. et al. Comparative pulmonary toxicity assessment of single-wall carbon nanotubes in rats. *Toxicological Sciences* **77**, 117-125, (2004).
15. Huczko, A. et al. Pulmonary Toxicity of 1-D Nanocarbon Materials. *Fullerenes, Nanotubes, and Carbon Nanostructures* **13**, 141-145, (2005).
16. Muller, J. et al. Respiratory toxicity of multi-wall carbon nanotubes. *Toxicology and Applied Pharmacology* **207**, 221-231, (2005).
17. Fan, J. A. et al. Fractal design concepts for stretchable electronics. *Nat. Commun.* **5**, 3266, (2014).
18. Aoki, H. Laser processing method to form an ink jet nozzle plate. (1998).
19. Bohme, R. & Zimmer, K. Laser fabrication of micro sized diffractive and refractive optical devices in fused silica and glass. *CLEO/Europe IEEE Cat.* 688, (2003).
20. Klank, H., Kutter, J. P. & Geschke, O. CO2-laser micromachining and back-end processing for rapid production of PMMA-based microfluidic systems. *Lab on a Chip* **2**, 242-246, (2002).

21. Itzkan, I. et al. The thermoelastic basis of short pulsed laser ablation of biological tissue. *Proceedings of the National Academy of Sciences of the United States of America* **92**, 1960-1964, (1995).
22. Patel, R. S. & Wassick, T. A. Laser processes for multichip module's high-density multilevel thin film packaging. **2991**, 217-223, (1997).
23. Cho, K. *et al.* Analysis of latency performance of Bluetooth low energy (BLE) networks. *Sensors* **15**, 59-78, (2014).